

Università degli Studi di Napoli Federico II



Ph.D. in

Aerospace Engineering, Naval and Total Quality Management Engineering

Ph.D. School in Industrial Engineering

Ph.D. Cycle XXVII

Ph.D. Thesis

Bathymetric Digital Elevation Model Generation from
L-band and X-band Synthetic Aperture Radar Images

in the Gulf of Naples, Italy:

Innovative Techniques and Experimental Results

Ph.D. Supervisors:

Prof. Antonio Moccia

Prof. Sergio Vetrella

Dr. Alfredo Renga

Ph.D. Candidate:

Valentina Boccia

Table of Contents

Abstract	6
Introduction	7
Chapter 1 - Coastal Bathymetry	8
1.1 Definition and scope of bathymetry.....	9
1.2 Conventional techniques for bathymetric reconstruction in coastal area.....	10
1.2.1 Single-beam echo sounders.....	10
1.2.2 Light Detection and Ranging (LIDAR) systems.....	12
1.2.3 Electro-optical instruments.....	14
1.3 SAR-based bathymetry: a new approach.....	15
Chapter 2 - SAR Imaging of Sea	16
2.1 The sea: waves and currents.....	17
2.2 Synthetic Aperture Radar (SAR)	23
2.3 SAR imaging of sea surface.....	26
Chapter 3 - SAR-Based Bathymetric Techniques and Models	33
3.1 Wave-based bathymetric technique.....	34
3.1.1 Linear Dispersion Relation.....	35
3.1.2 Non-linear or finite-amplitude wave theories.....	40

3.1.3 Composite models.....	47
3.1.4 Validity of wave theories.....	48
3.1.5 Synthesis and discussion.....	50
3.2 Current-based bathymetric technique.....	51
3.2.1 Alpers and Hennings model.....	53
3.2.2 Bathymetric Assessment System - BAS.....	58
3.2.3 Volterra Series Expansion.....	61
3.2.4 Synthesis and discussion.....	70
Chapter 4 - Error Budget Analysis.....	73
4.1 Wave-Based Approach (WBA) based on the Linear Dispersion Relation.....	74
4.1.1 Applicability of the Linear Dispersion Relation.....	75
4.1.2 Error budget analysis - WBA.....	77
4.1.3 SAR based products derived from WBA.....	83
4.1.4 Specifications and requirements - WBA.....	84
4.2 Current-Based Approach (CBA) based on Volterra Series Expansion.....	87
4.2.1 Error budget analysis - CBA.....	87
4.2.2 SAR based products derived from CBA.....	92
4.2.3 Specifications and requirements - CBA.....	94
Chapter 5 - WBA Application to SAR Image.....	97

6.3.2.4 COSMO-SkyMed SAR image N° 4 (Scene ID: EL20130120_512956_2545081.6.2).....	126
6.3.2.5 COSMO-SkyMed SAR image N° 5 (Scene ID: EL20130210_514951_2630659.6.2).....	128
6.3.2.6 COSMO-SkyMed SAR image N° 6 (Scene ID: EL20130210_514951_2632986.6.2).....	130
6.4 Experimental results obtained on the selected ALOS PALSAR image.....	133
6.4.1 Tracking of swell shoaling and refraction phenomena on the selected ALOS PALSAR image.....	133
6.4.2 Digital Elevation Model retrieved from the selected ALOS PALSAR image.....	138
6.5 Experimental results obtained on the selected COSMO-SkyMed SAR image.....	142
6.5.1 Tracking of swell shoaling and refraction phenomena on the selected COSMO-SkyMed SAR image.....	143
6.5.2 Digital Elevation Model retrieved from the selected COSMO-SkyMed SAR image.....	146
Chapter 7 - Discussion and Conclusions.....	150
References.....	154

Abstract

The present Ph.D. Thesis investigates remote sensing bathymetric techniques in coastal area based on the use of Synthetic Aperture Radar (SAR) data. Since SAR signal is not able to pass sea surface and to reach sea bottom, indirect processes with sea floor morphology sensed through the effects it may have on sea surface are investigated.

The conventional bathymetric techniques are briefly analyzed and the main advantages related to the use of remote sensing SAR-based bathymetric techniques highlighted. Proper sea surface modeling is performed and its interaction with SAR is investigated. Two different bathymetric techniques are proposed: the Wave-Based Approach (WBA) and the Current-Based Approach (CBA). Several theories for proper modeling of the involved phenomena and of their retrieval from SAR images are presented and the most promising are identified. An error budget analysis is performed and potential performance, specifications and requirements of the considered bathymetric approaches are described.

With specific reference to the area of the Gulf of Naples, Italy, the Wave-Based Approach is selected because of current velocity being too slow or too irregular both in time and in intensity for proper application of the Current-Based Approach. Therefore, a WBA algorithm for sea surface spectrum retrieval from SAR data is proposed.

The proposed WBA algorithm is applied on both L-band ALOS PALSAR images and X-band COSMO-SkyMed SAR images covering the area of the Gulf of Naples, Italy. The experimental results and the achieved improvements with respect to the approaches found in the available literature are presented. Digital Elevation Models (DEMs) of seabed are obtained and a correlation analysis with the retrieved water depth values from the official nautical charts provided by the Italian Navy Hydrographic Institute is performed.

Introduction

The main goal of the performed Ph.D. research has been the investigation of innovative techniques to retrieve bathymetric data from Synthetic Aperture Radar (SAR) images and their application to the area of the Gulf of Naples, Italy, by using both L-band ALOS PALSAR data and X-band COSMO-SkyMed SAR data provided by the Italian Space Agency (ASI). Indeed, the research has been part of the SAR4BAT project (Synthetic Aperture Radar data fusion for bathymetric retrieval of seabed in coastal areas and archaeological areas) founded by ASI in the framework of a call reserved to Small/Medium Enterprises (SMEs) and dealing with Earth observation.

This work has been carried out also with the financial contribution of Regione Campania in the framework of the project for Technology Innovation of Transport Systems (INSIST).

Specifically, an algorithm for proper bathymetric data retrieval when the Wave-Based Approach is considered has been developed and tested. Results have shown that it provides a significant improvement in water depth estimation and Digital Elevation Model generation of seabed morphology with respect to the approaches described in the available literature.

The present Ph.D. Thesis is organized as follows. Chapter 1 introduces the conventional bathymetric techniques and the advantages related to the approach based on SAR. Chapter 2 presents the adopted sea surface modeling theory and the main concepts related to SAR interaction with sea surface. Chapter 3 describes two SAR-based bathymetric approaches and the several theories for proper modeling of the involved phenomena. Chapter 4 reports on the performed error budget analyses and the retrieved specifications for both the two bathymetric approaches. Chapter 5 describes the proposed algorithm for implementation of the selected SAR-based bathymetric technique on SAR data. Chapter 6 shows the adopted data set and the main obtained results.

Chapter 1

Coastal Bathymetry

This chapter provides a description of the meaning and scope of bathymetry. The adopted terminology is introduced and the main concepts and methodologies for bathymetric data representation are described. Some of the main bathymetric applications are considered in order to highlight the importance of accurate bathymetric data retrieval in coastal area. The chapter proceeds with an overview of the main bathymetric methods currently used to detect sea water depth in coastal zone. Their working principles are briefly described, together with the benefits and drawbacks of each method. Finally, the SAR-based bathymetric approach analyzed in the performed study is briefly introduced.

1.1 Definition and scope of bathymetry

The term “bathymetry” originally referred to the underwater depth of the floor of water bodies, including oceans, seas, rivers, streams, and lakes, relative to their surface. Nowadays, it also means the measurement and study of the depths and shapes of underwater terrain thus also being defined as mean “submarine topography” [1].

Similarly to topographic maps representing the three-dimensional features of emerged terrain, bathymetric maps depict the land that lies underwater. Therefore, most of the conventional definitions used in topography and, more in general, in solid Earth analysis can be properly adopted if the altitude above the (mean) sea level is replaced by the depth below the (mean) sea level. Indeed, bathymetry has been historically represented by colors and contour lines on dedicated maps [1], i.e. bathymetric and nautical maps. Contours represented the first technique for quantitative (analogical) relief representation in cartographic documents [2] and they describe bathymetry as a set of iso-depth lines. However, despite their widespread use, contour maps present some problems since there are no data between consecutive iso-depth lines and errors can be introduced, e.g. in drawing, line generalization, reproduction, thus losing the essential original information [3]. In the last decades digital data modeling and analysis have been diffusely exploited by using Digital Terrain Models (DTMs) and Digital Elevation Models (DEMs), i.e. a subset of DTM merely representing the relief. Again, DEM is used also with reference to the bathymetric relief in order to avoid the introduction of a specific acronym, e.g. Digital Depth Model. Nowadays, it represents the standard for Geographic Information System (GIS) processing of bathymetric information content.

Dense and accurate bathymetric information in coastal area is essential due to the crucial role that coastal zones play in human society. Indeed, those areas embrace a large number of activities, such as recreation, fishing, cargo ships and sailing boats traffic, pipeline management, cable laying, power plant exploitation, and research. Accurate information and monitoring of coastal areas have been identified as a crucial aspect at the international level [4] since they assure proper coastal management, risk assessment and suitable planning of infrastructures. Concerning this, accurate measurement of sea water depth and monitoring of seabed morphology variations play an important role for proper resource management [5]. Reliable retrieval of bathymetric information and production of up-to-date relevant DEMs of coastal areas can guarantee safe navigation and execution of several important activities such as warp analysis, forecasting of potential flooding effects and geomorphological risk monitoring [6]. Moreover, investigation of seabed morphology can support marine pollution monitoring and underwater archeology [7].

1.2 Conventional techniques for bathymetric reconstruction in coastal area

Since the mid of 1900s single-beam echo-sounders derived from military sonar have been developed and exploited for hydrographic surveying [8]. During the last decades multi-beam echo-sounders have been used for wide area oceanic depth surveying while single-beam echo-sounders embarked on a ship represent the most common and mature technique for bathymetric data retrieval in coastal area. During the 1980s, a new bathymetric technique based on light detection and ranging, i.e. the LIDAR technology, from airplanes or helicopters was introduced and exploited. Nowadays, it constitutes a well established bathymetric method and, therefore, it is used for comparison with the data obtained from other remote sensing techniques, such as the use of passive electro-optical instruments.

1.2.1 Single-beam echo sounders

An echo-sounder is a ranging system based on the transmission and reception of either sonic or ultrasonic waves [8]. Specifically a sonic/ultra-sonic pulse is transmitted from a transducer embarked on a ship (see Fig. 1.1.a). The pulse is reflected from seabed back to the transducer and therefore is received by the echo-sounder. The time lag between transmission and reception of a sonic or ultra-sonic pulse represents a direct measurement of the local depth.

Normally, the area of interest is covered by planned straight transects [9] thus retrieving a dense distribution of bathymetric measurements (see Fig. 1.1.b).

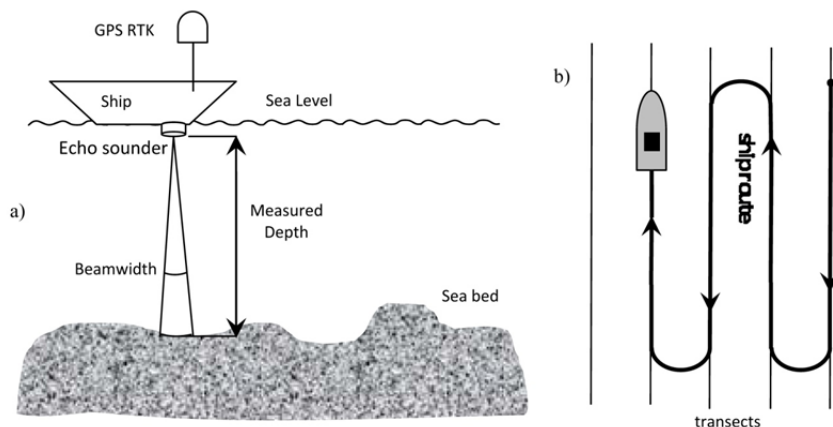


Fig. 1.1 Illustration of bathymetric data retrieval based on single-beam echo sounders (partially adapted from [9],[10]).

Echo-sounders were derived from military sonar. Therefore, most of the basic principles of echo-sounders share similarities with the basic radar operations:

- 1) The transmission of short pulses is used in both cases to allow for ranging measurements with a main difference being represented by the wavelength of the transmitted pulses. More in detail, microwave frequencies (0.3-300 GHz) are used by radar whereas sonic and ultrasonic frequencies (10-500 kHz) are utilized by echo-sounders. The reason for this difference is that despite electromagnetic waves have an excellent propagation in a vacuum and air, they hardly penetrate nor propagate through liquids. Instead, acoustic waves, either sonic or ultra-sonic, achieve good penetration and propagation through all elastic media once these media can be made to vibrate when exposed to pressure variations as in water.
- 2) Time measurements are converted to range measurements through the knowledge of signal propagation velocity. Radar signal travels at the velocity of light (about $3 \cdot 10^8$ m/s) while sound waves propagate in sea water with a velocity of about 1500 m/s. In both cases the range resolution can be expressed as $c\tau/2$ where c is the propagation velocity and τ the pulse length.
- 3) The energy transmitted by echo-sounders is governed by the so-called sonar equation which is characterized by the same definitions and properties of the radar equation. Pulse compression techniques are usually not exploited in echo-sounders. Concerning this the principle of echo-sounding is very close to that of pulse radar [11], and therefore when dealing with an echo-sounder the pulse length determines both the amount of energy transmitted into the water (i.e. the maximum detectable length) and the range resolution.
- 4) The transducer plays the same role in echo-sounders as that of the antenna in pulse radars, e.g. the beam width depends on the acoustic wavelength and the size of the transducer. More in detail, for the same beam width a lower frequency will require a larger transducer.
- 5) The acoustic pulse travels through the water column and hits the seabed. The interaction with the sea floor results in reflection, transmission and scattering [8]. The reflected energy which returns to the transducer, i.e. the echo, is sensed by the transducer. The strength of the echo decreases rapidly with time, for that reason the echo is usually adjusted to compensate for echo decrease as a function of time.

According to these considerations it is reasonable to expect that different acoustic frequencies determine different types of systems [12]:

- Deep water systems work in waters deeper than 1500 meters with low acoustic frequencies ranging from 15 to 50 kHz and pulses longer than 10 ms.

- Shallow water systems work in water depths from 5 to 1500 m using frequencies from 50 to 200 kHz and pulse lengths from 1 ms to 10 ms.
- High-resolution systems work in very shallow waters (up to a few tens of meters) at frequencies higher than 200 kHz and pulse length shorter than 1 ms. They are used for local studies (i.e. ports and bays) and are typically characterized by small beam width ($< 2^\circ$).

State-of-the-art single-beam echo-sounder implementation also includes inertial sensors with heading sensor (usually a gyro or fluxgate compass) or inertial sensors with the integration of highest accuracy differential Global Positioning System (GPS) information (e.g. GPS receivers able to work in RTK mode) in order to achieve accurate attitude and position estimates. In this way it is possible to guarantee sub-decimetre accuracy in hydrographic surveying over shallow waters [10]-[12].

The main drawback of single-beam echo-sounder, in wide area coastal bathymetry, hence, does not deal with the overall accuracy but is specifically related to the way bathymetric surveys are performed: in situ measurements by specific acquisition campaigns have to be conducted. These ship campaigns are in general time consuming and expensive. In addition difficulties in performing in situ measurements can be met in specific regions, such as estuaries, due to strong currents. Finally those difficulties are increased notably in applications relevant to the monitoring of bathymetric changes.

1.2.2 Light Detection and Ranging (LIDAR) systems

LIDAR (“Light Detection and Ranging”) is an active remote sensing technology that uses light in the form of pulsed radar to measure distances [13], [14]. It is similar to radar but uses laser light pulses instead of radio waves [14]. Together with additional data collected by the airborne system, LIDAR generates precise, three-dimensional information about the shape of the Earth.

LIDAR technology was developed over 40 years ago as ground-based method to study and map atmospheric composition and structure [14]. During the 1980s, the development of GPS opened new possibilities and the first airborne LIDAR systems were introduced. During the early 1990s decimetre accuracies began to be achieved thanks to the improvement of the Inertial Measuring Units (IMU) or Inertial Navigation Systems (INS) technology. Nowadays, the most commonly used platforms for acquiring LIDAR data are airplanes and helicopters thus assuring quick and easy coverage over broad areas [13].

Despite they are extensively used for topographic measurements, LIDAR systems represent a well-established technology for bathymetric purposes in coastal area providing seamless, contiguous coverage between land and sea [14]. They basically consist of a laser, a scanner, a GPS receiver and a set of gyroscopes. Topographic LIDAR typically emits near-infrared pulses to map the land, while bathymetric LIDAR emits also green light pulses to investigate seafloor morphology [13], [15]. Indeed, while a lower frequency infrared pulse is reflected off the sea surface, a higher frequency green laser penetrates through the water column and reaches the bottom. Part of the signal is reflected off the seabed and bathymetric LIDAR determines water depth by measuring the time delay between the transmission of the pulse and its return signal [16], i.e. the echo, and knowing the light speed in air and water. Infrared light penetrates very little and can be used for detection of sea surface level. Latitude, longitude and elevation of the target can be computed by combining the information obtained about the relative distance, the angle at which the pulse was emitted, and the absolute location of the sensor above Earth surface [14].

LIDAR can potentially investigate seabed morphology for water depth up to 50 meters with good water clarity and bottom reflectivity [17]-[20]. Centimetre accuracies can be achieved [14], [16]. No depth measurements can be performed in case of high turbidity. With sampling rates greater than 150 KHz, it produces a densely spaced network of highly accurate georeferenced depth points that can be used to generate DEM of seabed [14]. Since it is an active remote sensing system, LIDAR is day-night independent. Actually, most LIDAR data are collected at night since air is usually clearer and there is less air traffic than in daytime [14]. Unfortunately, unlike radar, LIDAR system only works with clear sky. It cannot penetrate clouds, rain, or dense haze.

An example of operational bathymetric LIDAR is the Scanning Hydrographic Operational Airborne LIDAR Survey (SHOALS) [21] owned by the U.S. Army Corps of Engineers (USACE) and employed in cooperation with the U.S. Navy out of the Joint Airborne LIDAR Bathymetry Technical Center of Expertise [22], Mobile, Alabama.

Anyway, the operational cost for a LIDAR system is still relatively high and it is not practical to deploy this system in some areas of the world where updated bathymetric information is needed. Therefore, the bathymetric data obtained with this system are usually used for comparison with the results obtained from other remote sensing techniques.

1.2.3 Electro-optical instruments

Passive electro-optical instruments detect and measure the amount of solar radiation that is scattered back from the seabed and passes through the water column. Multispectral and hyperspectral technologies have demonstrated to give good results for bathymetric purposes [23]-[25]. Indeed, different wavelengths of light penetrate water at different depths since they undergo attenuation due to the interaction with the water column [26]-[28]. Longer wavelength light, i.e. red light, has a higher attenuation coefficient than short wavelengths [29], i.e. blue light. However, several additional factors contribute to light attenuation, such as water clarity, substances in the water column, seafloor colour and composition [30]. In most coastal areas, also algae, sediment, phytoplankton, inorganic particles and organic dissolved material negatively influence light penetration through sea water [23]. Therefore, a proper physical model for shallow-water reflectance evaluation is used and corrections able to take into account the water quality level and bottom reflectance variations are introduced to retrieve bathymetry [25], [31]. Moreover, also the effects due to sun glint, atmosphere, haze and thin clouds have to be taken into account for proper water depth estimation [25].

In clear sea water with bright sandy seabed, water depths up to 20 m can be detected [30], [32]. As the water becomes more turbid, with sediment or dense phytoplankton, much of the sunlight entering the water column is absorbed by the top layers of sea water and seafloor cannot be detected.

Using spaceborne passive electro-optical devices to infer shallow water bathymetry is quite effective and cost-efficient with respect to acoustic methods. Indeed, several ocean colour sensors are already operative for oceanographic research and, therefore, useful images can be easily obtained [33]. However, visible radiation is only available during daytime and just clear sky imagery can be analysed since visible light cannot pass through clouds. This means that variations in seabed morphology that occur on a short timescale could not be detected and the achievable time frequency of image acquisition is difficult to estimate since it depends on the specific case, e.g. geographic area and season. Moreover, also when good sky conditions are met, bathymetric retrieval can be prevented by sea water turbidity thus increasing uncertainty on the bathymetric data acquisition time frequency achievable with the passive electro-optical method.

1.3 SAR-based bathymetry: a new approach

Since the first Synthetic Aperture Radar (SAR) was sent into orbit onboard the NASA's SEASAT satellite in 1978 [34], sea surface features related to the underwater bottom morphology have been identified on SAR images of sea surface. In the last decades, several studies have been conducted to understand and model these phenomena in order to retrieve bathymetric data [34]-[36]. Innovative techniques have been identified [37]-[39] but they still need additional research to be effectively used.

SAR microwave signals, whose wavelength is typically shorter than a few tens of centimetres, are able to penetrate into seawater only to a depth which is negligible in comparison to the electromagnetic wavelength [40]. This means that to all practical purposes it is possible to state that SAR signals are not able to penetrate sea surface and to reach seabed. SAR images are generated by signals backscattered from sea surface, i.e. sea surface echoes. Nevertheless, bathymetry can be retrieved from SAR data based on indirect processes. Indeed, under specific conditions, underwater morphology is able to modify the characteristics of sea surface and therefore to introduce modulations into SAR image intensity. These mechanisms are related to the hydrodynamic characteristics of sea motion and are not affected by the quality of the water. Hence, SAR bathymetry can be used independently from the clearness of the water.

Using SAR data to retrieve coastal bathymetry represents a promising alternative to conventional bathymetric techniques. Indeed, SAR is day-night independent and its functioning is not affected by clouds. SAR images can cover wide areas with high repetitiveness, which implies cost reduction with respect to traditional bathymetric surveys. Moreover, SAR-based bathymetric data retrieval is not affected by sea water clarity conditions. Obviously, the magnitude of such indirect surface effects decreases notably with the local depth thus limiting the applicability of SAR based bathymetry to shallow waters and coastal areas. Improvement and understanding of SAR-based techniques for bathymetric data retrieval can be a key-point to obtain up-to-date bathymetric maps for coastal regions with resolution sufficient to infer geological processes by measuring temporal variations in the seabed morphology.

Chapter 2

SAR Imaging of Sea

The present chapter deals with a crucial aspect of SAR-based bathymetry, that is proper sea surface modeling. Therefore, the main assumptions that need to be made are described and the main involved parameters are presented. Sea surface spectrum is introduced and the different types of sea surface waves are defined. A brief description of the Synthetic Aperture Radar (SAR) system is provided by introducing the main quantities and parameters involved in the bathymetric data retrieval from SAR image. Finally, the basics of SAR interaction with sea surface are explained and the different imaging mechanisms of sea surface features are presented.

2.1 The sea: waves and currents

Sea surface modeling is the starting point to quantify both SAR response from sea and the effects produced by bottom topography. Sea surface can be considered as a combination of many wave components characterized by different values of parameters such as amplitude, phase, direction of propagation, period, and wavelength. Each of these single components was generated by wind in a different region of the ocean or sea and has propagated to the location of observation.

When the assumption of small amplitude waves is made, a sinusoidal wave profile can be assumed to represent each wave component (See Fig. 2.1) [41]-[43]. Indeed, in theory any more complex profile can be obtained by the addition of several sinusoidal waves with different wavelengths. Under this assumption, several considerations about the path of each water particle can be made.

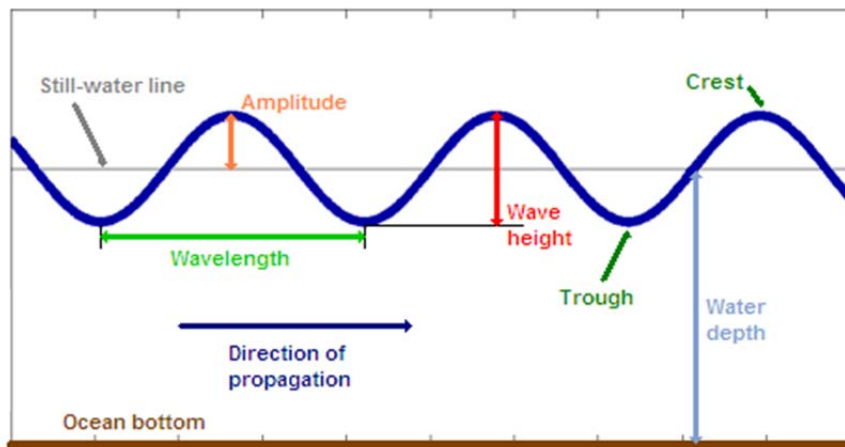


Fig. 2.1 Sinusoidal wave profile [44].

Hereinafter, the (x, z) coordinates define the position of a water particle, where x represents the horizontal position and z is the vertical position measured from the x axis. When water particles are on the undisplaced surface, they lie along the x -axis, i.e. they are characterized by $z = 0$. When the wave is propagating, at time t the water particle labeled (x, z) will be at a new position. This displacement can be modeled as the combination of a vertical and a horizontal displacement, i.e. $\eta_x(x, z, t)$ and $\eta_z(x, z, t)$, respectively. When a sinusoidal wave profile is assumed, the following statements can be made [43]:

- I. Sea water is in steady-state motion and, therefore, η_x and η_z harmonically vary with the angular frequency, ω , of the wave; the motion of each (x, z) particle can be considered as a superposition of two harmonic vibrations at right angles to each other.
- II. Since the motion of each (x, z) particle belongs to a traveling wave, the phase angles of both η_x and η_z are expected to contain a term related to $-kx$, where k is the wavenumber of the propagating wave; on the contrary, they are expected to be independent from the vertical position z , i.e. particles vertically stacked in equilibrium move in step with each other when there is a wave, both up-and-down and sideways.
- III. It is expected that η_x has its maximum value half way between a crest and a trough, i.e. where η_z is instantaneously zero, since the slope of the wave surface has its greatest value there and the maximum horizontal rearrangement of water must have occurred; the vertical and horizontal components of the vibration are supposed to be in quadrature with each other.
- IV. The movement of water particles is expected to become increasingly gentle as the depth beneath the sea surface increases; on the contrary, if an infinitely long canal is considered, no dependence on the position along the canal is expected; therefore, amplitudes of vertical and horizontal displacements are assumed to be dependent only on the vertical position z .

The aforementioned statements can be summarized by assuming η_x and η_z to have the following analytical expressions [43]:

$$\eta_x(x, z, t) = A_x(z) \sin(\omega t - kx) \quad (2.1)$$

$$\eta_z(x, z, t) = A_z(z) \cos(\omega t - kx) \quad (2.2)$$

where A_x and A_z are the amplitude of the horizontal and vertical oscillation, respectively.

Therefore, at any time t each water particle (x, z) satisfies the following equation [43]:

$$\left(\frac{\eta_z}{A_z}\right)^2 + \left(\frac{\eta_x}{A_x}\right)^2 = 1 \quad (2.3)$$

that is the equation of an ellipse having its principal axes lying along the η_x and η_z axes and cross at the point (x, z) . Therefore, the path traced by each water particle is an upright ellipse centered on the equilibrium position of the particle itself. Its size, shape, and whether it is flattened or elongated along the vertical direction, depend on the A_x and A_z values.

Since the assumption of small amplitude waves is made, equations (2.1) and (2.2) can be differentiated in order to obtain the velocities at the location (x, z) , although strictly it is the velocity at the location $(x + \eta_x, z + \eta_z)$. In this way, the following analytical expressions are retrieved [43]:

$$V_x(x, z, t) = -\omega A_x(z) \cos(\omega t - kx) \quad (2.4)$$

$$V_z(x, z, t) = -\omega A_z(z) \cos(\omega t - kx) \quad (2.5)$$

If the incompressibility condition (2.6) and the no-viscosity condition (2.7) are considered

$$\frac{\partial V_z}{\partial z} + \frac{\partial V_x}{\partial x} = 0, \quad (2.6)$$

$$\frac{\partial V_z}{\partial x} - \frac{\partial V_x}{\partial z} = 0, \quad (2.7)$$

together with the following two boundary conditions

- a) sinusoidal wave for $z = 0$,
- b) no vertical movement in correspondence of the seafloor, i.e. $z = -h$, where h is the water depth,

it is possible to obtain the following analytical expressions for the amplitudes $A_x(z)$ and $A_z(z)$ [43]:

$$A_x(z) = \frac{A \cosh[k(h+z)]}{\sinh(kh)} \quad (2.8)$$

$$A_z(z) = \frac{A \sinh[k(h+z)]}{\sinh(kh)} \quad (2.9)$$

Equations (2.8) and (2.9) give the shape of the ellipse covered by a water particle at a given depth. The ratio of its height to its length is equal to $\tanh[k(h+z)]$ and can never be greater than 1. All the orbital ellipses have their longer axis lying horizontally and become flatter as the depth increases. Indeed, orbits are completely flattened into horizontal movements in correspondence of seafloor and water particles just rub backwards and forwards. Also the horizontal displacement decreases as the depth increases, but more slowly than the vertical displacement since $\cosh[k(h+z)]$ decreases more slowly than $\sinh[k(h+z)]$ as z becomes more negative. Moreover, each water particle moves clockwise along its orbit as viewed from the positive y direction. Therefore, any water particle vertically beneath a wave crest moves

forwards, i.e. in the wave propagation direction, and any water particle beneath a trough moves backwards [43].

In deep water ($kh \gg 1$) and with reference to the water particles relatively close to the surface ($|z| \ll h$), some approximations can be made and the following expressions can be considered [43]:

$$\eta_x(x, z, t) \approx A e^{kz} \sin(\omega t - kx) \quad (2.10)$$

$$\eta_z(x, z, t) \approx A e^{kz} \cos(\omega t - kx) \quad (2.11)$$

The orbit flattening phenomenon is negligible for the water particles of interest and their orbits can be approximately considered circular at all depths, as shown in Fig. 2.2. Orbit diameter decreases exponentially as water depth increases and motion becomes negligible for depths much greater than $1/|k|$ [43].

On the contrary, in shallow water ($kh \ll 1$) different approximations can be made and the following expressions for the displacements can be considered [43]:

$$\eta_x(x, z, t) \approx A (1/kh) \sin(\omega t - kx) \quad (2.12)$$

$$\eta_z(x, z, t) \approx A (1+z/h) \cos(\omega t - kx) \quad (2.13)$$

The amplitude of the horizontal displacement is approximately the same at all depths and its value is very large compared with the surface wave amplitude, A . On the contrary, the amplitude of the vertical displacement decreases almost linearly from its surface value to zero on the seafloor. Therefore, shallow water waves are essentially longitudinal waves and this means that each water particle just moves back and forth along the wave propagation direction [43], i.e. x -axis, as shown in Fig. 2.2.

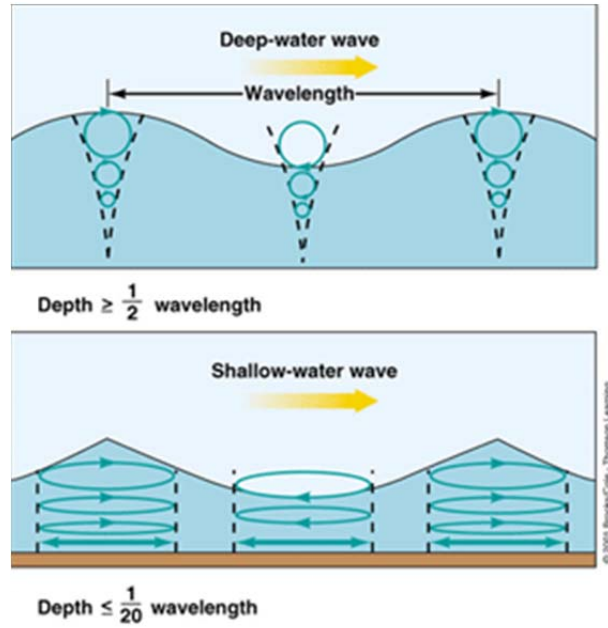


Fig. 2.2 Displacements of water particles when a swell wave propagates: (*top*) deep water depth; (*bottom*) shallow water depth [45].

When a wave is propagating on sea surface, the phase speed of the wave, c , i.e. the speed at which a crest moves, can be defined as [42]

$$c = \frac{\omega}{k} \quad (2.14)$$

where,

- ω is the frequency in [rad/s] at which the waves oscillates as measured by an observer fixed in the medium, i.e. $\omega = 2\pi f = 2\pi/T$ with f being the frequency in [Hz] and T the wave period in [s];
- k is the wavenumber measured in [rad/m] and represents how many cycles there are per unit distance at any instant, i.e. $k = 2\pi/L$ with L being the wave wavelength in [m].

Moreover, the group velocity, c_g , i.e. the energy propagation velocity, can be defined as [42]

$$c_g = \frac{\partial \omega}{\partial k} \quad (2.15)$$

Indeed, within a group of propagating waves of gradually varying wavenumber or frequency, troughs and crests normally travel at a different speed from the group itself, i.e. phase speed is different from group velocity [42].

The relationship between angular frequency and wavenumber is defined as the dispersion relation and it is established by the physical processes that govern wave propagation [41], [43].

In order to characterize waves and their energy distribution, a spectral approach is required. The energy of a monochromatic wave train is proportional to the square of the wave amplitude and the overall energy of the sea surface wave field can be assumed as the sum across all frequencies of the energy amount related to each of those individual monochromatic wave trains [41]. The distribution of the energy with respect to spatial frequency and wave number is called the sea surface spectrum [41].

Extensive studies have been performed to define and model the shape of sea surface spectrum and its dependence on wind. Several characteristic spectra have been defined, such as the one based on the Joint North Sea Wave Analysis Project (JONSWAP) experiment [41], [46]. Specifically, different spectra at different distances from the coast have been identified. However, each spectrum presents values close to zero at low frequencies, a steep rise up to reach the maximum value above a certain frequency threshold, and a decay at high frequencies [41]. When wind speed increases, it has been noticed that the height of the peak increases and the corresponding frequency threshold reduces [41]. This means that the stronger the wind is, the higher and longer the waves become. On the contrary, the shape of the high-frequency portion of the sea surface spectrum appears not to change with increasing wind, thus indicating that this part of the spectrum is saturated [41]. The performed studies [41] showed that when the wind blows it pumps energy into the higher frequency waves through differential pressure on the upwind and downwind faces. This phenomenon is balanced by some dissipation at very high frequencies but the most of the energy flows to lower frequencies, i.e. to longer waves, through non-linear wave-wave interactions [41]. It is worth to note that the longer the waves are, the more rapidly they are able to transport energy away from a certain location. Therefore, a maximum wavelength that can grow for a given wind speed can be identified.

Due to the significant variability in height and period, definitions of the different types of waves are based on statistical analyses. However, based on wave features and dynamics, three main kinds of waves can be defined [41], [47], namely capillarity waves, wind sea, and swell waves. Capillarity waves or ripples are wind-generated waves, characterized by very high frequency and irregular patterns. Surface tension is the dominant force and gravity effects are negligible. When the wind is blowing and the waves are growing in response, the sea surface tends to be confused and a wide range of heights and periods is observed. Such waves are called wind seas, or often, just sea. These waves are more regular and longer than capillarity waves, but still include wind-generated high frequency components. Swell waves, on the contrary, generate in a certain region of sea surface as the result of intense and adverse weather conditions. Their propagation is dominated by gravity and is not significantly affected by wind. For this reason, they are able to propagate far from their region of origin and can continue travelling for several

days. Swell are characterized by long period and long individual crests which tend to be uniform in height, period and direction of propagation [41], [48], [49].

The presence of currents, generated by either tidal forces or winds, complicates the modeling because non uniform currents can interact with the wave spectrum producing a variation of sea wave fields [37], [50].

2.2 Synthetic Aperture Radar (SAR)

Synthetic Aperture Radar (SAR) is an active sensor that emits radiation in the microwave region of the spectrum (see Figs. 2.3-2.4). It can potentially work anytime, regardless of the time of day or weather conditions.

Satellites are the most common platforms for SAR systems. The path followed by a satellite is referred to as its orbit and the area imaged on the surface is referred to as the swath. Depending on the considered sensor and mode, swaths can be less than 1 m or tens of kilometers wide. The revisit period is the interval of time required for the sensor to image the same area on the ground. However, it can be different from the orbit cycle time, i.e. the interval of time required for the satellite to complete its orbit cycle, since steerable sensors can be used thus making the revisit time less than the orbit cycle time [51].

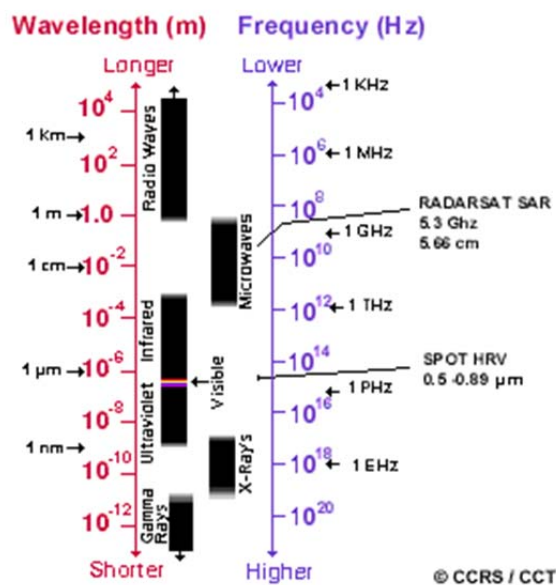


Fig. 2.3 The electromagnetic spectrum [51].

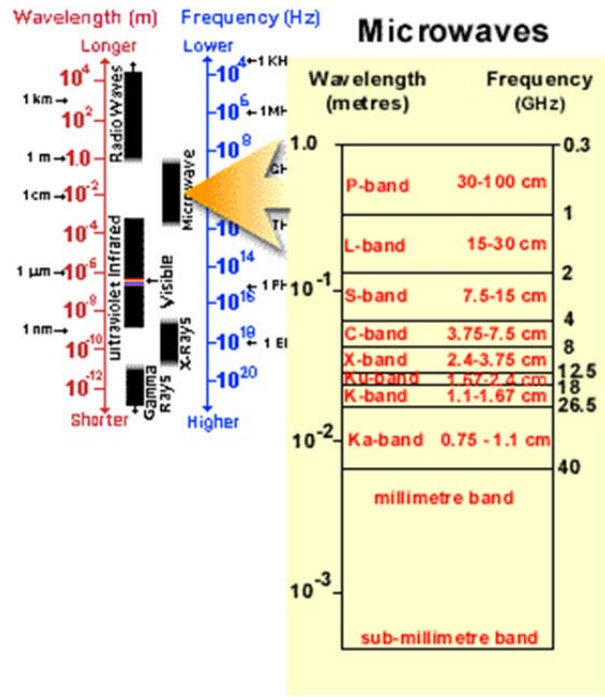


Fig. 2.4 The microwave region of the electromagnetic spectrum and its different bands [51].

The SAR system was first introduced by Carl Wiley in 1951 [52] and it fundamentally consists of a transmitter, a receiver, an antenna, and an electronics system to process and record the data [51]. The transmitter generates successive short frequency modulated pulses of microwave radiation (marked with A in Fig. 2.5) at regular intervals which are focused by the antenna into a beam (marked with B in Fig. 2.5). The radar beam illuminates the surface obliquely at a right angle to the motion of the platform. The antenna receives a portion of the transmitted energy reflected, i.e. backscattered, from various objects within the illuminated beam (marked with C in Fig. 2.5). By measuring the time delay between the transmission of a pulse and the reception of the backscattered echo from different targets, their distance from the radar and thus their location can be determined [51].

The platform travels forward along the flight direction with the nadir directly beneath the platform. Range refers to the across-track dimension perpendicular to the flight direction, while azimuth refers to the along-track dimension parallel to the flight direction (see Fig. 2.6). The incidence angle is the angle between the radar beam and ground surface (marked with A in Fig. 2.7) which increases, moving across the swath from near to far range. The look angle is marked with B in Fig. 2.6. At all ranges the radar antenna measures the radial line of sight distance between the radar and each target on the surface. This is the slant range distance (marked with C in Fig. 2.7). The ground range distance (marked with D in Fig. 2.7) is the true horizontal distance along the ground corresponding to each point measured in slant range [51].

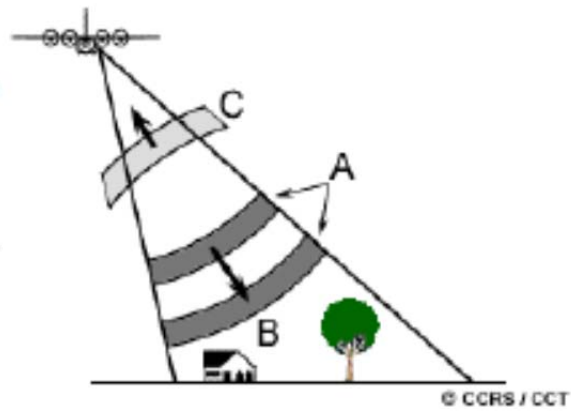


Fig. 2.5 SAR functioning: A marks pulses of microwaves, B is the radar signal beam, C is the backscattered signal [51].

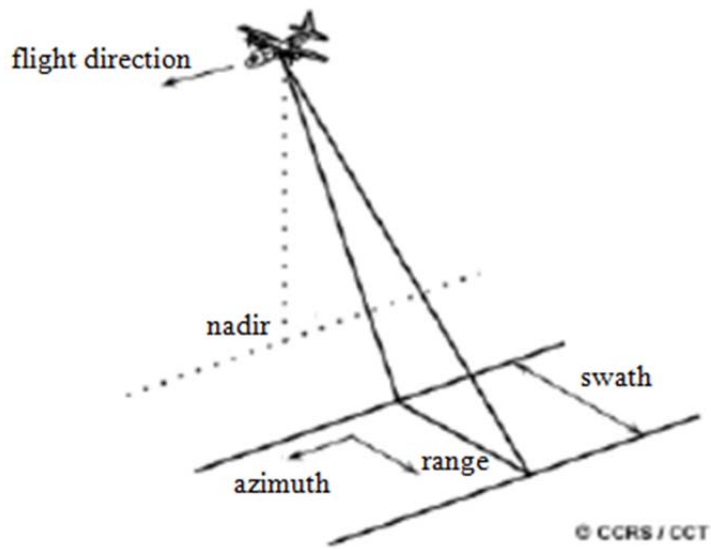


Fig. 2.6 SAR viewing geometry [51].

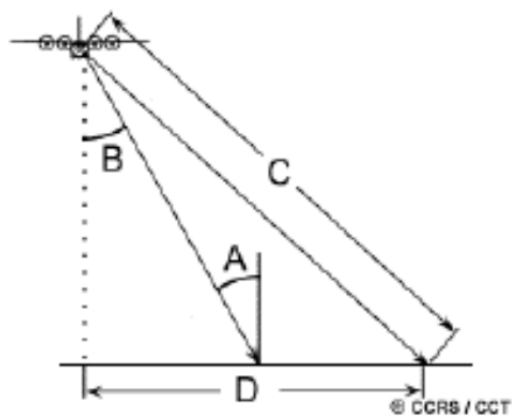


Fig. 2.7 SAR viewing geometry: A is the incidence angle, B is the look angle, C is the slant range [51].

Basically SAR works as a chirp radar exploiting both amplitude and phase of the received echoes [53]. The antenna has sufficiently wide beam width in the along-track direction so that a certain target is illuminated by a number of pulses (usually on the order of thousand for spaceborne SARs) [54]. Those pulses are reflected from the scene thus generating a sequence of echoes that are collected by the receiver. The ensemble of locations of the SAR antenna during the illumination of a certain target is referred as synthetic aperture of the system. Since the velocity at which the platform moves is very short with respect to the velocity of propagation of the signal, the start-and-stop approximation can be adopted [55]. Specifically, the SAR antenna can be considered to be stationary during signal propagation along the slant range direction and it moves on the next position only after the echo is received. Under the assumption of stationary target, pulse compression techniques [54], [56], [57] are used to exploit the frequency modulation of the transmitted pulses in order to enhance the range resolution. As result, the SAR range resolution is inversely proportional to the length of the frequency modulation bandwidth. At the same time, the Doppler history due to the relative motion between the SAR antenna and the target is tracked and compressed so to enhance the azimuth resolution. As result, the SAR azimuth resolution is directly proportional to SAR antenna length [54], [56], [57]. This means that a short antenna is required to improve azimuth resolution thus being an important advantage of SAR with respect to Real Aperture Radar (RAR) requiring large antennas to improve azimuth resolution [56]. Therefore, as the platform moves forward along the orbit, the sensor records and processes the backscattered signals thus building a two-dimensional image of the surface [51].

The microwave region of the spectrum used by SAR systems is divided in several ranges of wavelength, i.e. bands (see Fig. 2.4). Different bands are used by SAR sensors for different purposes and to detect different targets. The brightness of features on a radar image is dependent on the amount of the transmitted energy that is returned back to the radar from targets on the surface. The magnitude or intensity of this backscattered energy is dependent on how the radar energy interacts with the surface, which is a function of several variable or parameters, such as specific characteristics of the SAR system (frequency, polarization, viewing geometry, etc.) [51].

2.3 SAR imaging of sea surface

The backscatter patterns depicted by SAR image of sea surface are a measure of the sea surface roughness encountered by the transmitted microwaves. Specifically, this mechanism is

regulated by the amplitude of short waves which have a wavelength matching the Bragg condition, or up to an order of magnitude longer [42]. According to the Bragg scattering theory, the backscattered radar power or the Normalized Radar Cross Section (NRCS), σ_0 , are proportional to the spectral energy density of those waves which travel away or towards along the SAR look direction and which have spatial wavelength λ_B that is related to the radar wavelength, λ , and to the incidence angle, θ , by the Bragg resonance condition [41], [42]

$$\lambda_B = \frac{\lambda}{2 \sin \theta} \quad (2.16)$$

The small capillarity waves which satisfy the Bragg condition (2.16) are called Bragg-waves. According to the Bragg scattering theory, only Bragg-waves contribute to the SAR response since they generate constructive interference in the direction of the sensor [39]. Therefore, in the case of total lack of wind the sea surface is smooth and reflects the SAR signal aside thus obtaining a black image of sea surface. However, due to uniformly distribution of small-scale waves, the Bragg condition is nearly always satisfied.

Features of an ocean phenomenon clearly appear on SAR image only because surface roughness is modulated by the phenomenon itself. Contributions from different portions of sea wave spectrum combine in a nonlinear way to generate the final SAR image [58], [59]. Therefore, due to the non-linearity of the imaging mechanism, wave patterns depicted in SAR images are not the true sea surface waves, i.e. SAR image is not a picture of sea surface [47]. However specific conditions exist in which linear imaging can be assumed [59].

Specifically, there are three possible mechanisms for SAR imaging of swell waves, i.e. hydrodynamic modulation, tilt modulation and velocity bunching. These different mechanisms may reinforce, compete, or complement each other depending on the direction along which swell waves are travelling relative to the SAR viewing direction [41], [42].

It is worth to note that hydrodynamic modulation and velocity bunching imaging mechanisms also activate when gradients of sea surface current are present at the moment of SAR image acquisition [32], [41], [60] i.e. also when no swell waves are propagating on sea surface.

Hydrodynamic modulation

When a swell wave propagates, water particles near sea surface describe a circular path. As the swell crest goes past an observer, a particle floating at the surface is seen to move forward in the same direction as, but slower than, the wave. As the swell trough passes, the particle moves in the opposite direction [41]. Therefore, at a given instant there are patterns of horizontal

convergence and divergence of water particles at the sea surface. Their effect is increasing and decreasing, respectively, the amplitude of the Bragg-waves, thus producing a modulation of surface roughness. In turn, this causes a modulation of radar backscatter thus generating patterns of dark and light on SAR image. The higher echoes (higher sea surface roughness) are expected on the rising face of swell, where the convergence occurs, whereas the lower returns (lower sea surface roughness) are expected on the trailing edge of swell. Since swell waves pass through a whole cycle in about 10 s, there is little time for the Bragg-waves to return to the equilibrium conditions [41]. Therefore, the phase of the SAR brightness is expected to match the location of maximum convergence [41].

This imaging mechanism works only for swell waves propagating, or having a significant component of their motion, in the range direction since the Bragg-waves affecting radar backscatter are those travelling in that direction [41]. However, depending on whether swell are propagating towards or away from the SAR sensor, there is a 180° phase shift of modulation on the image since the hydrodynamic modulation relates the maximum backscatter to the rising edge of the wave. On the contrary, swell propagating in the azimuth direction still modulates the surface ripples but hardly affects those ripples propagating in the range direction which contribute to the Bragg scattering.

The hydrodynamic modulation also enables surface currents to be imaged by SAR. Indeed, in the absence of currents the sea surface roughness is determined by the local wind stress and, therefore, the roughness detected by SAR is expected to be uniform in a region of uniform wind stress [41]. On the contrary, in regions of varying currents the modulation of the wavelength and amplitude of sea surface waves causes their energy distribution to deviate from the equilibrium spectrum [41] thus modulating the radar backscatter cross section. Specifically, the wave energy which determines sea surface roughness is forced by the convergence of currents at the sea surface to be stronger than its equilibrium value for a certain wind velocity [41]. Conversely, a current divergence reduces the energy [41]. Therefore, convergence and divergence regions result to be bright and dark patches on the SAR image. Detection of their spatial distribution reveals the horizontal structure of the underwater ocean process that produces the current field. Under suitable conditions, this can yield information also about the magnitude of the phenomenon.

Tilt modulation

This imaging mechanism is based on the strong dependence between the magnitude of SAR echo and the local incidence angle due to the presence of swell wave. Specifically, the

backscatter decreases as the incidence angle increases. This means that SAR echo is stronger for the swell side facing the radar and weaker for the side facing away (see Fig. 2.8). Sea surface tilt associated with swell waves can be of the order of $\pm 20^\circ$ and so there can be significant modulation of the backscatter [41]. It is worth to note that the tilt modulations mechanism detects swell waves even if surface roughness is completely uniform and unmodulated. This imaging mechanism can be considered unique to swell waves [41] and it applies only to range-travelling waves. Indeed, for azimuth travelling swell waves there is only a very weak second order change in the SAR incidence angle [41].

Hydrodynamic modulation and tilt modulation reinforce each other in the imaging of range-travelling swell waves propagating toward the radar sensor. On the contrary, when swell travel away from the radar sensor the two mechanisms oppose each other and weaken the overall modulation of backscatter by swell. Indeed, while the tilt modulation depends only on the instantaneously static shape of the surface, the effect of hydrodynamic modulation on SAR backscatter strictly depends on whether swell are propagating towards or away from the sensor.

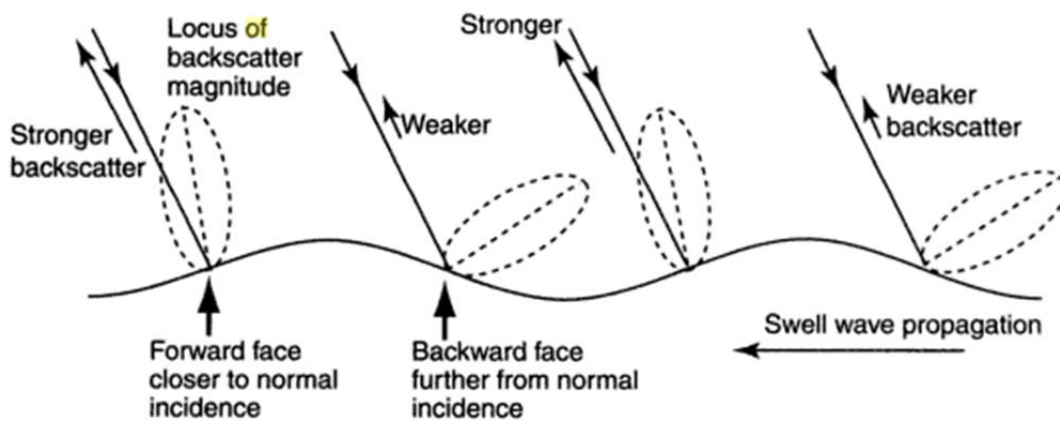


Fig. 2.8 Tilt modulation mechanism for imaging of swell waves [41].

“Velocity bunching” modulation

The two imaging mechanisms considered so far can only detect swell waves propagating with a significant component of their velocity in the range direction. On the contrary, the "velocity bunching" modulation allows to image waves propagating in the azimuth direction. This mechanisms is based on the relative motion between the SAR sensor and the Bragg-waves, which move as consequence of swell waves propagation. This relative motion affects the

Doppler shift of the SAR echo thus altering the way the SAR azimuth compression process reconstructs the image of sea surface during the data processing.

Specifically, due to Bragg-waves riding up and down on the back of the propagating swell waves, sea surface particles describe circular paths. This orbital motion has a component towards the radar which sinusoidally varies from positive to negative across the swell wave profile. For azimuth travelling swell waves, the vertical part of particle motion has a component in the slant range direction. This results in the scattered energy from that part of the wave profile being assigned to an azimuth location in the image which is shifted forwards or backwards depending on the sign and magnitude of the motion of the surface relative to the radar [41]. The overall effect is to increase brightness in parts of the SAR image to which the signal is misassigned, and to reduce it in the regions of the image corresponding to the true location of the mis-located scattering element [41].

When swell waves are travelling in the negative azimuth direction, scattering elements on the rising swell face are shifted forward in azimuth, tending to locate them towards the position of the swell crest on the SAR image; similarly, scattering elements on the falling swell side are shifted backwards in azimuth, tending to locate them towards the position of the same swell crest [41]. Therefore, the overall trend throughout the whole swell wave profile is to move the scattering elements, i.e. "to bunch" them, towards the crests and away from the troughs (see Fig. 2.9). The result is a swell-like distribution of image brightness, maximum over crests and minimum over troughs, which allows the azimuth travelling waves to be imaged [41]. On the contrary, if the swell waves are travelling in the positive azimuth direction the image brightness increases over troughs and diminishes over crests.

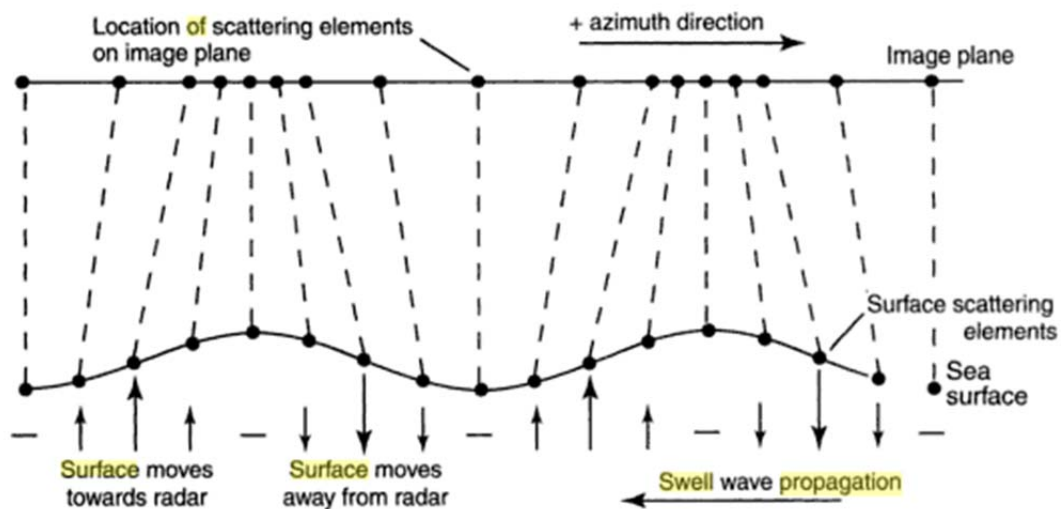


Fig. 2.9 The velocity bunching process [41].

This imaging mechanism does not work for range travelling swell waves since the azimuth shift caused by the vertical surface movement occurs along directions parallel to the crests and troughs. The overall density of the scattering elements in the image plane does not change and there is no apparent effect on the SAR image [41].

"Velocity bunching" modulation is a non-linear process [41] and it works as imaging mechanism as long as the shift is small. If the maximum shift is larger than $\frac{1}{4}$ of the swell wavelength, the scattering elements from one face of the wave are shifted beyond the next trough or crest. When the shifts increase to beyond $\frac{1}{2}$ of the swell wavelength, the integrated contribution of all the shifted elements becomes increasingly less coherent [41] (see Fig. 2.10).

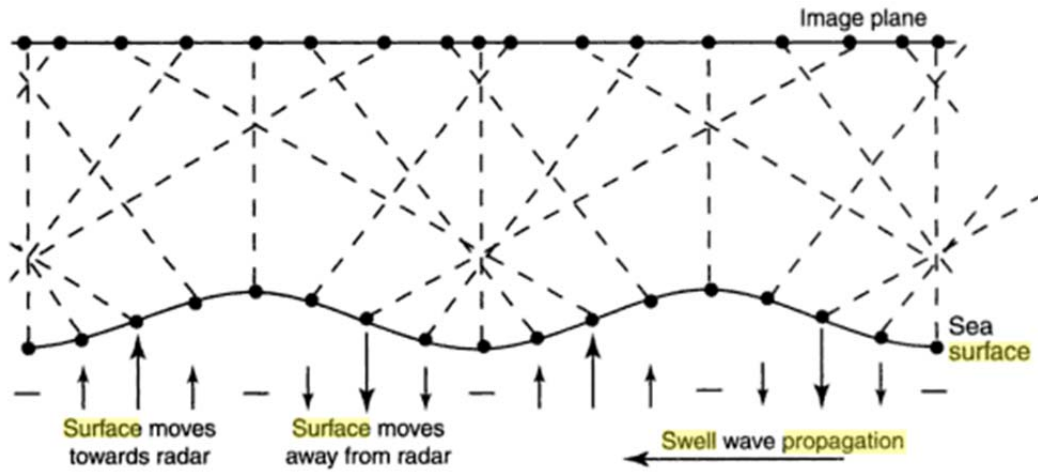


Fig. 2.10 The velocity bunching process for large amplitude waves [41].

Being u_R the relative motion between surface and radar, and $K_{vb} = \frac{RV_{sat}}{V_{gr}^2}$ a fixed quantity for a given satellite orbit with range R , speed of the sensor V_{sat} , and speed of the footprint over the ground V_{gr} , the distance a scatterer is shifted on the image is [41]

$$x_{shift} = u_R K_{vb} \quad (2.17)$$

For a swell wave of amplitude A , period T and wavelength λ , the maximum value of u_R is $(2\pi A/T) \cos \theta$, where θ is the incidence angle and g is gravity acceleration. Therefore, in order to have an azimuth shift shorter than half the swell wavelength, the following condition must be satisfied [41]

$$A < \frac{T\lambda}{2\pi K_{vb} \cos \theta} = \frac{gT^2}{8\pi^2 K_{vb} \cos \theta} \quad (2.18)$$

This relationship implies that there is a high-frequency cut-off for the detection of azimuth travelling swell waves. For satellite SARs this is normally taken to be around 11 s period or 200 m in wavelength, which is very limiting for coastal waters that have short fetches where the important waves have periods between 8 and 10 s [41]. However, some empiric equations can be considered to estimate the minimum detectable value of wavelength for swell waves travelling along the azimuth direction (see Section 4.1.3).

Chapter 3

SAR-Based Bathymetric Techniques and Models

The present chapter presents the SAR-based bathymetric techniques found in the scientific literature. Two different techniques are investigated: the wave-based bathymetric technique and the current-based bathymetric technique. For each of them, several models are shown and discussed. Finally, a selection is performed for SAR-based bathymetry.

3.1 Wave-based bathymetric technique

Changes in swell waves characteristics have been used since World War II to indirectly infer bottom depths [61]. Indeed, as swell waves travel from deep to shallow water, their shape alters. Their speed decreases and their wavelength shortens. The wave height increases due to conservation of energy and, therefore, their steepness rises. This process is called wave shoaling [39]. As consequence, when swell crests are not aligned with contour lines of bottom topography, they realign themselves as a result of decreasing water depths. Indeed, varying depths along a swell crest cause the crest to travel at different phase speeds, with those parts of the wave in shallower water being more decelerated than those in deeper water. This results in a changing of swell travel direction and takes place until the wave crests have become parallel to the shoreline or the wave breaks (see Fig. 3.1). This process is called wave refraction [39]. Therefore, if the rays are considered, i.e. the lines normal to wave crests between which a fixed amount of energy flux is contained, it can be seen that they converge on local shallows and shoals. Investigation and quantitative estimation of these processes allow bathymetric features to be sensed. In the case of not extreme wind speed and sea state, absence of currents, and swell patterns characterized by wavelengths that are sufficiently far from the cut-off conditions [39], experimental results demonstrate that the swell wavelengths imaged by SAR represent an unbiased estimate of the true swell wavelengths [32]. Therefore, under those conditions linear imaging can be assumed [59]. However, proper hydrodynamic modelling is required to relate variations of swell waves characteristics to sea bottom features.

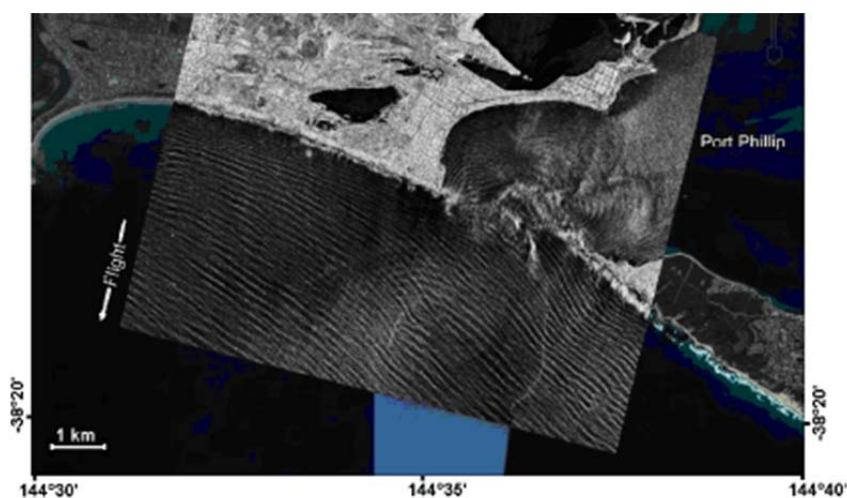


Fig. 3.1 TerraSAR-X Spotlight image acquired over entrance of Port Phillip in Melbourne, on 17 March 2008 at 19:45 UTC [39]. Refraction and shoaling phenomena of swell waves are clearly visible.

It is worth to note that the same effects of refraction and wave height variation also occur in presence of sea surface current variations since wave phase speed also changes with the ambient current. Specifically, in the case of current propagating in the opposite direction of the propagating swell waves, wave height increases and their wavelength decreases, i.e. swell waves steepen similarly to the shoaling phenomena which occurs when water depth decreases.

3.1.1 Linear Dispersion Relation

Most of the wave-based bathymetric applications used so far rely on the linearized version of the finith depth dispersion equation for swell waves, that is a simplyfied version of the theoretical relationship between wavelength, period and water depth [49] under the assumption that the wave height is much smaller than the wavelength. It relates to the Airy wave theory (often referred to as linear wave theory) which provides a linearized description of swell propagation on the surface of a homogeneous fluid layer with high-enough accuracy for many purposes [49].

In order to derive the analytical expression of the swell waves linear dispersion relation, the Navier-Stokes equations for a two-layer fluid must be considered. Indeed, the atmosphere/ocean system consists of fluids of two densities, air and water. However, due to the density of air being much smaller than the density of water, the linearized Navier-Stokes equations for a one-layer fluid in a gravitational field can be considered to describe swell waves propagation [49]. Moreover, a number of assumptions can be made [49]: since the inverse Coriolis parameter is much larger than a typical swell wave period, the Coriolis force is normally negligible; swell waves can be considered free to first order, that is dissipation and forcing by the environment can be neglected; for the longer waves, i.e. having wavelength larger than 1 m, viscosity and surface tension can also be neglected. Therefore, the Euler equation for a one-layer fluid can be considered [49]. A further simplification can be made, because waves happen to be irrotational [49] and the flow can be described by a velocity potential. In addition, water is nearly incompressible [43], so that the flow is also divergence free, which implies that the velocity potential satisfies Laplace's equation.

From an analytical perspective, the equations reported hereinafter have to be considered [49].

The two-layer full nonlinear Navier-Stokes equations read [49]

$$\nabla_i u_i = 0$$

$$\partial u_i / \partial t + u_j \nabla_j u_i = -(1/\rho) \nabla_i p - g \delta_{3i} + \nabla_j \tau_{ij}, \quad i = 1, 2, 3, \quad (3.1)$$

$$\rho = \begin{cases} \rho_a, & z > \eta \\ \rho_w, & z < \eta \end{cases}$$

where:

- (u_1, u_2, u_3) is the velocity vector;
- t is the time;
- (x_1, x_2, x_3) are the three-dimensional space coordinates;
- $p(x_1, x_2, x_3, t)$ is the pressure;
- $\rho(x_1, x_2, x_3, t)$ is the density;
- g is the acceleration due to gravity;
- τ is the stress tensor;
- ρ_a is the density of air;
- ρ_w is the density of water;
- $\delta_{3i} = 0$ except for $i = 3$, when it equals 1.

Velocities and forces, i.e. pressure and tangential stress, are continuous at the interface. A particle on either side of the surface will move from $(\mathbf{x}, z = \eta(\mathbf{x}, t))$ to $(\mathbf{x} + \Delta\mathbf{x}, z + \Delta z = \eta(\mathbf{x} + \Delta\mathbf{x}, t + \Delta t))$ in time Δt , with $\Delta\mathbf{x} = \mathbf{u}\Delta t$ and $\Delta z = w\Delta t$. Therefore, the kinematic boundary condition is obtained:

$$\eta(\mathbf{x} + \Delta\mathbf{x}, t + \Delta t) = \eta(\mathbf{x}, t) + w\Delta t \quad (3.2)$$

or equivalently

$$w_+ = w_- = \partial\eta/\partial t + \mathbf{u} \cdot \nabla\eta = D\eta/Dt \quad (3.3)$$

where the subscripts + and – indicate that the argument has to be taken just above or below the interface.

Regarding the boundary conditions, in water of finite depth the orthogonal velocity component at the bottom should vanish [49]. Moreover, due to the typical oceanic dimensions being very much larger than the typical wavelength, the basin is considered of infinite size [49]. If viscosity is neglected, the Euler equations in which the stress terms have been dropped can be considered. Continuity of stress at the interface is no longer required, which allows the parallel velocity at

the interface to be discontinuous. This approximation can be made in air and water. A further approximation of the air motion is to neglect it altogether.

It is worth to note that for very short waves the assumption of continuity of pressure is not correct since the effect of surface tension becomes important. At high wind speeds, when multiple whitecaps, bubbles and spray appear, the assumption on the existence of a well-defined sea surface η breaks down and the equations lose their meaning [49].

The general nonlinear equations can be simplified by linearization. Wave steepness, considered to be a small parameter, can be defined in a general way by assuming that η is characterized by both a vertical and a horizontal length scale, in such a way that their ratio is small. This ratio is then taken as the expansion parameter. To obtain the linearized equations one makes a formal expansion around zero [49].

The linearized Euler equations are obtained from eq. 3.1 by assuming [49]

$$\begin{aligned}
 & \cdot \quad \tau = \rho_a = 0: \\
 & \cdot \quad \nabla \cdot \mathbf{u} + \partial_z w = 0, \\
 & \cdot \quad \partial_t \mathbf{u} = -\nabla p / \rho, \\
 & \cdot \quad \partial_t w = -\partial_z p / \rho - g, \\
 & \cdot \quad \partial_t \eta = w, \quad z = 0, \\
 & \cdot \quad p = p_{atm} = 0, \quad z = 0
 \end{aligned} \tag{3.4}$$

The last equation expresses continuity of pressure at the surface. The atmospheric pressure is taken to be equal to zero.

The solution of (3.4) is irrotational and a potential flow description can be used. The velocity potential $\Phi(x_1, x_2, x_3)$ can be introduced with

$$u_i = \Phi_{x_i}, \quad i = 1, 2, 3 \tag{3.5}$$

where the short hand notation is used for differentiation. The linearized potential flow equations read

$$\Phi_{x_1 x_1} + \Phi_{x_2 x_2} + \Phi_{zz} = 0, \quad z < 0, \tag{3.6}$$

$$\left. \begin{aligned} \eta_t &= \phi_z \\ \phi_t + g\eta &= 0 \end{aligned} \right\} z = 0 \tag{3.7}$$

The second boundary condition makes use of Bernoulli's relation to express continuity of pressure at the surface. Since pressure is zero just above the water, it should be zero just below the sea surface.

Eulerian coordinates have been used by specifying the velocity of the fluid in fixed space points as a function of time. However, since the fluid flows, Lagrangian coordinates should be preferred specifying the velocity of a fluid element while it flows. Moreover, for free surfaces like sea, Lagrangian coordinates have certain advantages and are often used in wave studies. However, in a linear approximation, Lagrangian coordinates are identical with Eulerian ones, so it does not matter which are used.

For deep water waves the assumption $\Phi \rightarrow 0$ as $z \rightarrow -\infty$ is made. In shallow water, for a flat bottom at depth $z = -h$, the following assumption can be considered instead [49]

$$\phi_z = 0, \quad z = -h \quad (3.8)$$

The linearized equations can be analysed thus obtaining [49]

$$\phi = -i\omega_{\pm} a \frac{\cosh k(z+h)}{k \sinh(kh)} e^{i(\mathbf{k}\cdot\mathbf{x} - \omega_{\pm}t)} \quad (3.9)$$

and the dispersion relation becomes [49]

$$\omega^2 = gk \tanh kh \quad (3.10)$$

Equation 3.10 can be generalized as [49]

$$\omega = \sqrt{gk \tanh kh} + \vec{k} \cdot \vec{u}_c \quad (3.11)$$

where:

· \vec{u}_c is the near surface current;

· $\omega_D = \vec{k} \cdot \vec{u}_c$ is the Doppler frequency and indicates the effect of the near-surface current which leads to a frequency shift of ω_D .

It is therefore clear that angular frequency ω and wavenumber k , or equivalently period T and wavelength L , are not independent. Surface gravity waves are dispersive waves, i.e. they exhibit frequency dispersion. This means that each wavenumber has its own frequency and phase speed

$$c = \omega/k.$$

When $h > 1/2 L$, i.e. in deep water, the dispersion relation is simply [49]

$$\omega = \sqrt{gk} \quad (3.12)$$

and the phase speed of the waves is hardly influenced by depth

$$c = \sqrt{\frac{g}{k}} = \frac{gT}{2\pi} \quad (3.13)$$

$$c_g = \frac{1}{2} \sqrt{\frac{g}{k}} = \frac{c}{2} \quad (3.14)$$

Therefore, the phase speed in deep water is only dependent on the swell period thus causing longer, lower-frequency waves propagate faster than the shorter, higher-frequency waves, and leading to dispersion of the wave components, which does not depend on the wavelength.

Similarly, when $h < 1/20 L$, i.e. in shallow water, the dispersion relation is simply [49]

$$\omega = k\sqrt{gh} \quad (3.15)$$

and

$$c = \sqrt{gh} \quad (3.16)$$

$$c_g = c = \sqrt{gh} \quad (3.17)$$

The phase speed of the waves is only dependent on water depth and no longer a function of period or wavelength. This means that all waves travel at the same speed independently of their wavelength, i.e. they are not dispersive, and there is no relation between wavelength and depth. The shallower the water the slower the waves, leading to refraction of waves over shallow sandbars or sloping beaches.

Therefore, standard linear dispersion relation can be used to describe the wave behaviour in intermediate water because ocean surface waves begin to feel bottom if $h < 1/2 L$.

However, for short wavelengths surface tension contributes to restoring forces which control the wave propagation [49]. Indeed, at wavelengths less than about 5 mm, surface tension is the dominant restoring force and gravity effects are negligible. The resulting wave is called capillarity wave and is characterised by the dispersion relation

$$\omega^2 = \gamma k^3 \quad (3.18)$$

where γ is the surface tension divided by the water density. The corresponding phase and group velocities are

$$c = \sqrt{\gamma k} \quad (3.19)$$

$$c_g = \frac{3}{2} \sqrt{\gamma k} \quad (3.20)$$

Capillarity waves are also dispersive but now shorter wavelength waves propagate faster than longer waves.

At intermediate wavelengths of a few centimetres, which is the most relevant scale to K-, X-, and C-bands radar backscattering, both gravity and surface tension influence wave propagation. Thus the dispersion relation is [42]

$$\omega^2 = gk + \gamma k^3 \quad (3.21)$$

Therefore, for the intermediate depth case, the full dispersion relation including the possibility of capillary waves is

$$\omega^2 = (gk + \gamma k^3) \tanh(kh) \quad (3.22)$$

3.1.2 Non-linear or finite-amplitude wave theories

Development of further wave theories besides the linear one has been necessary for a better description of swell wave propagation for more specific applications. Indeed, in coastal regions and for long waves in intermediate depths the ratio of the depth over the wavelength becomes relatively small and the waves are considered weakly dispersive and weakly non-linear. Moreover, wave crests become higher above the mean water line than the troughs are below it. Therefore, depending on the final application, the linear wave theory can be inadequate [60] since it provides just a useful first approximation to the swell wave motion in such situations.

The nonlinear theories can also describe phenomena such as mass transport where there is a small net forward movement of the water during the passage of a wave. Therefore, water waves are not considered pure oscillatory waves any more, i.e. water particles do not describe circular orbits that are closed or nearly closed for each wave period because they advance with the wave and do not return to their original position.

A perturbation solution using successive approximations can be developed to improve the linear theory where each additional term in the series is a correction to preceding terms [48]. The obtained result has revealed to be often in a better agreement between theoretical and observed waves.

When the wave slope $\epsilon = kA$ is assumed to be small, the perturbation solution can be developed as a power series in terms of kA and it is expected to converge as more and more terms are considered in the expansion. The perturbation expansion for velocity potential Φ may be written as [48]

$$\Phi = \epsilon\Phi_1 + \epsilon^2\Phi_2 + \dots \quad (3.23)$$

Each term in the series is smaller than the preceding term by a factor of order kA . In this expansion, Φ_1 , is the first-order theory (linear theory), Φ_2 is the second-order theory, and so on.

Substituting eq. 3.23 and similar expressions for other wave variables, i.e. surface elevation, velocities, pressure, etc., into the appropriate governing equations and boundary conditions describing the wave motion yields a series of higher-order solutions for ocean waves. Equating the coefficients of equal powers of kA gives recurrence relations for each order solution.

A characteristic of the perturbation expansion is that each order theory is expressed in terms of the preceding lower order theories. The first-order Stokes theory corresponds to the linear theory. Note that linear, i.e. the first-order, theory applies to a wave that is symmetrical about the still-water level (SWL) and has water particles that move in closed orbits. Stokes' higher-order theories predict a wave form that is asymmetrical about the SWL but still symmetrical about a vertical line through the crest and has water particle orbits that are open. They have higher more peaked crests and shorter, flatter troughs. The cnoidal wave crests are higher above the SWL than the troughs are below the SWL. Cnoidal troughs are longer and flatter and crests are sharper and steeper than Stokes waves. The solitary wave, a form of the cnoidal wave, has all of its profile above the SWL. Wave profiles obtained from different wave theories are sketched in Fig. 3.2 for comparison.

The following dimensionless parameters result to be very useful to describe linear waves as well as finite-amplitude waves:

- the wave slope, ϵ , is a measure of how large a wave is relative to its height and whether the linear wave assumption is valid; large values of the wave steepness suggest that the small-amplitude assumption may be questionable;
- the relative water depth, h/L , determines whether waves are dispersive or non dispersive and whether the celerity, length, and height are influenced by water depth;
- the relative wave height, $\frac{H}{h}$, may be used to replace either the wave steepness or relative water depth; large values of the relative wave height indicate that the small-amplitude assumption may not be valid;

the Ursell number, $U = \frac{HL^2}{h^3} = \frac{H}{h} \left(\frac{L}{h}\right)^2$, is often used to assess the relevance of various wave theories; for a given relative wave height H/h the Ursell parameter, and thus the nonlinearity, grows quickly with increasing relative wavelength L/h ; high values of U indicate large, finite-amplitude, long waves in shallow water that may necessitate the use of nonlinear wave theory.

Stokes's finite amplitude wave theory is applicable when $U < 79$. This condition restricts the wave heights in shallow water and the Stokes theory is not generally applicable to shallow water.

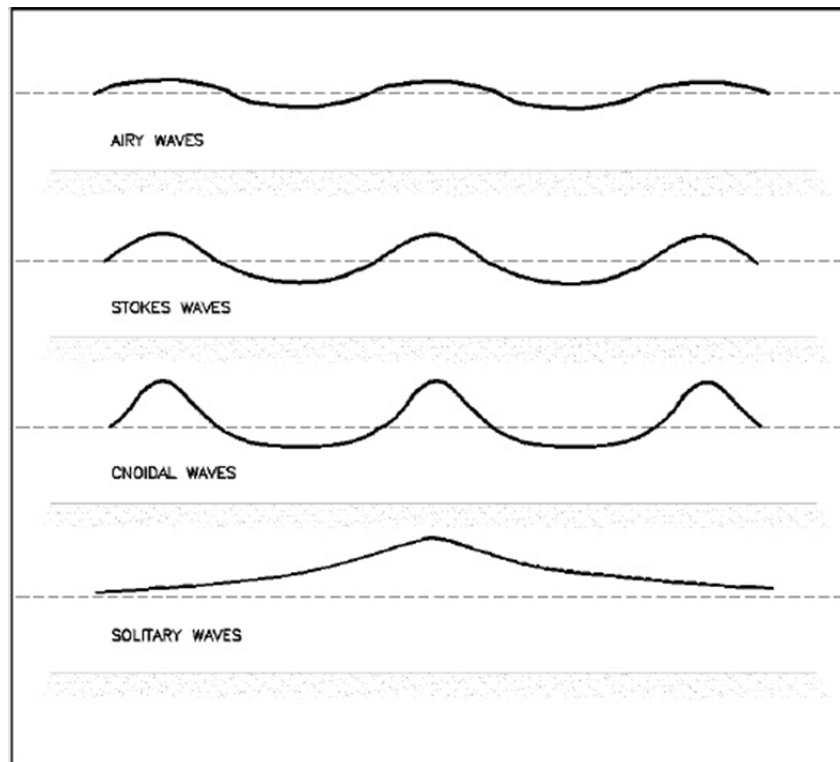


Fig. 3.2 Wave profile shape of different progressive gravity waves [48].

In [62] is showed a solution found by Stokes for so-called finite amplitude waves in deep water where the phase speed (to third order) is governed by k and the wave amplitude A

$$c = \sqrt{\frac{g}{k} (1 + k^2 A^2)} \quad (3.24)$$

In the higher-order Stokes solutions, superharmonic components (i.e., higher frequency components at two, three, four, etc. times the fundamental frequency) arise. These are superimposed on the fundamental component predicted by linear theory. Hence, wave crests are steeper and troughs are flatter than the sinusoidal profile (Fig. 3.2). The fifth-order Stokes

expansion, widely used in practical applications, shows a secondary crest in the wave trough for high-amplitude waves.

At high orders, wave velocity and wavelength depend on wave height, and therefore, for a given wave period, celerity and length are greater for higher waves. Some limitations are imposed on the finite-amplitude Stokes theory in shallow water both by the water depth and amplitude nonlinearities. For steeper waves in shallow water, higher-order terms in Stokes expansion may increase in magnitude to become comparable or larger than the fundamental frequency component. When this occurs, the Stokes perturbation becomes invalid.

Higher-order Stokes theories include aperiodic terms in the expressions for water particle displacements. These terms arise from the product of time and a constant depending on the wave period and depth, and give rise to a continuously increasing net particle displacement in the direction of wave propagation; therefore, particle paths for Stokes waves are no longer closed orbits and there is a drift or mass transport in the direction of wave propagation. The distance a particle is displaced during one wave period when divided by the wave period gives a mean drift velocity $U(z)$, called the mass transport velocity. To second-order, the mass transport velocity is [48]

$$U(z) = \left(\frac{\pi H}{L}\right)^2 \frac{c}{2} \frac{\cosh[4\pi(z+h)/L]}{\sinh^2(2\pi h/L)} \quad (3.25)$$

indicating that there is a net transport of fluid by waves in the direction of wave propagation. If the mass transport leads to an accumulation of mass in any region, the free surface must rise, thus generating a pressure gradient. A current, formed in response to this pressure gradient, will reestablish the distribution of mass. Following Stokes, using higher-order wave theories, both theoretical and experimental studies of mass transport have been conducted. Results of two-dimensional wave tank experiments where a return flow existed show that the vertical distribution of the mass transport velocity is modified so that the net transport of water across a vertical plane is zero.

Very high-order Stokes theories provide a reference against which the accuracy of the other theories may be tested. Wave amplitude and period may sometimes be estimated from empirical data. When data are lacking or inadequate, uncertainty in wave height and period estimates can give rise to a greater uncertainty than does neglecting the effect of nonlinear processes. Therefore, the additional effort necessary for using nonlinear theories may not be justified when large uncertainties exist in the used wave data. Nonetheless, nonlinear wave theories usually provide safer and more accurate estimates.

As waves move into shoaling water, the wave amplitude becomes progressively higher, the crests become shorter and sharper and the trough becomes longer and flatter. When $U > 79$, i.e. for longer waves, a different perturbation parameter should be used to account for the combined influence of amplitude and frequency dispersion. This can be achieved by constructing two perturbation parameters whose ratio is equivalent to the Ursell parameters. The set of equations obtained in this manner are referred to as the nonlinear shallow-water wave equations. Some common wave theories based on these equations are the Korteweg and de Vries and Boussinesq wave theories [48]. They can be derived by assuming the pressure to be hydrostatic so that vertical water particle accelerations are small and imposing a horizontal velocity on the flow to make it steady with respect to the moving reference frame.

The shoaling assumption

The notion of wave shoaling or wave transformation on a beach was introduced on an intuitive basis by Rayleigh in 1911. In his approach there are the following three more or less independent assumptions involved:

1. to the first approximation in bottom slope, the wave will continuously adjust its form so that surface profile, phase and particle velocities, pressure variation, etc. can be determined from the horizontal bottom theory, applying the local values of water depth and wave height;
2. the wave energy flux through a vertical section is constant, which implies that the reflection is negligible;
3. the number of waves remain constant during the shoaling process so that the wave period T is conserved.

Each of these assumptions requires a sufficiently gently varying water depth, but how gently will actually depend on the wave theory considered. This question can be analysed theoretically by rigorous perturbation expansions including the effect of the bottom slope h_x .

Rayleigh, of course, presented the ideas in terms of the linear wave theory, and for that case it may be shown that the shoaling assumption is satisfied if $S \equiv h_x L / h \leq O(H/L)$.

For higher order Stokes waves only smaller values of h_x are allowed, depending on the order considered. For first order cnoidal waves, in [48] it is showed that a consistent shoaling theory requires $S = O(h/L)^3$.

In conclusion we notice that in all the cases the parameter S occurs and that shoaling conditions imply that S is too small to be significant.

Cnoidal wave theory

The cnoidal theory is applicable to long, finite-amplitude waves of permanent form propagating in shallow-water and which are weakly dispersive and weakly non-linear (two classical Boussinesq assumptions). Cnoidal theory is based on the Boussinesq theory, but is restricted to waves progressing in only one direction. The theory is defined in terms of the Jacobian elliptic function. Cnoidal waves are periodic with sharp crests separated by wide flat troughs (Fig. 3.2).

The approximate range of validity of the cnoidal theory is $h/L < 1/8$ when the Ursell number $U > 20$.

As wavelength becomes long and approaches infinity, cnoidal wave theory reduces to the solitary wave theory (the most elementary solution of the Boussinesq equation is the solitary wave; a solitary wave is a wave consisting of a single crest and a surface profile lying entirely above the SWL). Also, as the ratio of wave height to water depth becomes small (infinitesimal wave height), the wave profile approaches the sinusoidal profile predicted by the linear theory.

Because local particle velocities, local particle accelerations, wave energy, and wave power for cnoidal waves are difficult to describe such descriptions are not included here.

The analytical solution for cnoidal wave theory was simplified in references [60], [63] to

$$\omega = k\sqrt{gh(1 + f(m)H/h)} + \vec{k} \cdot \vec{u}_c \quad (3.26)$$

$$f(m) = \frac{2}{m} - 1 - \frac{3E}{mK} \quad (3.27)$$

where E and K are the Jacobian elliptic integrals (E is the complete elliptic integral of the second kind). The expected single value for $f(m)$ is approximately 0.4. Specifically, in [62] the $f(m)$ term is calibrated to a single value, varying for coastal zones between 0.42 and 0.48.

It is proven, in the same works, that the accuracy of eq. 3.26 is significant with respect to that of the linear theory. More in detail, cnoidal theory predicts the phase velocity to be within a few per cent while small amplitude approximations will result in an underestimate of wave celerity and an overestimate of the actual depth when using the linear theory. The only exception is close to breaking, where the cnoidal theory overestimates the finite amplitude effect and yields results somewhat above the measurements.

Hedges' dispersion relation

Alternatively to the cnoidal theory, several authors have proposed simple modifications to the linear dispersion relation which are designed to mimic the effect of amplitude dispersion in shallow water. Hedges has proposed a modified dispersion relation given by [64]

$$\omega^2 = gk \tanh[k(h + A)] \quad (3.28)$$

In shallow water and for A/h small, the formula leads to the following dispersion relation

$$\omega^2 = gk^2(h + A) \quad (3.29)$$

$$c = \sqrt{[g(h + A)]} \quad (3.30)$$

This phase speed represents the speed of propagation of a solitary wave of height $H = 2A$. The shallow limit of the approximate form is thus physically reasonable. In the deep-water limit, eq. 3.28 approaches the linear dispersion relation, as the ratio A/h approaches zero due to increasing water depth.

Wave breaking

A progressive gravity wave is physically limited in height by depth and wavelength. For a given water depth and wave period, there is a maximum height limit above which the wave becomes unstable and breaks. This upper limit of wave height, called breaking wave height, is in deep water a function of the wavelength and, in shallow and transitional water, is a function of both depth and wavelength. Stokes predicted theoretically that a wave would remain stable only if the water particle velocity at the crest was less than the wave celerity or phase velocity. If the wave height were to become so large that the water particle velocity at the crest exceeded the wave celerity, the wave would become unstable and break. Stokes found that a wave having a crest angle less than 120° (angle between two lines tangent the surface profile at the wave crest) would break. In [48] is shown that in deep water the theoretical limit for wave steepness is

$$c = \sqrt{[g(h + A)]} \quad (3.31)$$

$$\left(\frac{H_0}{L_0}\right)_{max} = 0.142 = \frac{1}{7} \quad (3.32)$$

and that the limiting steepness for waves traveling in depths less than $L_0/2$ without a change in form is

$$\left(\frac{H}{L}\right)_{max} = \left(\frac{H_0}{L_0}\right)_{max} \tanh\left(\frac{2\pi h}{L}\right) = 0.142 \tanh\left(\frac{2\pi h}{L}\right) \quad (3.33)$$

3.1.3 Composite models

Composite models have been introduced as an attempt to smoothly match an approximate, shallow-water dispersion relation to an analytically obtained relation for intermediate and deep water. The inadequacy of an approximate shallow-water dispersion relation to model nonlinear effects in intermediate water depth, coupled with the invalidity of the Stokes model in shallow water, leads to the need for a matched dispersion relation which predicts the phase speeds of waves smoothly from deep to shallow water.

Kirby and Dalrymple in [64] propose the following dispersion relation to model nonlinear effects over a broad range of depths

$$\omega^2 = gk(1 + f_1(kh)\epsilon^2 D) \tanh(kh + f_2(kh)\epsilon) \quad (3.34)$$

Where

$$D = \frac{\cosh(4kh) + 8 - 2 \tanh^2(kh)}{8 \sinh^4(kh)} \quad (3.35)$$

In order to satisfy the Stokes wave limit, the following relations must be satisfied

$$f_1(kh) \rightarrow 1 \text{ as } kh \rightarrow \infty$$

$$f_2(kh) \rightarrow 0 \text{ as } kh \rightarrow \infty$$

$$f_1(kh) \rightarrow 1 \text{ as } kh \rightarrow 0$$

In addition $f_1(kh)$ must be $O(kh^5)$ or smaller in order to overcome the singularity in D , which is $O(kh^{-4})$. Based on these requirements, they have chosen f_1 and f_2 according to

$$f_1(kh) = \tanh^5(kh) \quad (3.36)$$

$$f_2(kh) = [kh/\sinh(kh)]^4 \quad (3.37)$$

In order to compare the proposed composite dispersion relation to the previous results, in Fig. 3.3 is reported the quantity ω^2/gk versus values of kh . Separate sets of curves are given for choices of the wave steepness ϵ . The dependent variable may be also reinterpreted as

$$\frac{\omega^2}{gk} = \left(\frac{\omega}{k}\right) / \left(\frac{g}{\omega}\right) = \frac{c}{c_0} \quad (3.38)$$

where c is the local phase speed, dependent on kh and ϵ , and c_0 is the linear, deep-water phase speed.

An inspection of each set of curves shows that the composite form matches smoothly to both the Stokes form in deeper water and the Hedges form in shallow water. The strong singularity in the Stokes form is also apparent. The curve corresponding to the composite form typically lies between the Stokes curve and the Hedges curve, which may or may not intersect each other. Vertical bars are also shown which indicate a hypothetical breaking limit based on $A/h = 0.4$. The benefits of the empirical modification are clear; allowance is made for the specification of a model which remains valid in shallow water and at the same time is essentially analytically based for $kh > 2$.

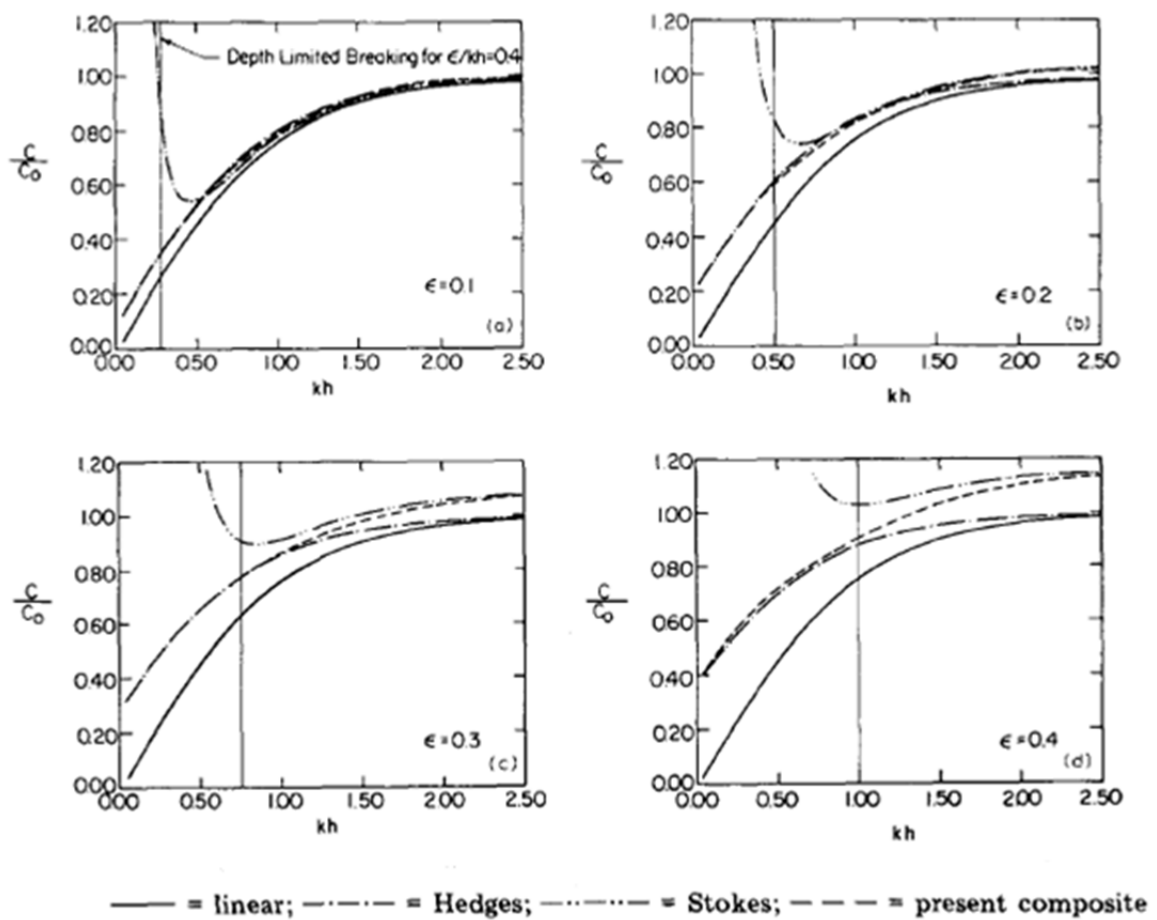


Fig. 3.3 Variation of linear and nonlinear dispersion relation with kh and wave steepness $\epsilon = kA$ [64]; (a) $\epsilon = 0.1$, (b) $\epsilon = 0.2$, (c) $\epsilon = 0.3$, (d) $\epsilon = 0.4$.

3.1.4 Validity of wave theories

In order to ensure proper use of the several existing wave theories, their range of validity must be established. Fig. 3.4 [48] describes the approximate limits of validity for several wave

theories, including the third- and fourth-order Stokes' theories. The fourth-order Stokes' theory may be replaced with the more popular fifth-order theory, since the latter is often used in applications. Cnoidal theory is recommended for shallow-water waves of low steepness, while Stokes' higher order theories are preferred for steep waves in deep water. Linear theory is recommended for small steepness and small U values. For low steepness waves in transitional and deep water, linear theory is adequate but other wave theories may also be used. Fig. 3.4 can represent a guide to select an appropriate wave theory for given values of H , h , and T . It is necessary to know the limiting value of wave heights and wave steepness at different water depths to establish range of validity of any wave theory that uses a Stokes-type expansion. This is customarily done by comparing the magnitude of each successive term in the expansion; each should be smaller than the term preceding it. The magnitude of the Ursell number U may be used to establish the boundaries of regions where a particular wave theory should be used.

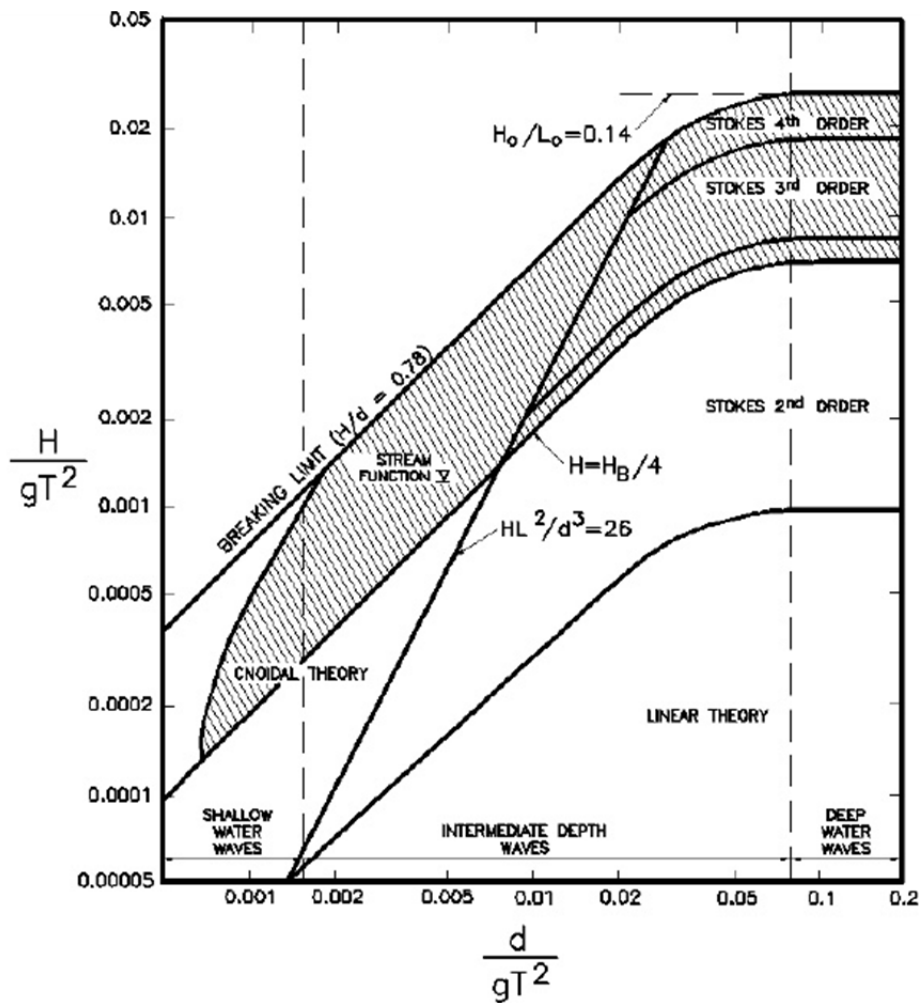


Fig. 3.4 Ranges of validity of various wave theories [48] (d represents the water depth in the figure).

3.1.5 Synthesis and discussion

A bathymetric technique based on sea surface long-period waves called swells has been presented. Swell waves are waves which have travelled far from their region of origin tending to be uniform in height, period and direction of propagation and to have long individual crests. Different models aimed at describing the relations between swell wave parameters and water depth have been shown in the previous subsections. Depth estimation from SAR depends on sea state and needs the presence of such kind of waves in the image acquired. To retrieve bathymetry from waves we need wave parameters being dependent on water depth, i.e. waves must “feel” the bottom. This is true only for water depth less than half the wavelength of the sea wave, that is for intermediate and shallow water. For deeper water, waves are not influenced by sea bottom topography and therefore it is impossible to use this method to retrieve bathymetry. Obviously the wave wavelength depends on the analyzed site and, therefore, we cannot identify an univocal value for the intermediate water limit. However, an approximate value range of 70-100 m water depth can be adopted as intermediate water limit depending on sea state and acquisition quality and representing the maximum depth affecting wave motion.

For intermediate depth it has been shown that there is no doubt about the ability of the linear dispersion relation to well model the wave behavior depending on the sea bottom topography. It is the first-order, small amplitude wave theory linking water depth to sea waves wavelength and period and it emerges as solution of the general equations of motion under the assumption that the wave height is much smaller than the wave wavelength. With a single SAR image it is possible to track a wave from open sea to shoreline and to measure changes of wavelength and direction. Unfortunately, it is not possible to measure its period directly. The information about wave period can be derived by external sources or from a first indication of the offshore water depth. Linear dispersion relation cannot work for bottoms featuring sharp changing of depth.

For very shallow water, a few meters depth, the ratio of the depth over the wavelength becomes relative small and wave crests become higher. In such a situation, Hedges' dispersion relation could be considered to describe the effect of amplitude dispersion. However this dispersion relation also needs the wave amplitude as an input parameter and wave amplitude cannot be directly calculated from SAR images. In addition, when amplitude and period are estimated from empirical data, uncertainty in wave height and period estimates can give rise to a greater uncertainty than that achieved neglecting the effect of nonlinear processes. In conclusion, the additional effort necessary for using nonlinear theories may not be justified when large uncertainties exist. In accordance with the this consideration, the linear dispersion relation has been applied to TerraSAR-X spotlight SAR data demonstrating to capability to derive good bathymetric measurements until the shoreline [32], [39].

From the observations made, it is reasonable to select the linear dispersion relation as the most suitable model to derive bathymetry from SAR images; in this way, only one external parameter is needed, i.e. the wave period or equivalently a first indication of the offshore water depth (see Section 5.1). Instead, values of swell wavelength and direction of propagation can be directly retrieved from SAR data. In this way, sea water depth can be estimated throughout the SAR image by application of the linear dispersion relation (eq. 3.10).

3.2 Current-based bathymetric technique

In 1969 de Loor identified some bathymetric features on the Ka-band (36 GHz) aerial images of the North Sea [65], [66]. However, the origin of the current-based bathymetric method goes back to 1978 when the first radar images acquired by the American SEASAT SAR satellite became available [35], [67], [68]. Specifically, SEASAT SAR images of the English channel (see Fig. 3.5) were extensively studied to interpret and explain the relevant imaging mechanism.

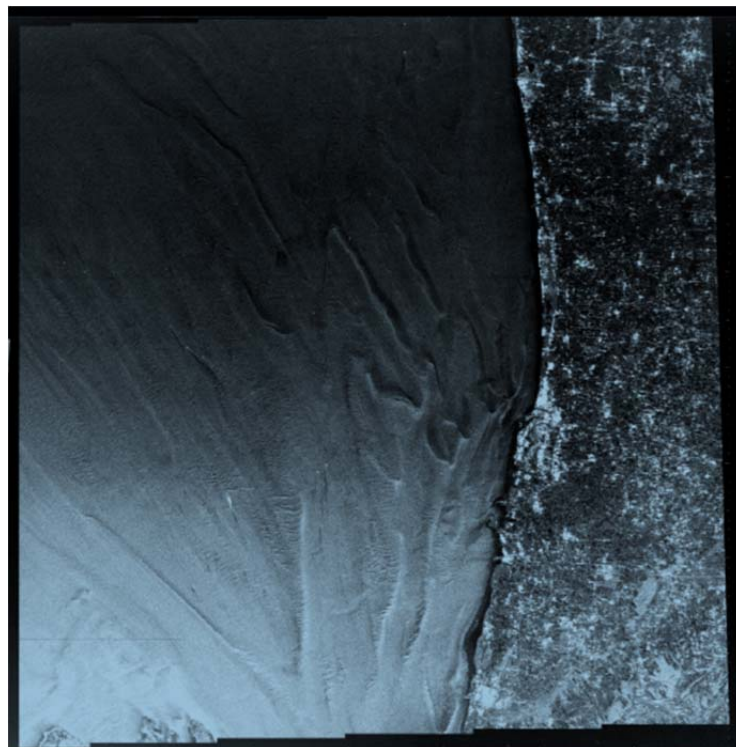


Fig. 3.5 SEASAT SAR image (L-band, HH polarization) of the English channel [35]. The French/Belgian coast is visible on the right hand side. The V-shape feature in the lower left-hand section of the image is a pair of two underwater ridges called South Falls (the thin line to the left) and Sandiette (the broader line to the right).

An imaging model able to explain the basic features observed in radar imagery of underwater bottom topography was first proposed by Alpers and Hennings [37]. It derived from a series of empirical evidences arising from the analysis of a wide series of radar images and stated that underwater topographic features like sandbanks or shoals become visible on radar images of sea surface under moderate wind speed (3-12 m/s) and strong tidal currents (≥ 0.5 m/s) [35], [43]. They formulated an imaging mechanism based on the following three steps (see Fig. 3.6) [35], [37]:

- 1) Current field variations are generated by the interaction between the current flow and the seabed, and they produce gradients in the surface current velocity.
- 2) Surface current velocity gradients modify the spectrum of the short, wind-generated, surface waves.
- 3) Intensity modulations in radar imagery result from modulations in the surface roughness consequent to (2).

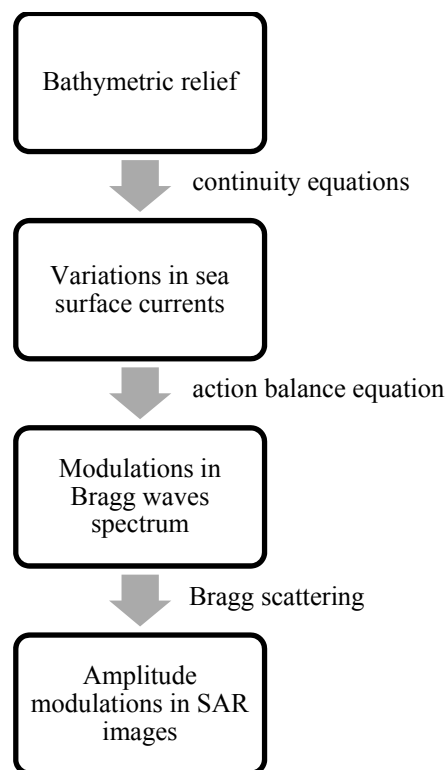


Fig. 3.6 Illustration of the key steps in radar imaging of bathymetric features [69]. For each step the main modeling approach proposed in [37] is also reported.

3.2.1 Alpers and Hennings model

The first example of complete quantitative bathymetric modeling of bathymetric imaging by SAR was developed by Alpers and Hennings in 1984 [37], providing a theoretical framework for each step of the imaging mechanism (Fig. 3.6). Actually, their research was not aimed at the development of a theoretical model quantitatively explaining all the aspects of bathymetric imaging. Their purpose was to present a simple model able to explain the basic features of underwater bathymetry observed in radar imagery. However, despite some oversimplifications, the model became the basis for the development of the first SAR based product [50] for bathymetric reconstruction.

Current-bottom topography interaction

The first step concerns the effect that a three-dimensional bathymetry has on a three-dimensional time-variable current. The shallow water hydrodynamic equations [70] and the conservation of mass (or continuity) equation must be considered in this case. With specific reference to SAR operations in coastal areas [35], weak time dependence and incompressible laminar flow can be assumed. In addition, vertical shear currents can be typically neglected.

Alpers and Hennings assumed the following equations for the current velocity component normal to the direction of the underwater ridge or bank, u_{\perp} , and the parallel one, u_{\parallel} ,

$$\begin{aligned} u_{\perp}(x_{\perp})d(x_{\perp}) &= c_{\perp} \\ u_{\parallel} &= c_{\parallel} \end{aligned} \quad (3.39)$$

where $d(x_{\perp})$ indicates a depth profile along a line perpendicular to the ridge, x_{\perp} , x_{\parallel} represent the axis perpendicular and parallel to the ridge, respectively (see Fig. 3.7), and c_{\perp} , c_{\parallel} are constant values. Equation 3.39 implies that surface current vector $\mathbf{u} = (u_{\perp}, u_{\parallel})$ changes direction when crossing a sand bank at oblique angles.

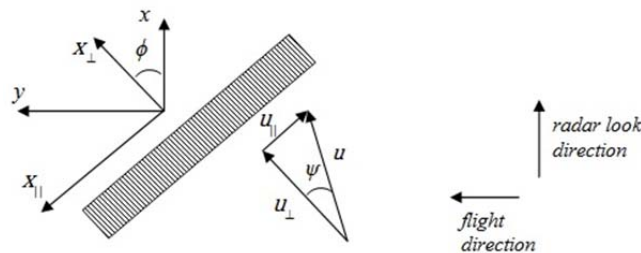


Fig. 3.7 Geometry and symbols of Alpers and Hennings Model [37].

Wave-current interaction

The second step of the imaging model deals with the interaction between surface current and surface short waves. Based on the hydrodynamic interaction theory [71], the response of the spectrum of the sea surface waves to the perturbation generated by a variable surface current is described by the Action Balance Equation (ABE). Specifically, ABE is a partial-derivative differential equation giving a relationship among surface velocity, its gradient and the action spectrum density of short surface waves.

The action spectral density n is defined as E/ω_0 where E is the energy density distributing the wave energy over the angular frequencies ω_0 in a stationary reference frame. The energy density varies, in general, over sea surface depending on surface space coordinates $\mathbf{p} = (x, y)$, wavenumber $\mathbf{k} = (k_x, k_y)$, and time t . The ABE states that the Lagrangian derivative of the action spectral density is given by the so called source function s , which models all the phenomena affecting the wave spectrum, e.g. wind or dissipation processes

$$\frac{\partial n(\mathbf{p}, \mathbf{k}, t)}{\partial t} + \mathbf{p}' \cdot \frac{\partial n(\mathbf{p}, \mathbf{k}, t)}{\partial \mathbf{p}} + \mathbf{k}' \cdot \frac{\partial n(\mathbf{p}, \mathbf{k}, t)}{\partial \mathbf{k}} = s(\mathbf{p}, \mathbf{k}, t) \quad (3.40)$$

where the symbol “ \cdot ” indicates the dot product and the apex “ $'$ ” represents the time derivative [7]. If no variable currents were present the spectrum of short surface waves would be in equilibrium according to the Phillips’s law

$$n_0(\mathbf{k}) = a_p \frac{|\mathbf{k}|^{-4}}{\omega_0(\mathbf{k})} \quad (3.41)$$

where a_p is a constant and $||$ is the Euclidean vector norm. For the present problem the wave frequency ω in a moving medium must be considered [37], which is affected by the current velocity $\mathbf{u}(\mathbf{p}, t)$

$$\omega(\mathbf{p}, \mathbf{k}, t) = \omega_0(\mathbf{k}) + \mathbf{k} \cdot \mathbf{u}(\mathbf{p}, t) \quad (3.42)$$

and regulates the behavior of the time derivatives \mathbf{p}' and \mathbf{k}' as follows

$$\mathbf{p}' = \frac{\partial \omega(\mathbf{p}, \mathbf{k}, t)}{\partial \mathbf{k}} \quad \mathbf{k}' = \frac{\partial \omega(\mathbf{p}, \mathbf{k}, t)}{\partial \mathbf{p}} \quad (3.43)$$

Different models can be used to represent the source function [72]. The most common ones are linear or quadratic in the action spectrum. In both cases, a parameter is introduced called relaxation rate. With specific reference to the linear model, the source function is

$$s(\mathbf{p}, \mathbf{k}, t) = -\mu(\mathbf{k})[n(\mathbf{p}, \mathbf{k}, t) - n_0(\mathbf{k})] \quad (3.44)$$

where μ is the relaxation rate and represents a measure of the response time of the wave spectrum to current variations depending on the combined effects of winds, non linear energy transfers and non linear dissipation. The inverse of the relaxation rate is the relaxation time that therefore represents the time in which the disturbed action spectrum of short water waves returns back to its equilibrium state. According to Alpers and Hennings approach the relaxation rate is interpreted as a free parameter

Substituting eqs. 3.42-3.44 and neglecting second order terms, eq. 3.40 yields

$$\frac{\partial n(\mathbf{p}, \mathbf{k}, t)}{\partial t} + [\mathbf{c}_g(\mathbf{k}) + \mathbf{u}(\mathbf{p}, t)] \cdot \frac{\partial n(\mathbf{p}, \mathbf{k}, t)}{\partial \mathbf{p}} - \mathbf{k} \cdot \frac{\partial \mathbf{u}(\mathbf{p}, t)}{\partial \mathbf{p}} \cdot \frac{\partial n(\mathbf{p}, \mathbf{k}, t)}{\partial \mathbf{k}} = -\mu(\mathbf{k})[n(\mathbf{p}, \mathbf{k}, t) - n_0(\mathbf{k})] \quad (3.45)$$

where $\mathbf{c}_g(\mathbf{k}) = \partial \omega_0 / \partial \mathbf{k}$ is the group velocity of short waves [7]. In addition, under the majority of cases, the time derivative of the action spectrum can be neglected [37], [50],[72],[73].

Radar-wave interaction

The last step of the bathymetric SAR model considers SAR response as a function of the sea surface spectrum modulation which is determined by the current variations due to bathymetry. As noted above, for radar wavelength in the microwave region, Bragg scattering is the most significant scattering effect from sea surface. According to Bragg's model [40], the backscattered power is proportional to the spectral energy density of those waves traveling along the ground range direction of the SAR sensor, and characterized by a specific wave number depending on radar wavelength and incidence angle. With reference to SAR image intensity i the model states that

$$\frac{\Delta i(\mathbf{p}, \mathbf{k}_B)}{i_0} = \frac{\Delta n(\mathbf{p}, \mathbf{k}_B)}{n_0} \quad (3.46)$$

where the subscript 0 is used for the equilibrium condition (i.e., i_0 is the reference image intensity corresponding an equilibrium region of sea surface where the current velocity is constant and not affected by bottom topography), \mathbf{k}_B is the Bragg's wavenumber vector and Δ indicates the variation with respect to the equilibrium value [7]. Bragg's model performs well at L- and P- bands, higher-order composite scattering models [74] should be used at higher

frequencies, i.e. for C- and X-band. In addition, when the ground range component of the surface current velocity varies along the azimuth direction, the velocity bunching gives rise to a signal intensity modulation in the azimuth direction [41]. Such a modulation is typically lower but in general not negligible [37] with respect to that due to Bragg scattering.

The analytical model developed by Alpers and Hennings is able to explain why bathymetric features can be observed in SAR images, however it often represents an extremely strong simplification if SAR images have to be used for cartographic purpose, that is to derive bottom bathymetry.

The first important work discussing the potential use of RAR and SAR images for bathymetric data retrieval is the one presented by Vogelzang [72]. It highlights the main properties of the analytical model proposed by Alpers and Hennings, and proposes solutions to improve its applicability through numerical approaches. The work recognizes the ABE as the critical step in bathymetric reconstruction since the effects of surface current velocity on the surface short wave spectrum is the less assessed modeling step. Even when the temporal dimension is not taken into account, the action spectrum is a function of two vector parameters (\mathbf{p} , \mathbf{k}) or equivalently four scalar parameters (x , y , k_x , k_y). Vogelzang analyzed the behavior of different ABE formulations, but limited to one-dimensional and stationary assumptions. ABE can be solved analytically as done by Alpers and Hennings only if advection is neglected with respect to relaxation and high-order effects in the action spectrum and current velocity are neglected. If this is not the case, only numerical solutions can be derived. Two different numerical solutions of the ABE were derived by Vogelzang considering two different source functions:

- a) Alpers and Henning linear source function (see eq. 3.44), with relaxation rate as a constant parameter.
- b) The source function proposed by Shuchman et al. [75] that is quadratic in the action spectrum. In this case also the relaxation rate is modeled as a function of wavenumber and wind speed variations.

Considering an assigned sinusoidal current variation, Vogelzang solved numerically the ABE by the method of characteristic and evaluated the variation of radar Bragg backscattering as resulting from varying the remaining parameters such as wind speed, current velocity, relaxation rate, radar wavelength. The analyzed parameters were:

- a) Radar backscatter modulation or modulation depth, that is the magnitude (in percentage) of the modulation in radar image intensity induced by a variable current velocity. From former experimental results reported in the literature the expected modulation was in the order of 10 per cent (0.1) for both L-band and X-band.

b) Phase shift, i.e. the phase angle between the peak of the current velocity (corresponding to the peak of bottom topography) and the peak of radar backscattering.

For example, considering the analytical model of Alpers and Hennings, the phase angle is always 90° (see Fig. 3.8) and it is not affected by the radar wavelength, whereas the modulation depth is 10% in L-band and only 1% in X-band (where the latter value does not correspond to experimental results).

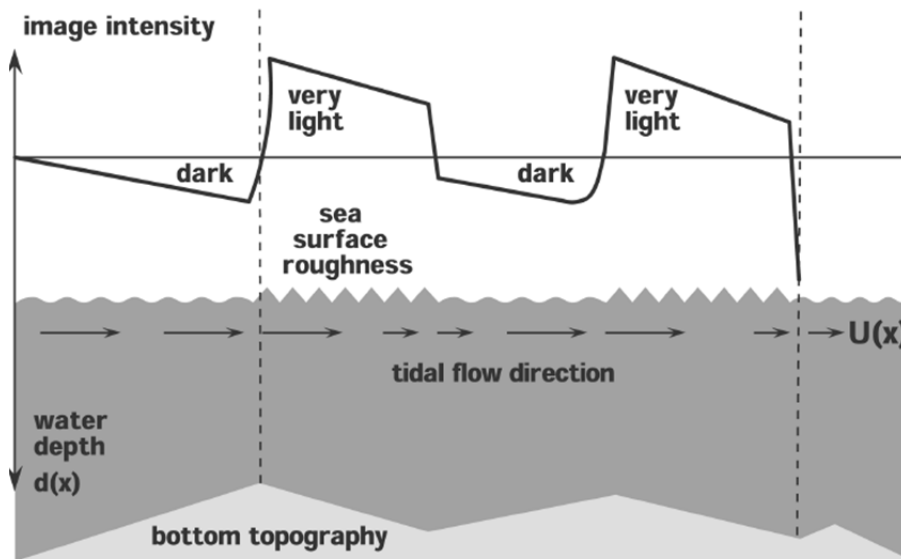


Fig. 3.8 Geometry of Alpers and Hennings Model [35]. Surface current gradient generated by the bottom topography produces a modulation of sea surface spectrum increasing Bragg-waves energy (i.e. surface roughness) in correspondance of strong current gradient. Sea surface zones featuring increasing roughness appear brighter in SAR images.

The main results of Volgezang's work have been:

- 1) Advection is important for both the magnitude of the modulation in the radar backscatter and the position of this modulation relative to the bottom topography, notably at L-band for features smaller than 1 km such as sand waves. This means that, to the purpose of retrieving bathymetric data, ABE cannot be solved analytically but numerical methods must be used.
- 2) The terms of second-order in the action spectrum and current velocity, neglected by Alpers and Hennings, have only a small effect on the phase shift and the modulation depth.
- 3) When advection is included in the model of Alpers and Hennings, the achieved results are close to those of Shuchman et al., which means that the effect of quadratic terms in the source

function and the effects of wave number and wind speed variations due to current velocity variations in the relaxation rate are small.

4) The implemented methods foresee that the modulation at X-band is one order of magnitude smaller than at L-band. This result is in disagreement with experiments which show the same order magnitudes for both bands. In this context, Vogelzang underlined that radar backscattering modeling in X-band should be improved by inclusion of additional scattering mechanism with respect to the first order Bragg model.

3.2.2 Bathymetric Assessment System - BAS

On the basis of all the above reported results, the first (and also, till now, the only) commercial system for bathymetric data retrieval (and raster DEM generation too) has been developed by ARGOSS, a Dutch company. The system is named Bathymetry Assessment System (BAS) [50].

The BAS consists of two main parts: an imaging model suite to compute a simulated SAR image from a given depth map and some tidal information, and a data assimilation inversion scheme. The schematic structure of the BAS is shown in Fig. 3.9.

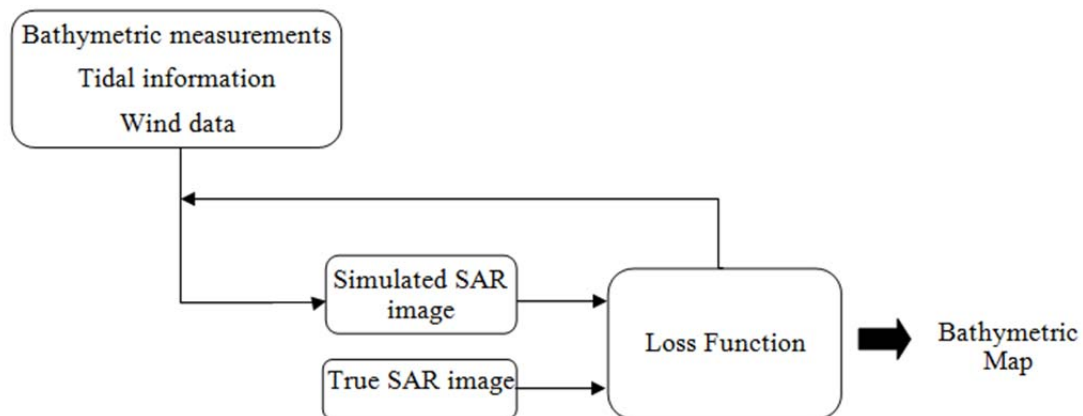


Fig. 3.9 BAS scheme [50], [69].

To produce a depth map, the BAS needs one or more SAR images and a limited number of conventional depth measurements [50]. Although depth variations can be detected with SAR, echo soundings are needed because the absolute water level or very smooth slopes cannot be determined. Indeed, the BAS uses SAR imagery to interpolate between ship's soundings in a smart way. The BAS does not eliminate the need for conventional depth measurements, but can help to reduce the sounding effort required for a reliable depth map. Conventional depth

measurements are also used to calibrate the imaging model and to generate a first-guess depth map to start the data assimilation inversion.

As shown in Fig. 3.9, a simulated radar image is calculated from the first-guess depth map using the imaging model. Therefore, it implements the so-called forward-model based on the described three-step mechanism. The simulated radar image is compared with the true radar image by evaluating a penalty function. The penalty function also contains a term giving the deviation between model depth and echo soundings, where available, and a term containing a smoothness criterion. The first-guess depth map is adjusted by minimizing the penalty function. This iterative procedure leads to a resulting model depth map which is the best estimate for the real depth [50].

It is worth to note that intensity modulations in SAR images are not only caused by bottom topography, but also by other features such as slicks, fronts, ship wakes and internal waves. Such no-bottom features should be recognized by image visual inspection and removed, otherwise BAS interprets them as depth variations.

The described method has been applied to various sites along the coast of the Netherlands in order to validate its performance and to determine the accuracy that can be reached with the system. For example, the relevant results to sites located in the Waddenzee [50], a shallow sea in the North of the Netherlands, are reported herein. Traditional soundings, with cm-scale noise level, were available for each site, leading to a measured depth value every 3 m along the transects, with a distance of 200 m between the tracks. Some of the tracks were used for calibration during map generation (these are later referred to as calibration tracks), while others were reserved for use in a statistical accuracy analysis.

The BAS typically produces depth maps on a grid of size 25 m. It is worth noting that BAS does not return the exact values of the soundings, since it has some freedom to deviate from them (smoothness criterion). The allowed difference between the BAS estimates and the soundings depends on the accuracy of the soundings themselves, the variability of the bottom topography within a grid cell, and the success of the imaging model in reproducing the radar image.

The first example of performance deals with the Plaatgat area [50], a tidal inlet between the Dutch isles Ameland and Schiermonnikoog. One ERS-1 SAR VV-polarized image has been used as input for BAS. The bottom topography of the Plaatgat site exhibits two-dimensional features and is too complex to be mapped as a whole with the one-dimensional BAS. To circumvent this problem, the Plaatgat site was divided into three sub-areas which can be treated, to a good approximation, as one-dimensional. Adopted performance metrics were:

- 1) bias (the average depth difference);

- 2) rms error (the root of the mean squared depth difference);
- 3) absolute error (the average of the absolute value of the depth difference);
- 4) exceedence level (95% of the depth differences are below this value).

In general, for different selections of validation tracks, the bias error is negligible being of the order of 2 cm. All the other metrics, instead, are affected by the distance between the calibration tracks. For 600 m distance both the rms and the absolute error are about 20 cm, with the exceedence level lower than 50 cm.

The second example of performance given in [50] deals with Groote Plaat, a tidal flat to the south west of the isle of Terschelling. Four C-band VV-polarized images collected by ERS-1 and ERS-2, from June to July 1996 were used as input for BAS. The achieved performance has shown negligible bias, rms and absolute errors lower than 10 cm and exceedence level lower than 15 cm for 400 m distance between calibration transects.

Finally, a single high resolution 3m x 3m C-band VV-polarized SAR image of Groote Plaat has been also used [50], collected by PHARUS, a Dutch airborne SAR. The higher resolution of the airborne image allowed a final BAS map resolution of 5 m x 5m. In the same condition as in the previous case, that is with 400 m distance between calibration transects, rms and absolute errors lower than 5 cm, and exceedence level of about 7.5 cm were achieved. These results indicate that, for high resolution systems the distance between the calibration tracks may be also extended above 1 km , if 20 cm rms error is considered satisfactory.

A major limitation of the first version of BAS is that the inversion scheme is one-dimensional. This means that BAS can be applied in areas with a simple bottom topography, so that the surface current is dominated either by mass conservation or by bottom friction. A more complicated area has to be split up into sub-areas where one of the models may be applied. This leads to much hand work and requires intervention by specialists also limiting the operational application of the system.

More recently, ARGOS extended BAS with two-dimensional models of tidal flow, wave-current interaction and backscatter, and a comprehensive inverse modelling technique to estimate the bathymetry [76]. However few details are available about these extensions as well as the potential performance improvements.

Most of BAS results deal with C-band SAR, which is not an optimum choice for observing bottom signatures (and phenomena caused by wave-current interaction in general) [50]. Stronger signatures are found when using lower radar frequencies: L-band or, preferably, P-band. Moreover, radar images at these bands are less influenced by surface slicks and

unhomogeneities in the wind field. As a result, at higher wind speeds, the quality of the depth maps produced by BAS from C-band images degrades because the image modulations become weaker relative to the speckle noise, and they are smeared out over a larger area due to the effect of long waves, which also add noise. Only in areas with smoother depth features like the shoals in the Wadden Sea, the restrictions on the radar images are less severe. It is reasonable to expect therefore that using L-band more accurate results could be obtained along with a wider range of applicability.

Similar results have been derived in an independent study conducted by Greidanus et al. [77]. The article concerns a submerged reef near the island of Heligoland, Germany. In this site the bottom topography is dominated by a series of parallel reefs with very steep slopes, with depths ranging from 4 to 20 m, resulting in very large surface current variations. A depth map of the test site was also constructed, wind data collected and circulation models used to derive sea state information and currents. L-band (both HH and VV polarized), C and X-band (VV-polarized) images of the test site were collected and the resulting bathymetric features analyzed. Different hydrodynamic models were implemented (including that implemented in BAS) and the results compared with the modulations observed in SAR images. Before extracting backscattered features, the surface waves were suppressed by applying filtering techniques in the Fourier domain. All the models gave rather similar results, the main difference being the magnitude of the contrasts. The models with two-scale backscatter and the one with fitted relaxation rate (that is implemented in BAS) have larger contrasts than the ones with Bragg backscatter and relaxation rate modeled by empirical relations. However, even the models that show the highest contrasts still lead to small contrast with respect to the observed one, the effect being stronger in X-band than in L-band. For L-band, contrasts in HH are observed to be larger than in VV, though the effect is small. In the end, L-band imagery is more suited for bathymetry applications than C- or X-band, as the latter are more influenced by the atmosphere and can be less well modeled.

3.2.3 Volterra Series Expansion

A new model, i.e. the inverse model, was introduced by Inglada and Garello [73], [78], [79] able to perform direct inversion from SAR intensity modulation to surface currents. Specifically, they individuated Volterra series expansion as a tool for obtaining an input-output relationship between the current and the SAR image pixel.

Considering both the action spectrum and the surface current in the Fourier domain

$$\begin{aligned}
N(\mathbf{v}) &= \mathcal{F}\{n(\mathbf{p})\} \\
\mathbf{U}(\mathbf{v}) &= \mathcal{F}\{\mathbf{u}(\mathbf{p})\}
\end{aligned}
\tag{3.47}$$

where $\mathbf{v} = (\mathbf{v}_x, \mathbf{v}_y)$ is the sea-wave spatial wavenumber vector and $\mathcal{F}\{\}$ indicates the Fourier transform, the following SAR imaging model can be derived [7]

$$\begin{aligned}
N(\mathbf{v}) &= N_0 + G_{1x}(\mathbf{v})U_x(\mathbf{v}) + G_{1y}(\mathbf{v})U_y(\mathbf{v}) + \\
&\quad G_{2x}(\mathbf{v})U_x^2(\mathbf{v}) + G_{2y}(\mathbf{v})U_y^2(\mathbf{v}) + \\
&\quad G_{2xy}(\mathbf{v})U_x(\mathbf{v})U_y(\mathbf{v}) + \dots
\end{aligned}
\tag{3.48}$$

In eq. 3.48 G_{mz} indicates the m-order kernel of the model along the generic coordinate z . The kernels can be calculated by applying the theory of Volterra Series Expansion (VSE) [73] to solve the ABE under different hypothesis, namely, Bragg scattering [78] or composite scattering model [73], and linear [78] or higher order source functions [73]. Based on the introduced imaging model, underwater bottom topography could be retrieved as follows: surface current variations are calculated from image intensity modulations according to eq. 3.48 and then these current variations are used as input to solve shallow water hydrodynamic and continuity equations.

Unfortunately, even though the availability of an analytical solution of the ABE in the Fourier domain makes the bathymetric SAR problem less intractable from a theoretical point of view, SAR-based bathymetric data retrieval is still very complex. A number of parameters must be set to derive surface current variations. Such parameters include: (a) the coefficients regulating the different scattering contributions [74], (b) the parameters of the selected source function (e.g. relaxation rate, wind conditions, etc.) [72], and (c) the surface and seabed boundary conditions to integrate the shallow water equations, where the former conditions are to be set in terms of surface currents and the latter ones in terms of bathymetry [70]. Most of these parameters cannot be retrieved from the considered SAR image and are sensitive to radar wavelength too. They either need to be acquired from additional sources, or must be measured at the location of the observed scene at the time of SAR acquisition, thus requiring specific acquisition campaigns [50]. The uncertainties on the values of these parameters represent a further error source in the SAR-based bathymetric process [80]. It is therefore clear that the imaging model must be further simplified to be used in bathymetric algorithm that has to work without local measurement campaigns, accurate weather modeling, or complex calibration of the input parameters.

The simplified model is based on the following assumptions: stationary currents, Bragg scattering, linear source function, and second order VSE model. In addition, a reference frame is

introduced in which x and y are the ground range and azimuth directions, respectively. The Bragg wavenumber vector \mathbf{k}_B is thus simplified as

$$\mathbf{k}_B = (k_B, 0) \quad (3.49)$$

where the Bragg wavenumber is [80]

$$k_B = \frac{4\pi \sin \Theta}{\lambda} \quad (3.50)$$

λ is the radar wavelength and Θ is the incidence angle. In this case, only G_{Ix} , G_{2x} and G_{2xy} are non-zero in eq. 3.48 [80]. Moreover, the modulation produced by the linear ground range kernel G_{Ix} is several order of magnitude stronger than those generated by second order kernels G_{2xy} , G_{2x} [78]. The imaging mechanism based on the linear ground range kernel G_{Ix} only is therefore selected as the simplified bathymetric SAR model in this work. The expression of this kernel is [78]

$$G_{1x}(\mathbf{v}) = k_x \frac{\mathbf{c}_g(\mathbf{k}_B) \cdot \mathbf{v} + j\mu(\mathbf{k}_B)}{(\mathbf{c}_g(\mathbf{k}_B) \cdot \mathbf{v})^2 + \mu^2(\mathbf{k}_B)} \left(\mathbf{v} \cdot \frac{\partial N_0(\mathbf{k}_B)}{\partial \mathbf{k}_B} \right) + j\Psi_0(k_B) \frac{R}{V} \sin \Theta v_y \quad (3.51)$$

where j is the imaginary unit, R is the slant range, V is the SAR antenna velocity to the ground, and Ψ_0 is the height spectrum of Bragg waves at the equilibrium [7], [74]

$$\Psi_0(k_B) = \frac{a_P}{\rho} \frac{k_B^{-3}}{\omega_0^2(k_B)} \quad (3.52)$$

In eq. 3.52 ρ is the sea water density. From the dispersion relation of the short waves, the frequency of Bragg waves is [43]

$$\omega_0(k_B) = \sqrt{gk_B + \frac{\sigma_w}{\rho} k_B^3} \quad (3.53)$$

where g is gravity acceleration and σ_w is the surface tension for the boundary between air and water. The gradient of the action spectrum with respect to the Bragg wavenumber vector in eq. 3.51 is

$$\frac{\partial N_0(\mathbf{k}_B)}{\partial \mathbf{k}_B} = \left(\frac{\partial N_0}{\partial k_B}, 0 \right) \quad (3.54)$$

with

$$\frac{\partial N_0(k_B)}{\partial k_B} = -\frac{a_P}{\omega_0(k_B)} (4 + \gamma) k_B^{-5} \quad (3.55)$$

where γ is the group velocity to the phase velocity ratio [43]. Eq. 3.55 can be derived from eqs. 3.41, 3.50, and 3.53 considering that $N_0(k_B) = n_0(k_B)$. The values \mathbf{c}_g and γ for Bragg waves can be calculated as

$$\begin{aligned} \mathbf{c}_g(\mathbf{k}_B) &= (c_g, 0) \quad , \quad c_g(k_B) = \frac{g}{2\omega_0(k_B)} \left(1 + 3 \frac{\sigma_w}{\rho} k_B^2 \right) \\ \gamma &= \frac{k_B}{\omega_0(k_B)} \frac{\partial \omega_0(k_B)}{\partial k_B} = \frac{g k_B}{2\omega_0^2(k_B)} \left(1 + 3 \frac{\sigma_w}{\rho g} k_B^2 \right) \end{aligned} \quad (3.56)$$

Finally, as far as the relaxation rate is concerned, different models exist to predict its value as a function of parameters like wind velocity, radar wavelength [72], [74]. Unfortunately, the accuracy of these models rapidly degrades with the accuracy of the available weather information [81]. In the present case, where accurate local weather data cannot be exploited, the relaxation rate models are of limited practical utility.

After some algebra, the linear ground range kernel can be formulated as [7]

$$G_{1x}(v_x, v_y) = -a_p \frac{4 + \gamma}{\omega_0(k_B)} \frac{c_g(k_B) v_x + j\mu(k_B)}{c_g^2(k_B) v_x^2 + \mu^2(k_B)} k_B^{-4} v_x + j\Psi_0(k_B) \frac{R}{V} \sin \Theta v_y \quad (3.57)$$

It is worth noting that $G_{1x}(0,0) = 0$. Since $\mathbf{U}(0,0)$ is the continuous component of \mathbf{U} and represents a constant surface current, this property of the linear ground range kernel corresponds to the physical condition that, when the bathymetry does not change, or the local depth is so high that it cannot affect significantly the current field, the surface current is constant and no intensity modulations result in the SAR image. As previously discussed, the constant current condition corresponds to the equilibrium condition for short surface waves, i.e. $\mathbf{U}(0,0) = \mathbf{U}_0 = \mathbf{u}_0$. The resulting simplified imaging model can be thus rewritten as

$$\begin{aligned} \Delta N(v_x, v_y) &= G_{1x}(v_x, v_y) \Delta U_x(v_x, v_y) \\ \Delta U_x(v_x, v_y) &= U_x(v_x, v_y) - U_{x0} \\ \Delta N(v_x, v_y) &= N(v_x, v_y) - N_0 \end{aligned} \quad (3.58)$$

From eqs. 3.46-3.47, and 3.58, the model can be finally expressed as a function of image intensity

$$\frac{\Delta i(x, y)}{i_0} = \mathcal{F}^{-1} \left\{ \frac{G_{1x}(v_x, v_y) \Delta U_x(v_x, v_y)}{N_0} \right\} \quad (3.59)$$

According to eqs. 3.58-3.59, it follows that the imaging model based on the linear ground range kernel is sensitive to the ground range component of current velocity. In addition, the equilibrium current velocity $\mathbf{u}_0 = (u_{x0}, u_{y0})$ cannot be derived from SAR imaging, which is only

sensitive to ground range velocity variation with respect to the equilibrium value. Finally, since only normalized relative variations of the energy spectral density are of interest, the true value of a_P is unnecessary for bathymetric data retrieval. Actually, to all the practical purposes, this constant can be set to one [7].

The linear ground range kernel includes three different contributions: relaxation, advection, and velocity bunching. It is well-known that the main term contributing to the linear kernel is the relaxation [37], which depends on the relaxation rate and regulates the reaction time of the short wave spectrum to current variations. Neglecting advection and velocity bunching, the linear ground range kernel becomes

$$G_{1x} |_{relaxation} (v_x) = -\frac{4 + \gamma}{\mu} jN_0 v_x \quad (3.60)$$

Under this assumption, the first example of bathymetric SAR model was derived in [37], leading to a direct relation between image intensity modulations and the slope of the ground range bathymetric profile. Fig. 3.10 shows the magnitude and the phase of the linear ground range kernel (solid lines) when only the relaxation is taken into account. The graphs are derived using the parameters listed in Tab. 3.1 and representing typical values for COSMO-SkyMed SAR sensor in stripmap mode [82]. The relaxation term is a filter passing all the frequencies except those in a stop band centered on the continuous component. Again this result agrees with the consideration that the continuous component of the current velocity, i.e. the equilibrium current velocity, cannot be estimated from SAR images, but only current variations can be measured.

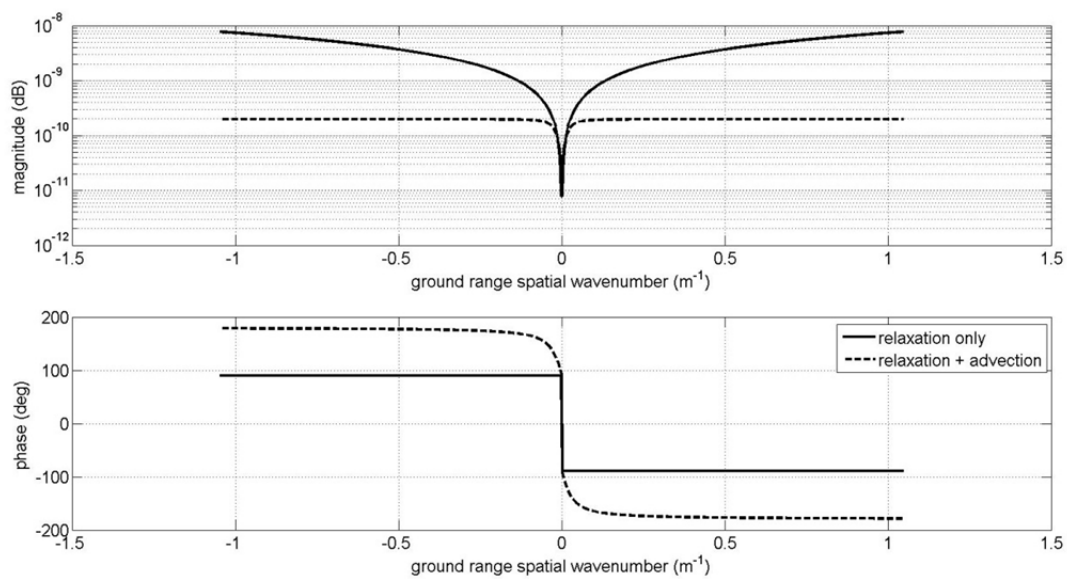


Fig. 3.10 Comparison between the magnitude (*top*) and the phase (*bottom*) of the linear ground range kernel derived considering both relaxation and advection and relaxation only [7].

Symbol	Parameter	Value
λ	radar wavelength	0.031 m
	orbital altitude	620 km
V	velocity to the ground	7 km/s
Θ	incidence angle	33°
	ground range sampling distance	3 m
	azimuth sampling distance	3 m
μ	relaxation rate	0.005 s ⁻¹
U_{x0}	equilibrium current velocity	0.25 m/s
d_0	depth corresponding to the equilibrium current velocity	25 m
$\Delta d/2$	maximum depth variation	5 m
F_L	scale length of the bathymetric feature	1000 m

Tab. 3.1 List of the parameters used to evaluate the linear ground range kernel (typical values for COSMO-SkyMed SAR sensor in stripmap mode [83]).

Concerning the advection term, it is regulated by the group velocity of Bragg waves. When both relaxation and advection are considered, the linear ground range kernel is

$$G_{1x} |_{relax.+advect.} (v_x) = -(4 + \gamma) N_0 \frac{c_g v_x + j\mu}{(c_g v_x)^2 + \mu^2} v_x \quad (3.61)$$

As shown by Fig. 3.10 (dashed lines), the advection term has a double effect on this kernel. First, looking at the magnitude, it has no practical effect on low frequencies, whereas it reduces the amplitude of image intensity modulations at high frequencies. Considering the phase behavior, instead, the advection is able to modify the phase of the kernel. This latter effect is typically more significant than the former one. According to the shifting property of the Fourier transform, varying the phase generates a backward or forward shift of the resulting intensity modulation in the space domain. In other words, for the same bathymetric profile and equilibrium current, similar intensity modulations are foreseen by relaxation only and relaxation plus advection, but the intensity profile is shifted backward or forward when advection is taken into account. This consideration, in agreement with the results in [72], shows that advection is important to relate the peaks of the intensity modulation to the peaks of the bathymetric profiles correctly, thus reducing the geolocation error of the retrieved depth maps.

When the ground range current field is characterized by a gradient along the azimuth direction, this gradient gives rise to the velocity bunching, according to the relevant term in the linear ground range kernel

$$G_{1x} \Big|_{relax.+advect.} (v_x) = -(4 + \gamma) N_0 \frac{c_g v_x + j\mu}{(c_g v_x)^2 + \mu^2} v_x \quad (3.62)$$

The magnitude and the phase of this term are shown in Fig. 3.11, where the values listed in Tab. 3.1 are again used for the parameters of interest.

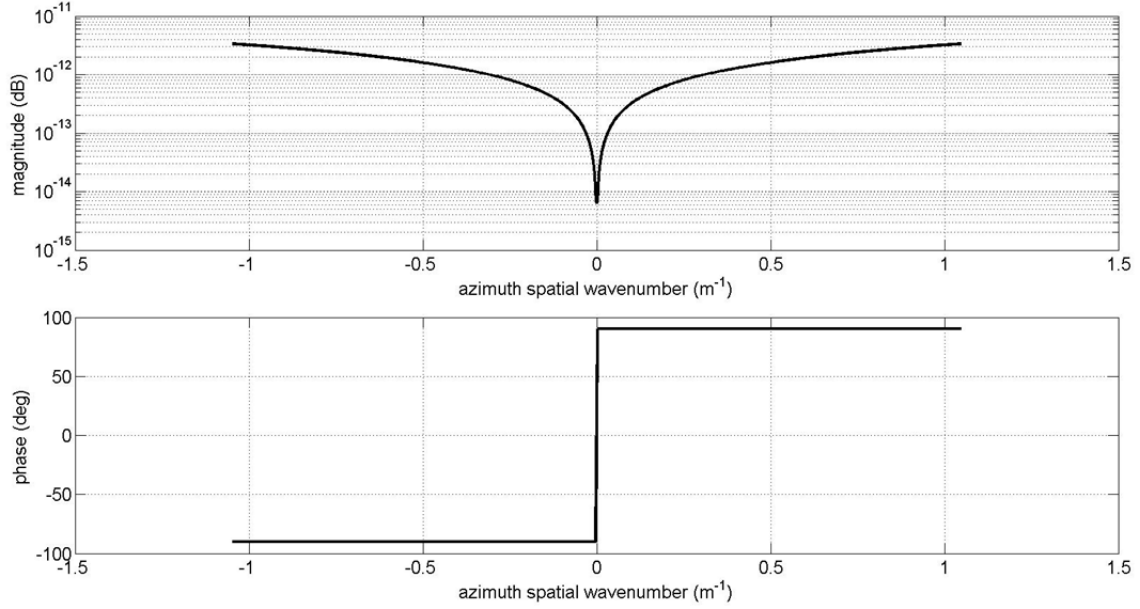


Fig. 3.11 Magnitude (*top*) and the phase (*bottom*) of the velocity bunching contribution to the linear ground range kernel [7].

Since the velocity bunching term is some orders of magnitude lower than the relaxation and advection ones, relaxation and advection only are used herein to generate an example of image intensity profile along the ground range direction. The simulation builds on the following assumed variation of the seabed:

$$d(x) = d_0 + \frac{\Delta d}{2} \cos\left(\frac{2\pi}{F_L} x\right) \exp\left(-\frac{1}{2} \frac{x^2}{(F_L/2)^2}\right) \quad (3.63)$$

where $d(x)$ is the depth at the ground range position x , $\Delta d/2$ represents the maximum depth variation from the mean value d_0 , and F_L is the wavelength of the sinusoidal profile. The depth profile is illustrated in the top diagram of Fig. 3.12, according to the parameters of Tab. 3.1. The sinusoid depth variation is damped down to the mean depth value by the Gaussian-like exponential term. Starting from the equilibrium current velocity, the current profile corresponding to the introduced bathymetry can be derived by the one-dimensional stationary laminar flow continuity equation

$$d(x) u_x(x) = u_{x0} d_0 \quad (3.64)$$

Finally, the intensity modulation due to bathymetry can be calculated from eq. 3.59, assuming $v_y = 0$ (i.e. no velocity bunching) and using the parameters listed in Tab. 3.1.

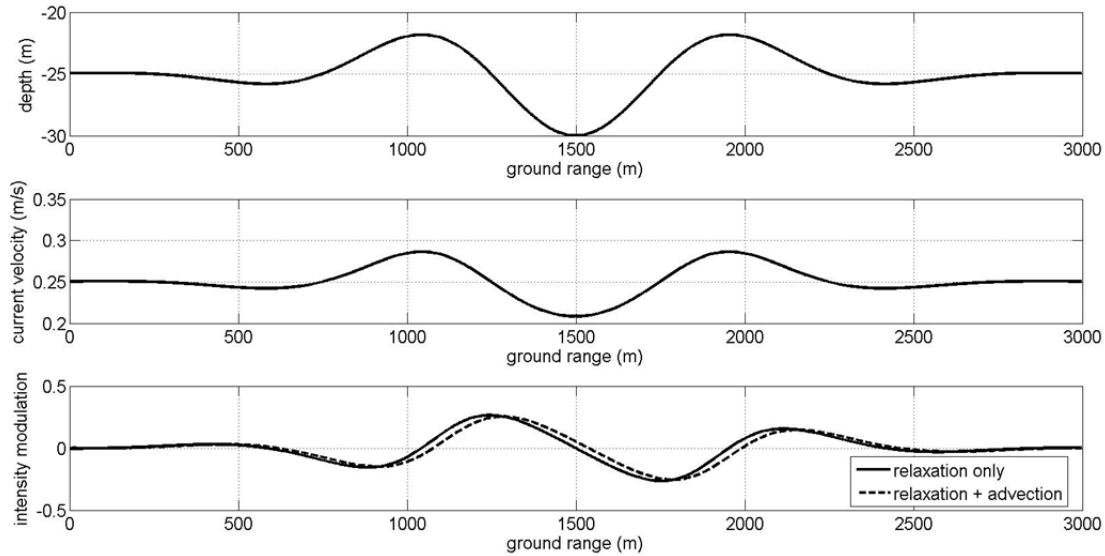


Fig. 3.12 Simulated image intensity profile (*bottom*) corresponding to the considered bathymetry (*top*) and current velocity (*middle*) [7].

As shown in Fig. 3.12, the model predicts intensity modulations characterized by alternating bright (decreasing depth) and dark (increasing depth) areas. When only relaxation is considered, the modulation is proportional to the slope of the local depth: it is therefore null when the slope is zero and maximum or minimum when the slope attains its extreme values. In addition, the intensity modulation is in the order of 10-20%, a result which agrees with the values achieved on real SAR data [37], [50], [72], [84]. As expected, the advection term does not change the amplitude of the intensity modulation significantly, but it introduces a backward shift with respect to the bathymetric profile, and therefore the peaks of the intensity modulation do not correspond to the maximum slope values any more. Even when the advection is taken into account, the peaks of the intensity modulations show the same frequency as the depth profile. Actually, this consideration explains why underwater features can be imaged and recognized in SAR images even if the SAR signal is not able to penetrate the sea surface.

Volterra series expansions have been used for bathymetric data retrieval in a limited number of works [73], [79], [85]. In the works by Inglada and Garello [73], [79] the algorithm reported in Fig. 3.13 has been implemented and tested.

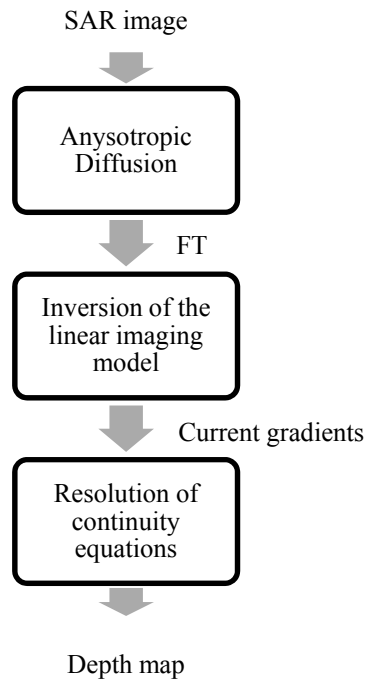


Fig. 3.13 Schematic representation of the approach for SAR-based bathymetric data retrieval proposed by Inglada and Garello and exploiting Volterra series expansion [69], [73].

The first step is used to smooth the SAR image in order to enhance bathymetric features and reduce the noise. This is achieved by the anisotropic diffusion approach [86] that represents a quite assessed technique for image preprocessing. The second step derives surface current gradients by the inversion of the linear kernel. Finally the third step calculates the depth values by continuity equations.

The method has been applied on L-band VV-polarized E-SAR airborne data, gathered in the North Sea, near Dutch coast. The test area was a square 5 km x 5 km wide, covered by asymmetric sand waves approximately perpendicular to the dominant tidal current. A reference DEM was calculated by echo-sounder data. The mean depth of the test area was about 25 m; the sand waves were characterized by a mean height of 5 m and crest-to-crest distance of 500 m. The tidal current was about 1 m/s during SAR data collection with a wind speed of about 3.5 m/s. SAR data were acquired with sand waves oriented parallel to the azimuth direction (i.e. the best configuration for imaging bathymetric features) and from 50° side-looking angle. A quantitative analysis of the results has not been reported in the available papers, however it has been observed that, without using in input any depth measurements coming from echo-sounders, the phasing between the estimated depth profiles and the reference ones was very good, even though the amplitude of sand waves was not always reproduced well (up to 1 m error).

The same approach has been also implemented by Marghany et al. [86] and tested on both L-band and C-band TOPSAR airborne data collected over the coastline of Kuala Terengganu, Malaysia. The main modification introduced by Marghany et al. to the algorithm reported in Fig. 3.13 is the introduction of an additional step after the resolution of continuity equations. This step is based on a fuzzy B-spline method used to interpolate among local depth measurements derived by resolving the continuity equation after the inversion of the linear mono-dimensional kernel of Volterra series expansion (actually this step deals with DEM generation phase and not specifically with bathymetric data retrieval). The achieved results show satisfactory correlations between the derived maps and the reference ones, with better results obtained from L-band data.

3.2.4 Synthesis and discussion

The current-based imaging of bathymetric features by SAR can be modeled through the following three-steps mechanism:

- 1) Interaction between tidal flow and bottom topography produces variations in the current velocity at the sea surface.
- 2) Variations in the surface current velocity give rise to modulations in the wind generated spectrum of water waves.
- 3) Modulation in the surface roughness causes variations in the radar backscatter and therefore it shows up as amplitude modulation in radar images.

This mechanism is activated, that is bathymetric features are actually imaged, only under moderate wind-speeds (3-12 m/s) and strong currents (≥ 0.5 m/s). Alpers and Hennings proposed the first model to quantify the contributions of each step of the imaging of bathymetric features. According to this model, surface current gradients generated by the bottom topography produce a modulation of the spectrum of Bragg surface waves increasing Bragg wave energy (i.e. surface roughness) in correspondence of strong current gradient. Sea surface zones featuring increased roughness appear brighter in SAR images. Under a series of approximations Alpers and Hennings were able to derive a simple analytical expression, based on a first-order solution of the Action Balance Equation, relating the gradient of bottom depth to the expected SAR image intensity variation. The expression can be used to individuate the best and the worst observation geometry for the imaging of bathymetric features. Specifically, the best observation geometry occurs when: (a) ridges are parallel to the flight direction and (b) current is orthogonal

to the ridges. On the contrary less bright bathymetric features are derived when (a) ridges are almost orthogonal to flight direction and (b) current flow is parallel to the ridges.

The approximations introduced by Alpers and Hennings are very useful to describe qualitatively what is then observed in SAR images, but they represent an oversimplification if SAR images have to be used to derive bottom bathymetry. For this reason a different approach has been selected and implemented in the first (and also, till now, the only) commercial system for bathymetric data retrieval, developed by ARGOSS, a Dutch company. The system is named Bathymetry Assessment System, BAS. BAS is based on the so-called forward model, that is SAR image is not “inverted” to obtain bathymetric data, but a-priori bathymetric information coming from external sources (such as measurements derived by echo-sounders) are used to simulate the SAR image. The simulated SAR image is compared to the real one. The differences between the images, due to inaccuracies of the bathymetric information used to simulate the image, are used to start an iterative procedure aimed at converging to the best estimate of the bottom bathymetry.

The simulation of SAR image from a known bathymetry is therefore the crucial step in BAS. It includes the numerical resolution of ABE and the implementation of Bragg scattering model. BAS has been successfully applied to bathymetric data retrieval from SAR images (mainly C-band) over Dutch coasts. The system demonstrated decimeter level accuracy but suffers from important limitations:

- 1) A significant amount of echo sounder measurements must be available. Actually SAR images are merely used to interpolate between the transects of bathymetric data collected by echo-sounders.
- 2) The model used to simulate SAR images is actually quite complex even though approximated. As noted above, it is based on the numerical resolution of ABE and on Bragg scattering, but also on the proper adjustment of specific parameters, such as the relaxation rate. In addition local weather data, such as wind measurements and sea wave state must be available.
- 3) BAS is not a fully automatic system. Human-in-the-loop is always needed not only to remove features not dealing with local bathymetry (such as ships or image artifacts) but also to control the convergence of the iterative procedure implemented to estimate bathymetry.

Some of these limitations can be smoothed considering an inverse approach, relying on the so-called inverse model. The inverse model represents the direct inversion from SAR images to surface currents and then to bathymetry. The possibility to exploit this approach is based on the

availability of a model relating the SAR image to surface current (or current gradient), and on the capability of inverting this model. Inglada and Garello developed such a kind of model resolving the ABE equation by expanding the action spectrum with respect to surface current in Volterra series. The exploitation of Volterra series expansion allowed them to relate the Fourier Transform of SAR images to the Fourier Transform of surface current, thus also deriving a model for inverting SAR images that is actually based on well-assessed image processing tools (such as Fourier Transform and anisotropic diffusion filtering). In the end, the model developed by Inglada and Garello has been demonstrated to be able to potentially derive bathymetric data without using in input any a-priori bathymetric measurements other than a single reference depth value. For this reason and as result of this part of the study, this approach has been considered worth of further analysis.

Concerning the kind of SAR data useful to derive bathymetric measurements by current-based techniques, it is important to remark that such techniques have been successfully applied to L-band, C-band and X-band SAR images, even if with different performance and issues. In general it is possible to state that L-band bathymetric features appear clearer than those imaged by C-band and X-band SAR. This can be explained considering that L-band images of sea are less influenced by local winds that are able, instead, to partially cover bathymetric features in X-band and C-band images. In addition, the conventional modeling approach, based on ABE and Bragg scattering, properly applies only to L-band data; for C-band and X-band data higher-order scattering mechanisms must be taken into account. Finally, concerning L-band, HH polarization should be preferred.

Chapter 4

Error Budget Analysis

The present chapter investigates the identified SAR-based bathymetric techniques, both the one based on swell waves and the one based on sea currents. An error budget is developed for both of them. Moreover, viability and potential performance of the investigated bathymetric techniques are discussed with specific reference to SAR data.

4.1 Wave-Based Approach (WBA) based on the Linear Dispersion Relation

Phenomena of swell wave shoaling and refraction due to underwater morphology start appearing in intermediate water depth because surface waves begin to feel the bottom when seawater depth, h , is shorter than about half of the swell wavelength, L [39]:

$$h < 1/2 L \quad (4.1)$$

This means that bathymetry through swell wave modulation can be performed only for water depth values lower than half the swell wavelength, that is, the limit water depth value. This limit cannot be univocally defined since swell wavelength depends on the considered case. Specifically, the standard expression of the linear dispersion relation (eq. 3.10) can be used in intermediate water depth, i.e. for water depth in the range $[(1/20)*L; (1/2)*L]$.

A more useful form of the linear dispersion relation for SAR based bathymetry data retrieval in intermediate water depth can be derived directly relating to the water depth

$$h = \frac{1}{k} \tanh^{-1} \left(\frac{\omega^2}{gk} \right) \quad (4.2)$$

or, equivalently

$$h = \frac{L}{2\pi} \tanh^{-1} \left(\frac{2\pi L}{T^2 g} \right) \quad (4.3)$$

where,

- h is the water depth;
- k is the wave number of the gravity wave;
- ω is the angular frequency of the gravity wave;
- L is the wavelength of the gravity wave and it is $L = 2\pi/k$;
- T is the period of the gravity wave and it is $T = 2\pi/\omega$;
- g is the gravity acceleration.

4.1.1 Applicability of the Linear Dispersion Relation

This section analyzes the theoretical behavior of the linear dispersion relation in intermediate water depth. Therefore, for each considered swell wavelength only the values of water depth less than half that wavelength shall be considered. In addition, only the wavelength satisfying

the relation $\left| \frac{2\pi L}{T^2 g} \right| < 1$ has to be taken into account due to the \tanh^{-1} function in eq. 4.3. This

means that for each swell wavelength, a lower limit value for the swell period has to be considered [87]

$$T_{MIN} = \sqrt{\frac{2\pi L}{g}} \quad (4.4)$$

Figure 4.1 and Fig. 4.2 show the relation between water depth, swell wavelength, and swell period in coastal areas for typical ranges of swell wavelength $L \in [20; 300]$ m, and swell period $T \in [4; 33]$ s. Figure 4.1 shows that for constant swell wavelength, the water depth decreases when the swell period increases. On the contrary, if swell period is constant, swell wavelength decreases when water depth decreases too; the longer the swell wavelength is, the steeper the slope of this trend is. The absolute value of the slope increases at short swell wavelength thus leading to large uncertainty in water depth estimation based on swell period. Indeed, a small error in the swell period is amplified by the linear dispersion relation for short values of the swell wavelength thus leading to a large error in the estimated water depth [87].

Figure 4.2 shows that the longest acceptable value for the measured swell wavelength, i.e. the largest acceptable value for the estimated water depth, depends on the considered value of swell period. The shorter the swell period is, the shorter the maximum acceptable swell wavelength is. In particular, for large swell periods this value is outside the range of valid swell wavelength. Absolute value of the slope increases for long swell wavelength thus leading to large uncertainty in water depth estimation especially for little swell period. Indeed, even a small error in swell wavelength leads to a large error in the estimated water depth [87].

According to the performed analysis a further remark can be made. When the swell period is sufficiently large and the local depth is quite limited, variations in the swell period are expected to generate very limited variations in the estimated water depth, i.e. the sensitivity of water to swell period is very low [87].

This property turns to be very useful for SAR-based bathymetry since it allows a first-guess approach to be used to estimate swell period [39].

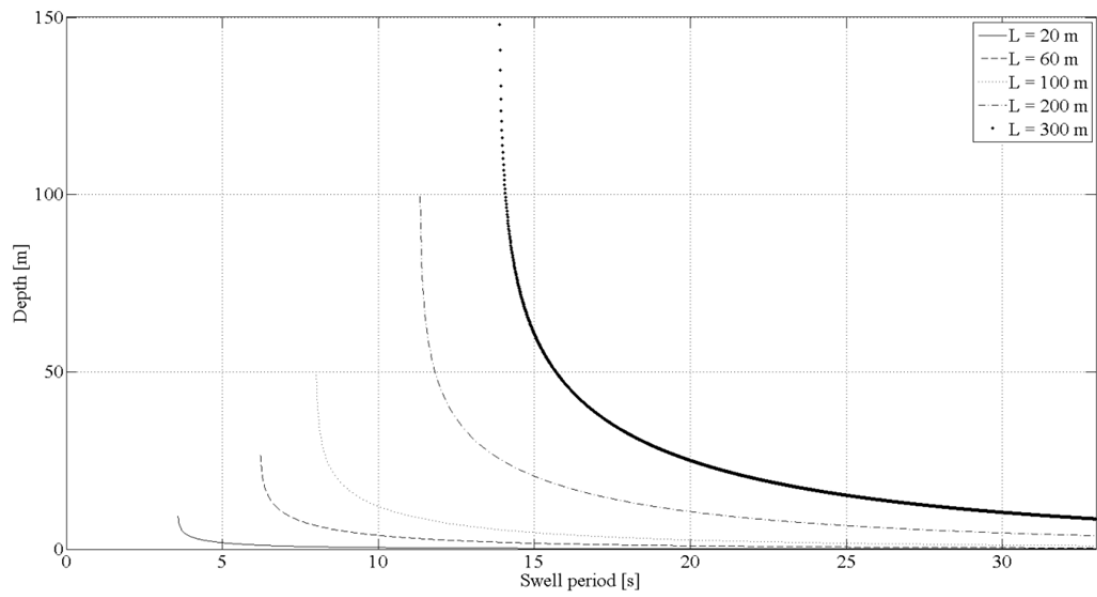


Fig. 4.1 Sea water depth as function of swell period for different values of swell wavelength, L , in the range [20; 300] m, according to the linear dispersion relation starting from intermediate water depth up to shoreline.

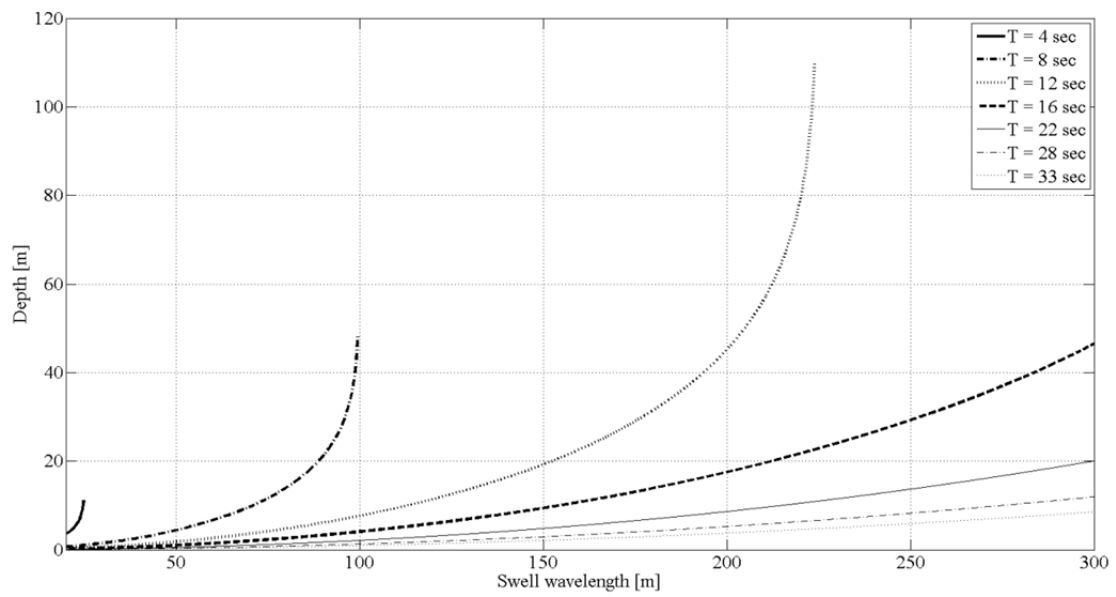


Fig. 4.2 Sea water depth as function of swell period for different values of swell period, T , in the range [4; 34] s, according to the linear dispersion relation starting from intermediate water depth up to shoreline.

4.1.2 Error budget analysis - WBA

An error budget model is presented in this section to investigate the potential performance of the linear dispersion relation. The case of swell waves fully characterizing sea surface at the moment of SAR image acquisition is considered, that is when no other significant features are present and linear SAR imaging can be assumed. For any given model of water depth estimation, $h = h(S_1, S_2, \dots, S_n)$, the basic propagation formula for variance of water depth, σ_h^2 , in terms of all the related error sources (S_1, S_2, \dots, S_n) is given by

$$\sigma_h^2 = \sum_i \left(\frac{\partial h}{\partial S_i} \right)^2 \sigma_{S_i}^2 + \sum_{i \neq j} \frac{\partial h}{\partial S_i} \frac{\partial h}{\partial S_j} \sigma_{S_i, S_j} \quad i = 1, \dots, n; j = 1, \dots, n. \quad (4.5)$$

With reference to the linear dispersion relation (eq. 4.3), the statistical correlation between error sources, i.e. the second summation in eq. 4.5, is neglected. The variance of the estimated water depth [87] is obtained by adding $\sigma_{h|_L}^2$, i.e. the square of the water depth uncertainty due to the one in the swell wavelength, σ_L , to $\sigma_{h|_T}^2$, i.e. the square of the water depth uncertainty due to the one in the swell period, σ_T

$$\sigma_h^2 = \left(\frac{\partial h}{\partial L} \right)^2 \sigma_L^2 + \left(\frac{\partial h}{\partial T} \right)^2 \sigma_T^2 = \sigma_{h|_L}^2 + \sigma_{h|_T}^2 \quad (4.6)$$

The analytic formula for the sensitivities, that is the partial derivatives $\frac{\partial h}{\partial L}$ and $\frac{\partial h}{\partial T}$, can be derived by differentiation of the linear dispersion relation (eq. 4.3)

$$\frac{\partial h}{\partial L} = \frac{1}{2\pi} \tanh^{-1} \left(\frac{2\pi L}{T^2 g} \right) + \frac{L}{T^2 g} \frac{1}{1 - \left(\frac{2\pi L}{T^2 g} \right)^2} \quad (4.7)$$

$$\frac{\partial h}{\partial T} = -L \frac{1}{1 - \left(\frac{2\pi L}{T^2 g} \right)^2} \frac{2L}{T^3 g} \quad (4.8)$$

Equations 4.7 and 4.8 show that $\sigma_{h|_L}$ and $\sigma_{h|_T}$ depend on wavelength and period of the swell wave field propagating in the considered portion of sea surface. In particular, the larger the

swell period is, the lower the sensitivities are. On the contrary, if a short value of swell period is assumed, large sensitivities occur thus leading to a large σ_h^2 also with limited σ_L and σ_T .

In order to avoid large errors in the estimation of water depth, an upper limit for sensitivities is introduced [87]. Ranges of acceptable values should, therefore, be defined for swell wavelength and swell period, respectively, so that only values of L and T which give

$$\left| \frac{\partial h}{\partial L} \right| \leq \left| \frac{\partial h}{\partial L} \right|_{\text{limit}} \quad (4.9)$$

$$\left| \frac{\partial h}{\partial T} \right| \leq \left| \frac{\partial h}{\partial T} \right|_{\text{limit}} \quad (4.10)$$

shall be used for bathymetric data retrieval. Limit values for sensitivities must be selected depending on the accuracy desired for the bathymetric survey.

In the present study, the cut-off value of 7.76 has been considered reasonable for both $\left| \frac{\partial h}{\partial L} \right|_{\text{limit}}$ and $\left| \frac{\partial h}{\partial T} \right|_{\text{limit}}$ [87]. It is equivalent to the value of $\left| \frac{\partial h}{\partial T} \right|$ obtained from (14) by considering $L = 200$ m and $h = 30$ m. Figure 4.3 shows that for each value of swell wavelength, two lower limit values of swell period are obtained: one related to $\left| \frac{\partial h}{\partial L} \right|_{\text{limit}}$ and the other one related to $\left| \frac{\partial h}{\partial T} \right|_{\text{limit}}$.

Since eqs. 4.9 and 4.10 must be satisfied at the same time, only values (L, T) in the area above both the two curves can be used. In the considered case, the admissible area is the same as considering only the condition expressed by eq. 4.10. The minimum acceptable swell period rises as the swell wavelength increases. The more the two curves are close to each other, the more the values of $\left| \frac{\partial h}{\partial L} \right|$ on the boundary of the admissible area are close to $\left| \frac{\partial h}{\partial L} \right|_{\text{limit}}$.

Figure 4.3 also shows that setting the upper limit for sensitivities is the same as considering a range of potentially inferable values of water depth. As expected, values of water depth rapidly increase approaching the $\left| \frac{\partial h}{\partial T} \right|_{\text{limit}}$ curve but, in the considered case, values within 30 m are obtained in almost the whole admissible area of the (L, T) plane. The above-reported considerations are of general validity, that is they depend only on the properties of the dispersion relation and so they hold independently of the technique used to calculate

wavelength and period. On the contrary, uncertainties in the error sources, i.e. in swell wavelength, σ_L , and in swell period, σ_T , depend on the adopted technique.

With specific reference to SAR imaging, the value of σ_L basically depends on the spatial resolution of the inspected SAR image. On the other hand, the value of σ_T depends on the accuracy of the sources that provide the swell period or, in case a first guess approach is used, on the accuracy of the assumed offshore water depth. Ranges of possible values for σ_L and σ_T have been considered to evaluate the performance of the linear dispersion relation for bathymetric data retrieval. Typical values of high spatial resolution (spotlight SAR image) and medium spatial resolution (stripmap SAR image) have been adopted as minimum and maximum values for σ_L [87], respectively. Therefore, values of $\sigma_L \in [2; 10]$ m have been considered in this work [82], [88]. On the other hand, the minimum and maximum values for σ_T have been retrieved from eq. 4.6 by assuming $\sigma_{h|_r} = 1$ m and $\sigma_{h|_r} = 10$ m, respectively, with $\left| \frac{\partial h}{\partial T} \right| =$

$\left| \frac{\partial h}{\partial T} \right|_{\text{limit}} = 7.76$ m/s [87]. Therefore, values of $\sigma_T \in [0.129; 1.29]$ s have been considered.

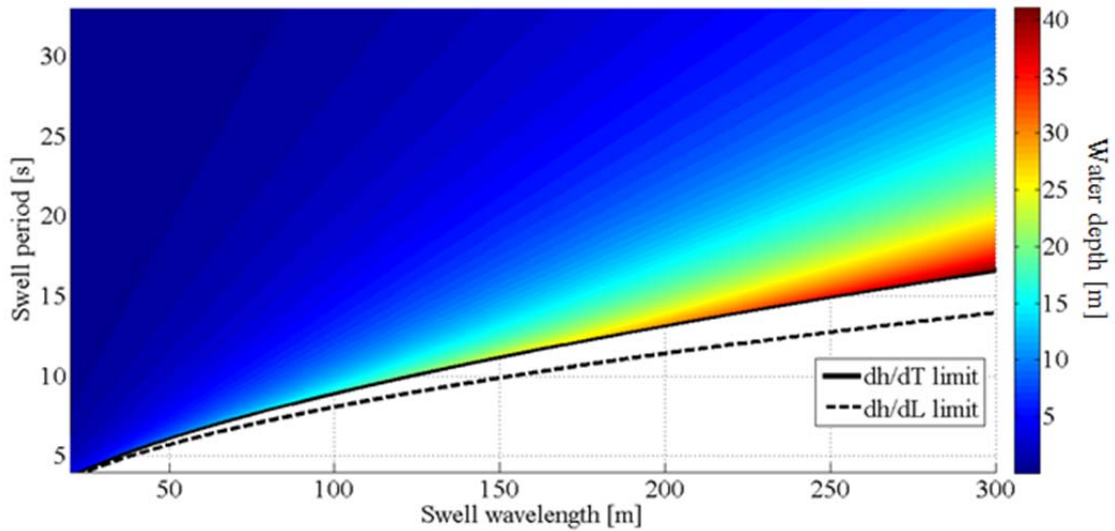


Fig. 4.3 Swell wavelengths and periods which provide $\left| \frac{\partial h}{\partial L} \right| = \left| \frac{\partial h}{\partial L} \right|_{\text{limit}}$ (dotted line) and $\left| \frac{\partial h}{\partial T} \right| = \left| \frac{\partial h}{\partial T} \right|_{\text{limit}}$ (continuous line) together with the water depths calculated from the linear dispersion relation in the considered admissible area of the (L, T) plane.

Figure 4.4 shows the resulting values of $\sigma_{h|L}$ for (L, T) in the considered admissible ranges by assuming the minimum and the maximum values of uncertainty in swell wavelength, respectively. A large zone in the (L, T) plane is characterized by low values of $\sigma_{h|L}$ up to about 0.5 m for $\bar{\sigma}_L = 2$ m, and to about 2.3 m for $\bar{\sigma}_L = 10$ m. Values of $\sigma_{h|L}$ rise in a small region close to the boundary. For long swell wavelength, $\sigma_{h|L}$ rises up to 0.7 m for $\bar{\sigma}_L = 2$ m, and to about 3.5 m for $\bar{\sigma}_L = 10$ m. For low L and T , instead, $\sigma_{h|L}$ can reach values up to 1.8 m for $\bar{\sigma}_L = 2$ m, and to 9 m for $\bar{\sigma}_L = 10$ m since values of $\left| \frac{\partial h}{\partial L} \right|$ are close to $\left| \frac{\partial h}{\partial L} \right|_{\text{limit}}$ in that region.

Similarly, Fig. 4.5 shows the calculated values of $\sigma_{h|T}$ for (L, T) in the considered admissible ranges by assuming the minimum and the maximum values of uncertainty in swell period. As expected, the values of $\sigma_{h|T}$ are quite low for large swell period. A large zone in the (L, T) plane is characterized by short values of $\sigma_{h|T}$ up to about 0.4 m for $\bar{\sigma}_T = 0.129$ s and up to about 4 m for $\bar{\sigma}_T = 1.29$ s. They rapidly increase approaching the boundary and achieve values up to 1 m for $\bar{\sigma}_T = 0.129$ s and up to 10 m for $\bar{\sigma}_T = 1.29$ s. The values of $\sigma_{h|T}$ increase more steeply than $\sigma_{h|L}$ in the area next to the boundary. This is because $\left| \frac{\partial h}{\partial T} \right|$ quickly rises in that region up to the limit value $\left| \frac{\partial h}{\partial T} \right|_{\text{limit}}$.

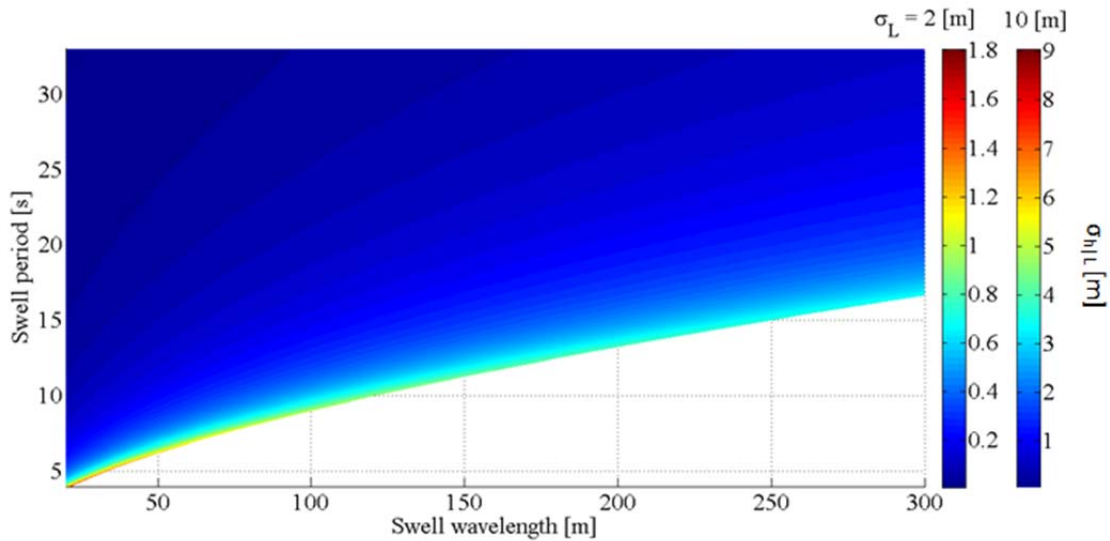


Fig. 4.4 Uncertainty in the estimated water depth due to that in swell wavelength in the considered admissible (L, T) area for $\bar{\sigma}_L = 2$ m and $\bar{\sigma}_L = 10$ m.

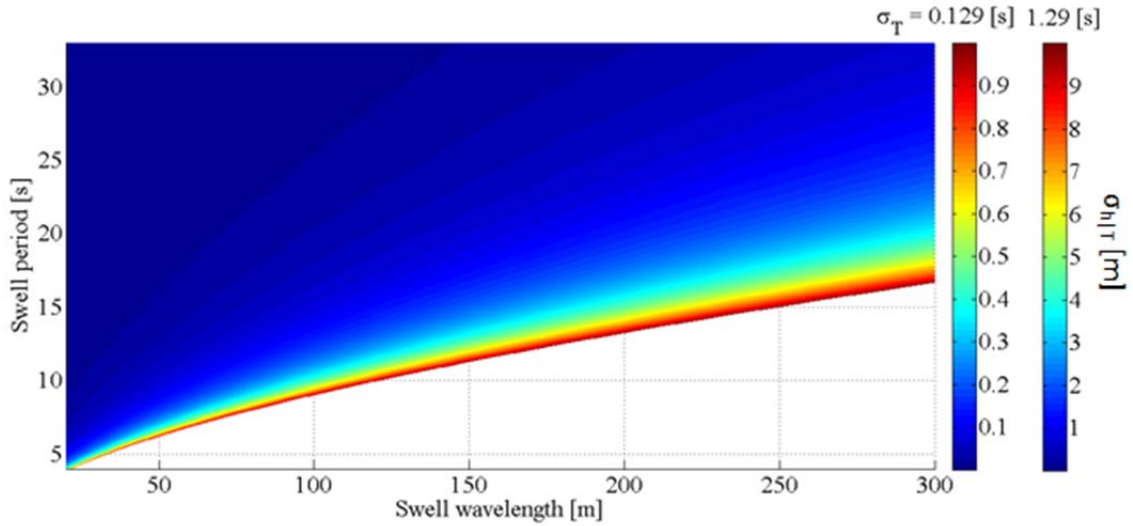


Fig. 4.5 Uncertainty in the estimated water depth due to that in the swell period in the considered admissible (L, T) area for $\sigma_T = 0.129$ s and $\sigma_T = 1.29$ s.

Table 4.1 and Tab. 4.2 report the resulting values of $\sigma_{h|L}$ and $\sigma_{h|T}$, respectively, for some (L, T) values by assuming the minimum and the maximum values of uncertainty in swell parameters.

Finally, the overall uncertainty in water depth has been calculated by eq. 4.6. Figure 4.6 and Tab. 4.3 show the obtained values of σ_h in the two limit cases for both σ_T and σ_L . When the minimum values are considered, i.e. $\sigma_T = 0.129$ s and $\sigma_L = 2$ m, the uncertainty in water depth is estimated to be not larger than about 0.6 m for almost all the acceptable (L, T) values. It increases in the region next to the boundary and, for short values of swell wavelength and period, it reaches values up to 2 m. On the other hand, for maximum input uncertainties, i.e. $\sigma_T = 1.29$ s and $\sigma_L = 10$ m, σ_h gets up to about 4.6 m for a large area in the (L, T) plane, and rises steeply up to about 13 m next to the boundary.

$\sigma_L = 2$ [m]			$\sigma_L = 10$ [m]		
L [m]	T [s]	$\sigma_{h L}$ [m]	L [m]	T [s]	$\sigma_{h L}$ [m]
20	33	0.007	20	33	0.03
22.2	4	1.8	22.2	4	9.0
150	13	0.5	150	13	2.3
300	16.6	0.7	300	16.6	3.5
300	33	0.1	300	33	0.5

Tab. 4.1 Uncertainty in the estimated water depth due to that in swell wavelength, $\sigma_{h|L}$, for different (L, T) and σ_L values.

$\sigma_T = 0.129$ [s]			$\sigma_T = 1.29$ [s]		
L [m]	T [s]	σ_{h_r} [m]	L [m]	T [s]	σ_{h_r} [m]
20	33	0.0003	20	33	0.003
22.2	4	0.97	22.2	4	9.7
150	13	0.4	150	13	4
300	16.6	1.0	300	16.6	10
300	33	0.067	300	33	0.67

Tab. 4.2 Values of uncertainty in the estimated water depth due to that in swell period, σ_{h_r} , for different (L, T) and σ_T values.

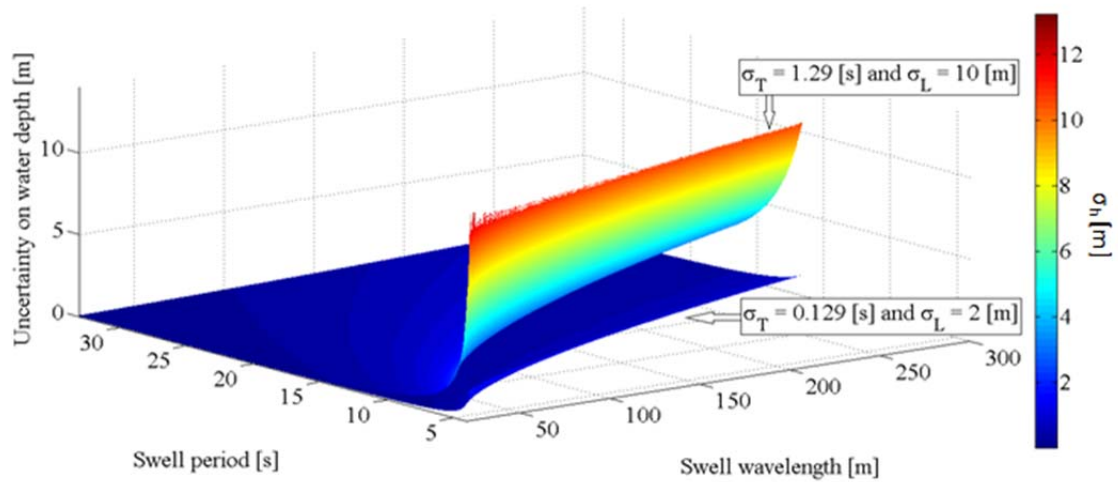


Fig. 4.6 Uncertainty in the estimated water depth in the considered admissible (L, T) area for the minimum and maximum values for both σ_T and σ_L [87].

$\sigma_L = 2$ [m] and $\sigma_T = 0.129$ [s]			$\sigma_L = 10$ [m] and $\sigma_T = 1.29$ [s]		
L [m]	T [s]	σ_h [m]	L [m]	T [s]	σ_h [m]
20	33	0.008	20	33	0.037
22.2	4	2.05	22.2	4	13.2
150	13	0.6	150	13	4.6
300	16.6	1.22	300	16.6	10.6
300	33	0.133	300	33	0.889

Tab. 4.3 Values of uncertainty in the estimated water depth, σ_h , for different (L, T) and (σ_L, σ_T) values.

4.1.3 SAR based products derived from WBA

The swell-based technique is able to generate contour-like charts to describe the bottom morphology. It has been conceived to detect bathymetric features that can be properly represented by a series of contour lines spaced by a quantity at least of the same order of magnitude as the swell peak wavelength in that area. As a consequence, sharp water depth variations are filtered out by the method and cannot be detected. Hence, the bathymetric detection capability of swell-based bathymetry is strictly dominated by the morphological characteristics of seabed, no matter if it is sandy or rocky, and by the range of swell wavelength present within the area of interest. In more detail, the range of swell wavelength sets the range of bathymetric depths that can be measured. If from a theoretical point of view the maximum depth is half the wavelength, the sensitivity analysis conducted in section 4.1.2 shows that the bathymetric depth can be calculated with satisfactory accuracy when the depth is lower than the theoretical limit. An indication of the maximum values for each swell wavelength is reported in Tab. 4.4. The expected range of applicability of the selected WBA is therefore from 40 to 3.5 m for the wavelength varying from 300 to 20 m.

It is worth noting that the detection of underwater features can be enhanced by a careful selection of the SAR images to process. Specifically, particular attention should be paid to the visual inspection of SAR images with a swell waves field propagating along the flight direction of the SAR sensor. Indeed, due to the velocity bunching phenomenon, azimuth propagating waves can be smeared and therefore of limited utility, if not characterized by a wavelength significantly longer than the cut-off length. Its value can be expressed by the empiric eq. 4.11 [39] which links the minimum detectable value of wavelength for swell waves travelling along the azimuth direction, $L_{Min|Azim}$, to the slant range, R , platform velocity, V , and significant wave height, H_s :

$$L_{Min|Azim} = \frac{R}{V} \sqrt{H_s} \quad (4.11)$$

The availability of ancillary information, e.g. related to wind speed or presence of surface currents, even if not strictly necessary, can represent a valuable aid in assessing the applicability of the linear SAR imaging model.

L [m]	T_{MIN} [s]	h_{MAX} [m]
20	4.00	3.5
40	5.46	8.2
60	6.78	11.5
80	7.93	14.5
100	8.96	17.4
150	11.22	23.9
200	13.19	30.0
250	14.97	35.7
300	16.61	41.0

Tab. 4.4 Limit values of water depth, h , for some values of wavelength, L , with the corresponding limit values of wave period, T , by adopting $\left. \frac{\partial h}{\partial T} \right|_{limit} = 7.76$ m/s.

4.1.4 Specifications and requirements - WBA

According to the performed analysis, the following specifications and requirements can be formulated:

- 1) Linear dispersion relation is theoretically able to retrieve values of water depth in the range [5; 40] m.
- 2) The WBA is able to retrieve bathymetric measurements over features characterized by a scale length that is of the same order of magnitude, at least, as the local peak wavelength of the swell waves.
- 3) With specific reference to sea surface state, the considered approach is able to infer sea water depth when swell waves fully characterize the sea surface at the moment of the SAR acquisition, i.e. when no other significant features are present and linear SAR imaging can be assumed. Disturbing phenomena, if present, shall not significantly affect swell parameters or, alternatively, they must be filtered out by proper preprocessing steps [89].
- 4) Particular attention should be given to surface currents since they can cause variations in swell phase velocity and wavelength which generate the same effects as seabed morphology in shallow water [32], [41], [60]. This means that SAR images are useful to

investigate seabed morphology only if acquired under weak current velocity. Quantitatively, current velocity larger than 0.05 m/s should be avoided [32].

- 5) To properly identify bathymetric sea surface features, SAR images with swell waves propagating along the flight direction should be avoided since the velocity bunching phenomenon may cause the minimum discernible wavelength to be longer than that of swell waves propagating along the ground-range direction [41], [90].
- 6) SAR capability to detect swell waves traveling along the ground-range direction strictly depends on the ground-range resolution of the SAR system. In detail, ground-range resolutions lower than five times the swell wavelength allow for accurate and reliable measurements of the swell wavelength to be performed.

For swell travelling along a generic direction, the minimum detectable length ranges from the one along the ground-range dimension, $L_{Min|Range}$, to that along the azimuth direction, $L_{Min|Azim}$. To a first order, being ϕ the angle between the direction of propagation of the swell waves and the platform flight direction, the value of the minimum detectable wavelength, L_{Min} , can be estimated as

$$L_{Min} = \frac{L_{Min|Range}}{2} (1 - \cos(2\phi)) + \frac{L_{Min|Azim}}{2} (1 - \cos(2\phi + \pi)) \quad (4.12)$$

Eq. 4.12 matches the results presented in [64].

Figure 4.7 depicts the simulated trend of the minimum detectable swell wavelength obtained by using typical values for ALOS (Advanced Land Observing Satellite) PALSAR working in stripmap mode, i.e. 6.25 m ground range pixel spacing, $L_{Min|Range}$ five times larger than the resolution, i.e. 31.25 m, 7.59 km/s for the satellite velocity and 848 km for the slant range (corresponding to about 38° incidence angle), and by considering 1 m for the significant wave height. As expected, the performed simulation shows that the value of the minimum detectable wavelength varies in the range [31.25; 111.73] m, shorter for swell waves propagating along the ground-range direction and longer for swell waves propagating along the azimuth one.

Figure 4.8 shows a subset of an ALOS stripmap image, 6.25 m x 6.25 m pixels spacing, covering the west coast of the Ischia Island in the Gulf of Naples, Italy. The sea surface is characterized by a swell field travelling along the ground-range direction with swell wavelength in the range [70 m; 160 m]. This is an example of the conditions in which shoaling and refraction can be tracked and linear SAR imaging can be assumed.

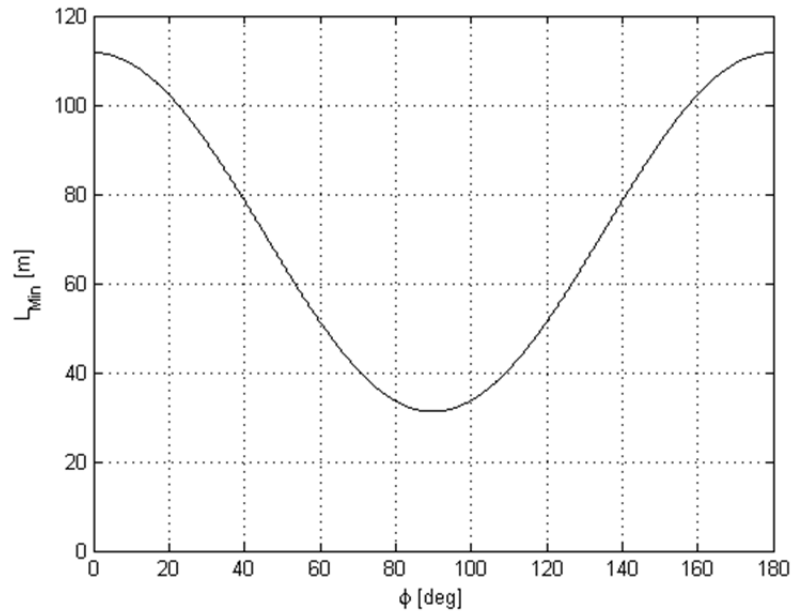


Fig. 4.7 Simulated trend of the minimum value for detectable swell wavelength obtained from equation 4.12 by using typical values for ALOS PALSAR working in stripmap mode (6.25 m ground range pixel spacing), i.e. $L_{Min|Range} = 31.25$ m, $V = 7.59$ km/s, $R = 663$ km, and for $H_s = 1$ m.

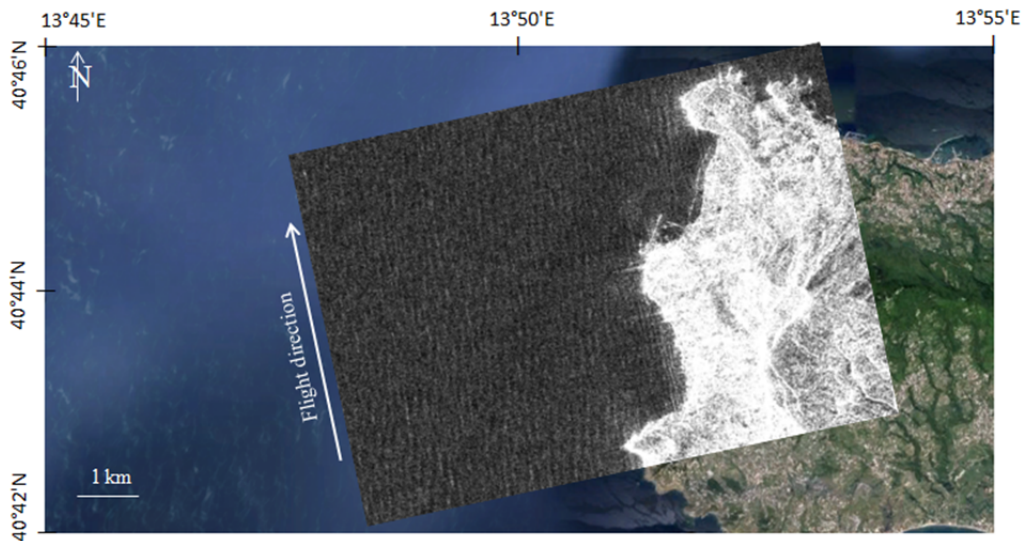


Fig. 4.8 Subset of the ALOS PALSAR stripmap image, 6.25 m x 6.25 m pixel spacing, acquired on February 13th, 2007, at 20:28 UTC, covering the west coast of the Ischia Island in the Gulf of Naples, Italy (background image © Google Earth); swell waves propagate along the ground-range direction and phenomena of shoaling and refraction are well visible approaching the coastline.

- 7) Values of the incidence angle of SAR images should be as short as possible thus reducing the slant range and, therefore, increasing the backscattering from sea surface and reducing undesirable smearing effects [90].

- 8) Amplitude-only data can be used since swell waves are detected as amplitude modulations. Radiometric calibration, at least internal calibration, is also desired along with multi-looked despeckled data able to enhance the features due to bottom topography. Finally, the possibility to use zero-Doppler ground-range/azimuth data, projected onto a reference ellipsoid and resampled at a regular spacing on the ground, is considered important to simplify the bathymetric processing. As a result, with specific reference to COSMOSkyMed standard processing levels [83], Level 1B Products or Detected Ground Multi-look (MDG) products represent the best choice to be used as an input to the method. Polarization does not play a central role, even if cross-polarization data should not be used.

4.2 Current-Based Approach (CBA) based on Volterra Series Expansion

4.2.1 Error budget analysis - CBA

A sensitivity analysis is conducted, based on a direct simulation of SAR imaging mechanism [80]. The simulated SAR data are then inverted and bathymetry is retrieved considering different error sources affecting the inversion process. In this way, the sensitivity of the retrieved bathymetric error to the considered error sources can be determined and an error budget model developed. Different nominal scenarios are considered to generate the simulated SAR images, consisting in sets of parameters used for the computation of the linear kernel and the simulation of sea current variations [80]. The main focus of the analysis is on the most significant sources of uncertainty. They have been identified in those which influence or describe the sea state (current velocity, wind speed measure, etc.) rather than radar data and other information directly related to the radar system (Bragg resonant wavenumber, antenna range and velocity, incidence angle, etc.). Indeed, the data dealing with sea state need to be acquired from different sources than the radar data, and they should have been measured at the location of the observed scene and at the time of the radar acquisition. Both the two latter requirements cannot be satisfied unless a dedicated acquisition campaign is carried out involving ground data collection, which is not of interest for SAR4BAT project applications. As a result, they introduce the largest uncertainty in the computation.

In particular, assuming application of the inversion algorithm on real SAR data, two different classes of sources of uncertainty must be considered [80]:

1. The sources of uncertainty at the stage of computation and inversion of the linear kernel. The linear kernel depends on Bragg wavenumber, group velocity, relaxation rate, radar ground range and velocity. Most of the terms are therefore affected only by SAR sensors and SAR operative mode. For those parameters it is expected that very low uncertainty is achieved, so the relevant uncertainty is neglected in the present analysis and the parameters are assumed to be perfectly known. As a matter of fact, the only parameter not depending on SAR sensor operation is the relaxation rate. Within the considered model, the relaxation rate is essentially a function of wind velocity. Hence, wind velocity uncertainty is considered as the main error source in the computation of the relaxation rate, and therefore in the computation of the kernel used to invert SAR image. In addition, it is important to point out that, since wind velocity uncertainty has no effect on velocity bunching, one-dimensional scenarios can be considered, in which only ground range profiles are simulated, i.e. $\mathbf{u}(x, y) = (\mathbf{u}(x), 0)$.

2. The sources of uncertainty at the stage of solving the continuity equation. Within the considered formulation of the continuity equation, two different sources of uncertainty must be taken into account: (a) velocity of the unperturbed current; (b) sea depth corresponding to the unperturbed current.

The bathymetric error due to these two classes of uncertainties is assessed in the following subsections considering eight nominal scenarios by varying SAR carrier frequency (L-band or X-band), depth range of the bathymetric feature, and depth of the unperturbed current according to the values reported in Tab. 4.5.

Parameter	Value
Depth corresponding to the unperturbed current, d_0	10 m; 25 m
Amplitude of depth variation, Δd	3 m; 10 m
Radar signal wavelength, λ	0.03 m; 0.24 m

Tab. 4.5 List of the parameters used to simulate the variations of surface current velocity due to bathymetry.

According to the continuity equation, the following functional model can be assumed for the retrieved depth

$$d(d_0, u_0, \Delta u(x)) = \frac{d_0 u_0}{u_0 + \Delta u(x)} \quad (4.13)$$

where $\Delta u(x)$ is calculated from the inversion of SAR intensity image and d_0 and u_0 must be provided by external sources. If only random, uncorrelated errors are considered, the propagation formula for the variance of d in terms of the variance (uncertainty) of all the error sources is

$$\sigma_d^2 = \left(\frac{\partial d}{\partial d_0} \right)^2 \sigma_{d_0}^2 + \left(\frac{\partial d}{\partial u_0} \right)^2 \sigma_{u_0}^2 + \left(\frac{\partial d}{\partial \Delta u} \right)^2 \sigma_{\Delta u}^2 \quad (4.14)$$

where σ^2 indicates the variance. In the present case the sensitivities (partial derivatives) can be easily derived

$$\sigma_d^2 = \left(\frac{u_0}{u_0 + \Delta u} \right)^2 \sigma_{d_0}^2 + \left(\frac{d_0 \Delta u}{(u_0 + \Delta u)^2} \right)^2 \sigma_{u_0}^2 + \left(\frac{d_0 \Delta u}{(u_0 + \Delta u)^2} \right)^2 \sigma_{\Delta u}^2 \quad (4.15)$$

The uncertainties σ_{d_0} and σ_{u_0} depend on the accuracy of the external sources exploited to estimate d_0 and u_0 , respectively. In the present case 0.1 m/s reference current uncertainty and 0.5 m depth uncertainty are considered [80], where the latter is compatible with reference depth data derived from a nautical chart.

The uncertainty $\sigma_{\Delta u}$ depends on the accuracy of the procedure implemented to invert SAR image and derived sea current variations. This uncertainty is essentially affected by the availability of accurate wind speed measurements.

The uncertainty on the sea current variation is determined simulating the eight scenarios and then inverting the simulated SAR image on the basis of a linear kernel in which wind speed error is included, corresponding to relaxation rate error.

Assuming 1 m/s for the wind measurement error, the error on the derived current variation is reported in Fig. 4.9. From the figure, it is immediate to note that:

- similar results are obtained in L-band and X-band;
- the error is higher when the reference depth is lower and larger depth variations are considered.

This is not an unexpected result because when the reference depth is lower, and larger depth variations are considered, actually a larger current velocity variation is established. Due to the linearity of the selected kernel, the error affecting current variations must necessarily be proportional to the considered current variations. For 1 m/s wind velocity error, the current

variation error is proportional to the current variation through a factor that is about 0.55. More in general, the relation between current variation and current variation error can be written as

$$\sigma_{\Delta u}(x) = C_{wind}(u_{wind})\Delta u(x) \quad (4.16)$$

where C_{wind} is a coefficient depending on wind speed error. Actually, if the coefficient is evaluated as a function of wind speed measurement errors, a linear behaviour can be clearly recognized. This means that the following relation can be derived for the uncertainty of current variation

$$\sigma_{\Delta u}(x) \cong 0.55\sigma_{wind}\Delta u(x) \quad (4.17)$$

where σ_{wind} is wind speed error.

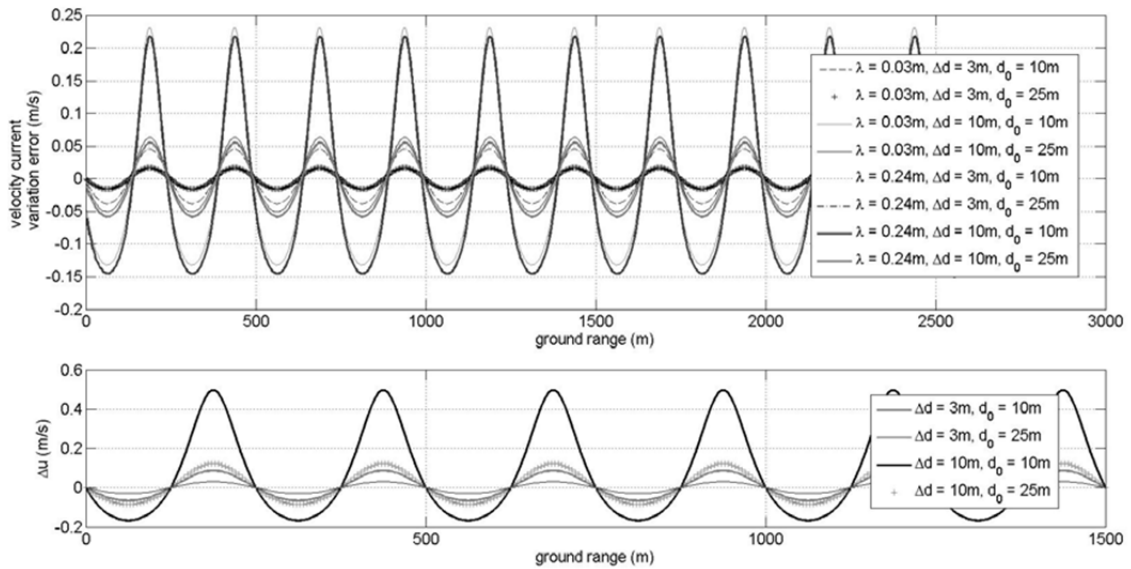


Fig. 4.9 Effect of 1 m/s wind velocity error on the estimated current velocity variations (*top*) for the simulated current velocity variations (*bottom*) [80].

The bathymetric uncertainty is a function of the considered bathymetric profile (d_0 , Δd) and of the unperturbed or reference current velocity (u_0). It also depends on the uncertainties in d_0 , u_0 , and Δu . The same bathymetric profiles as in the previous subsection are considered herein, i.e. $d_0 = (10 \text{ m}, 25 \text{ m})$, $\Delta d = (3 \text{ m}, 10\text{m})$, along with 0.5 m/s unperturbed current velocity. The uncertainties introduced in section 4.1 are also considered, together with 0.5 m/s wind speed error. Figure 4.10 shows the different contributions to the depth error. As expected, the errors are sensitive to current velocity variations. In more detail, the error due to the reference depth

uncertainty oscillates around the reference depth uncertainty and is equal to the latter one when current velocity variation is zero. The error due to unperturbed current velocity uncertainty is in general quite low, the only exception being the zones where current variation is maximum. Finally, the error due to wind uncertainty represents the highest contribution to the depth error. Again, quite low depth errors are achieved when current variations are not so strong, that is the range of bathymetric variation is small ($\Delta d = 3$ m). Significant errors are instead obtained when larger bathymetric variations ($\Delta d = 10$ m) are considered.

Figure 4.11 reports the overall depth uncertainty. The minimum error is equal to the error in the reference depth. In general, low depth errors are obtained for both low and high reference depths when the range of bathymetric variations is limited. The worst case for bathymetric reconstruction is when the variation of depth is of the same order of the reference depth. In this case, depth errors larger than 1.5 meters can be experienced.

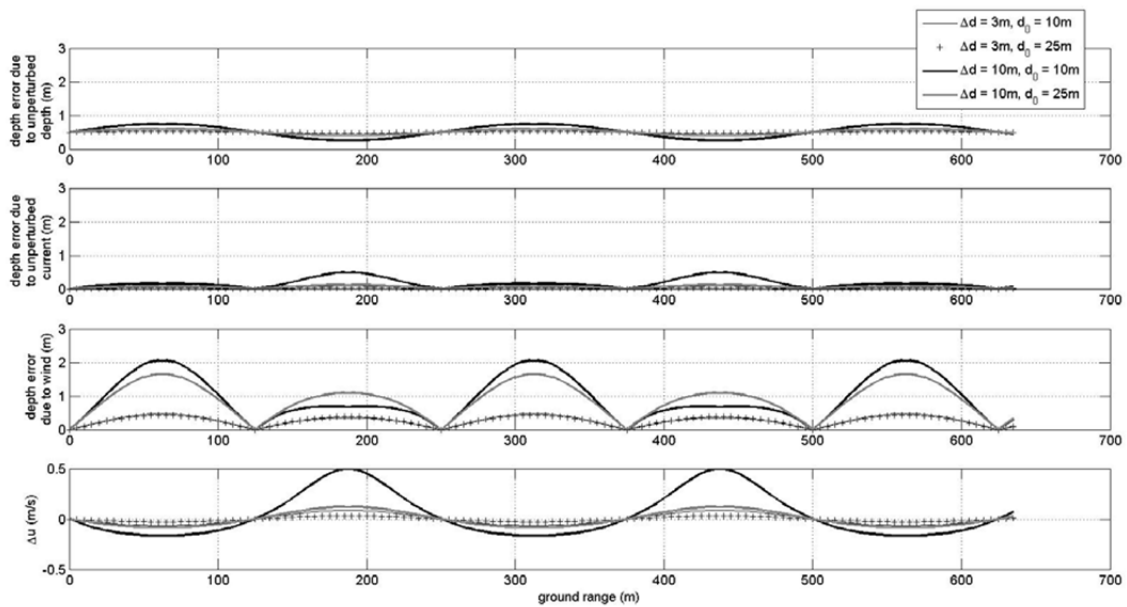


Fig. 4.10 Different contributions to depth uncertainties (*top, top center, bottom center*) corresponding to the simulated current velocity variation (*bottom*) [80].

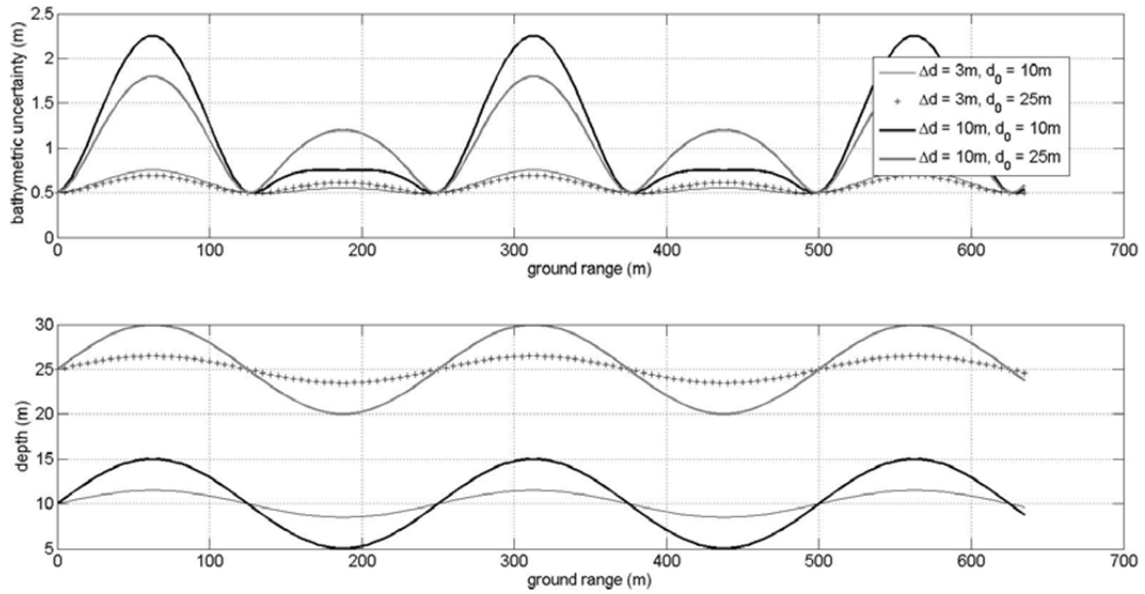


Fig. 4.11 Overall depth uncertainty (*top*) corresponding to the simulated bathymetry (*bottom*) [80].

4.2.2 SAR based products derived from CBA

The CBA relies on the inversion of SAR image, from image intensity to sea surface current velocity variations and then on the derivation of depth measurements. The first step is based on the linear kernel of VSE, whereas the second step is the solution of the continuity equation. Bragg scattering is assumed as the main scattering mechanism so the results of the inversion of the linear kernel of VSE are only sensitive to the variations of the current component directed along the ground-range direction. Azimuth-current components do not influence the output of the inversion process.

As a results, the output of SAR image inversion is the current field along the ground range dimension: one ground-range surface current profile can be derived for each azimuth line, and thus exploited to derive ground-range bathymetric profiles. The distance between two points of a given ground-range profile is set by the pixel spacing of the exploited SAR product and hence is limited by ground-range resolution. The same consideration applies to the distance between two different ground-range profiles, that is defined by the azimuth pixel spacing.

The overall output of the selected CBA can be therefore represented as a distribution of depth measurements that can be considered uniform, both in range and in azimuth, with density regulated by image resolutions.

However, the capability to derive a depth map in which each point corresponds to one image pixel does not mean that it is possible to recognize any feature characterized by size equal or larger than the resolution. This is because, as in WBA, also in CBA the bathymetry is sensed indirectly. Since in CBA the bathymetry is sensed through sea-current variations, only the bathymetric features that are able to produce proper and significant current variations can be detected. Specifically, the selected CBA is only sensitive to ground range current variations and, therefore,

- (1) if the current is mainly directed along the azimuth direction, the bathymetry cannot be retrieved by this method;
- (2) equivalently, no bathymetric feature can be observed when the bathymetric changes mainly along the azimuth direction.

When the main current component is along the ground range direction, the main results of the performed error budget analysis hold:

- (1) Bathymetric features with a ground-range depth profile characterized by a scale length that is significantly larger than the ground-range resolution can be detected. Concerning this, it is essentially to remark that the detection is based on image intensity modulations. Several image pixels are needed to individuate such a kind of image modulations. Therefore, it is reasonable to state that ground range depth profile with a scale length from 5 to 10 times larger than the ground range resolution can be detected by the selected CBA.
- (2) The depth uncertainty is a function of the shape of the observed profile. Concerning this, the error-budget analysis showed that, in the considered worst case, the depth uncertainty is of the order of 20% of the vertical excursion of the feature (i.e. 1m for 5m vertical variation). In addition, the method is able to derive with better accuracy the bathymetric features characterized by an increased depth (e.g. depression or subsidence) with respect to the background and not “bulge-like” features.
- (3) The range of depths that can be measured by the selected CBA is limited by the velocity of the unperturbed current. If the unperturbed current velocity is low, according to the continuity equation, the current variations due the bathymetry are also low thus leading to small amplitude variations that cannot be observed in the resulting SAR image because they are masked by SAR image noise. Hence maximum detectable depth is not expected to exceed 30 m. The minimum detectable depth can be set to around 5 m because lower depths in coastal areas typically correspond to slower currents and current variations that cannot be detected by the considered technique.

4.2.3 Specifications and requirements - CBA

According to the performed analysis, the following specifications and requirements can be formulated:

- 1) Even if the specific depth range depends also on sea state conditions, it is reasonable to assume that SAR bathymetry can be performed when the depth of the area of interest is in the range [5; 50] m [35], [50], [84].
- 2) Sharp depth variations cannot be detected because the indirect process through which SAR is able to sense bathymetry filters them out. CBA shall be able to retrieve bathymetric measurements over features characterized by a scale length from 5 to 10 times, at least, larger than image resolution.
- 3) CBA shall be used to retrieve bathymetric measurements when sea surface current velocity is equal or above 0.5 m/s and a significant component of this current is along the ground-range direction.
- 4) A specific range of wind velocities is needed to produce the intensity modulations that can be detected from the resulting images. In detail, Bragg scattering is possible when the wind speed is above the threshold for the generation of short waves, i.e. above 3 m/s [41]. However, with specific reference to the considered bathymetric model, the wind speed has to be also below 8 m/s because for larger values the surface roughness generated by the wind can be so intense to mask completely the intensity modulations due to bathymetry [35]. Hence, the optimum wind range to use the simplified model is from 3 to 6 m/s.
- 5) CBA shall be used to retrieve bathymetric measurements when no swell waves characterize the state of sea surface, otherwise SAR intensity modulations due to the swell waves can be interpreted as bathymetric variations by CBA.
- 6) Since the sea surface backscatter at all common SAR frequencies decreases quite sharply for increasing incidence angles from 20° to 50°, values of the incidence angle of SAR images should be as short as possible. In this way, slant range reduces and, therefore, backscattering from sea surface increases and undesirable smearing effects decrease [90]. Incidence angles larger than 40° should not be used for SAR bathymetry based on CBA.
- 7) Amplitude-only data can be used since current modulations are detected as amplitude modulations. With specific reference to COSMO-SkyMed standard processing levels

[83], Level 1B Products or Detected Ground Multi-look (MDG) products represent the best choice to be used as an input to the method.

- 8) Vertical polarization returns are higher than the ones obtained with horizontal polarization by several dB except at the steepest incidence angles ($< 20^\circ$), whereas the backscatter from cross-polarization data is usually uniformly 5 dB lower than the horizontal one. As a consequence, vertical polarization seems better in order to enhance sea surface returns; anyway it was observed that contrast and modulations due to bathymetry in horizontal polarization are larger than in vertical one, even if the effect is small.
- 9) L-band imagery is more suited for CBA than C- or X-band because the latter are more influenced by the atmospheric effects (e.g. winds) and these effects can be, in general, modelled less accurately. In addition, the selected modelling approach based on Bragg scattering properly applies only to L-band. The application to higher frequencies is possible, but degraded performance can be expected.
- 10) CBA should be applied to medium resolution, i.e. stripmap, SAR products. This is because the relevant resolution is good to image bathymetric features but is also able to filter out additional sea surface effects (e.g. waves) that are not typically modelled by CBA.
- 11) A vector measurement (i.e. both amplitude and direction) of wind velocity is needed to generate an estimate of the relaxation rate. Wind velocity must be provided in the same reference frame in which SAR data are delivered (e.g. WGS84 when Level 1B COSMO-SkyMed [83] data are considered). Wind velocity must be also completed with the height above sea surface where the velocity is measured. According to the performed error budget analysis, the expected accuracy of the measurement is 0.5 m/s for the ground range component of wind velocity.
- 12) At least one vector measurement (i.e. both amplitude and direction) of current velocity at a given location within the area of interest is needed to solve the continuity equation. The current measurement must be provided in the same reference frame in which SAR data are delivered. According to the performed error budget analysis, the expected accuracy of the measurement is 0.1 m/s for the ground range of component of the reference current.
- 13) The depth of the location where current velocity is measured is needed to solve the continuity equation. According to the performed error budget analysis, the required reference depth accuracy is 0.5 m.

Under particularly favorable circumstances, such as strong current, uniform wind fields, and absence of long waves, bathymetric features are clearly imaged [37], [84]. These clear features can be thus enhanced by standard image processing tools [73] and processed to estimate the local depth [37], [73], [84]. These conditions are actually very rare [50] and limited to regions, such as the North Sea, where currents, generated by tidal effects, are extremely intense, that is stronger than 1 m/s. Therefore, applicability of this approach to close areas, e.g. gulfs or inlets, or relative close seas, e.g. the Mediterranean Sea, is very limited because current velocity is too slow or tends to be irregular both in time and in intensity [7]. For these reasons, the current-based approach has been not further considered in the present work and the wave-based method has been preferred for bathymetric data retrieval.

Chapter 5

WBA Application to SAR Image

The present chapter focuses on the Wave-Based Approach because the particularly favorable circumstances for application of the Current-Based Approach are limited in the area of the Gulf of Naples, Italy, that is the area of interest of the performed work. Therefore, the WBA application methodology to SAR image and the involved parameters are presented. The proposed WBA algorithm is described and discussed.

5.1 WBA application methodology and involved parameters

When the conditions for linear imaging are satisfied [32], [59] the Wave-Based Approach can be considered a promising bathymetric technique for characteristic regions of the Mediterranean Sea, such as in gulfs and relatively close areas, where currents are extremely weak and cannot be used to infer bathymetry.

Based on the assumption of linear SAR imaging of sea surface, swell waves can be tracked from offshore up to the shoreline and swell refraction and shoaling in coastal areas can be investigated from SAR image using spectral analysis [36], [41], [42]. Fig. 5.1 depicts the main steps to be performed for L and T retrieval and for sea water estimation according to the available literature. The Fast Fourier Transform (FFT) of image intensity is applied to a small region of the SAR image. A two-dimensional image spectrum is retrieved in order to convert it into the directional wave spectrum of the local wave field. The resulting peak in the 2-D spectrum marks the dominant swell wavelength and the dominant swell direction of propagation in the considered portion of the SAR image. Specifically, values of wavelength and angle of propagation can be retrieved by using the following formulas [32], [39]

$$L = \frac{2\pi}{\sqrt{k_x^2 + k_y^2}} \quad (5.1)$$

$$\varphi = \tan^{-1}\left(\frac{k_y}{k_x}\right) \quad (5.2)$$

where

- L is the peak wavelength;
- φ is the peak wave direction with respect to the image;
- k_x and k_y are the peak coordinates in the frequency space.

It is worth noting that the wavelength of wind sea is usually too short to be imaged by SAR and wavelengths between about 80 and 300 m are often filtered to remove wind streaks (structures on the sea surface of the image produced by airflow turbulent eddies at the boundary layer) and wind sea patterns from the spectra. Hence, investigation of swell shoaling and refraction can be performed by scanning the region of interest with a small window and by executing the spectral analysis at each location within this small window. The retrieved swell direction of propagation has an ambiguity of 180° due to the static nature of SAR image. However, in coastal area this ambiguity problem can be solved by observing the SAR image and considering that swell waves propagate towards the coast [32].

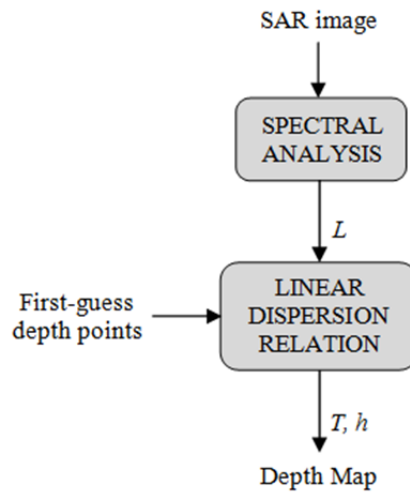


Fig. 5.1 The main steps of swell-based bathymetry according to the available literature [32], [36], [39].

Two different scanning techniques can be used. According to [32] and [39], a scanning window is moved along the swell propagation direction by a distance equal to the retrieved swell wavelength and a new FFT is computed. Alternatively, a raster approach can be used by moving a scanning window along the image axes, as shown in Fig. 5.2. The scanning window is moved by a predetermined distance, or sampling step, along the range and azimuth directions, starting from offshore and until the shoreline. In this way, values of swell wavelength and direction of propagation are calculated over a regular grid throughout the area of interest. Specifically, the windows can be considered adjacent to each other along each side or they can be positioned at a predetermined distance (or number of pixels) from each other according to the requirement.

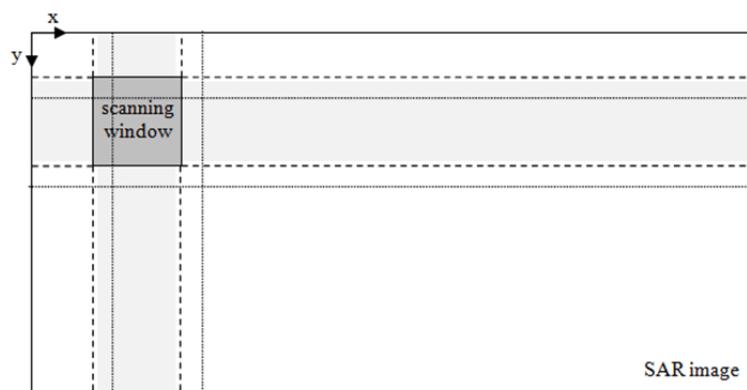


Fig. 5.2 Illustration of the raster scanning approach.

Concerning swell period, it is well known that the period cannot be directly retrieved from a single SAR image [32], [39], [91]. The wave period could be measured from a temporal sequence of radar images [38], but this sequence is not typically delivered in satellite remote sensing application. If external sources, such as buoys or weather services are not available, the

wave period can be measured by the dispersion relation starting from the knowledge of local depth in one or a few locations within the area of interest [39]. In detail, swell period is evaluated offshore by eq. 4.3 using trial values of T and by comparing the obtained value with the actual water depth reported on available low-resolution topographic datasets, e.g. nautical maps. In general, such a kind of first-guess approach is of limited accuracy. However, an important property of the dispersion relation can be exploited. As shown in Fig. 4.1, when the wave period is sufficiently long and local depth quite small, the sensitivity of the depth to the wave period is very low and therefore high uncertainties on the wave period and wave period variations can be tolerated. The first-guess approach is typically applied as close as possible to the intermediate water depth area [32], [39], in order to further reduce potential water depth errors.

Finally, the values of L and T retrieved over the investigated area are used to estimate sea water depth according to eq. 4.3. In this way, a dense and regular distribution of depth measurements is obtained and a bathymetric map can be generated.

5.2 The developed Wave-Based Algorithm for bathymetry retrieval

The oversimplified algorithm presented in section 5.1 assumes that swell waves are perfectly imaged by SAR without any source of perturbation. It is therefore called theory-driven algorithm in what follows. Indeed, the validity of the linear imaging model does not guarantee the reliability of the theory-driven algorithm. Even if, from a global point of view, swell waves are correctly imaged and dominate SAR data, additional phenomena occur locally, including speckle, noise, and other sources of perturbation. Local estimation and tracking of swell by the theory-driven algorithm is thus extremely unstable and in general not robust. For this reason, the algorithm must be completed by further processing steps and procedures [89].

First of all, it is important to select SAR images of sea surface in agreement with the specifications and requirements described in section 4.1.4 [92]. When the best SAR images are selected, it is essential to select sub-portions of the images in which swell waves are present since the method cannot run over sea pixels not dominated by swell waves. Those areas can be individuated by a visual inspection of the SAR image since swell waves are imaged by SAR as long, regular, and bright-and-dark alternating stripes [92]. Behaviour of swell waves in the selected areas should be influenced by bathymetry, i.e. coastal regions or any region where

bathymetry is not suspected to be very deep. The method cannot run over land pixels and, therefore, land must be masked out. It is also desirable for the visual inspection to be able to clearly recognize that some peculiarities of the wave shoaling and refraction are occurring over the selected sub-portion [92]. In this way, it is extremely likely that the wavelength estimation and so the local depth determination performed by the method will be successful.

When the sub-portions of SAR image are selected, the proposed methodology shown in Fig. 5.3 should be implemented. It is based on the introduction of a preprocessing step before spectral analysis and a smoothing step after spectral estimation. Finally, the algorithm is completed by precise requirements and limitations posed to the outcomes of the frequency analysis. Figure 5.4 provides a more detailed overview of the several steps constituting the proposed data processing algorithm for swell-based bathymetry.

Preprocessing is in charge of filtering out phenomena occurring at a smaller scale with respect to bathymetry. This is performed by resizing the original spatial resolution of SAR data, i.e. introducing a scaling factor. Standard bilinear interpolation is used to resize the image. The specific value of the scaling factor depends on the value of the original spatial resolution and should be set in order to reduce the noise without removing swell waves features on the SAR image. Thereafter, a two-dimensional median filter is applied on the resized image. The filter replaces the amplitude value of the resized SAR image pixels by the median value in a neighbourhood around of any given pixel. Again, the kernel size of the median filter must be set to reduce the residual noise while preserving the image modulations generated by swell waves.

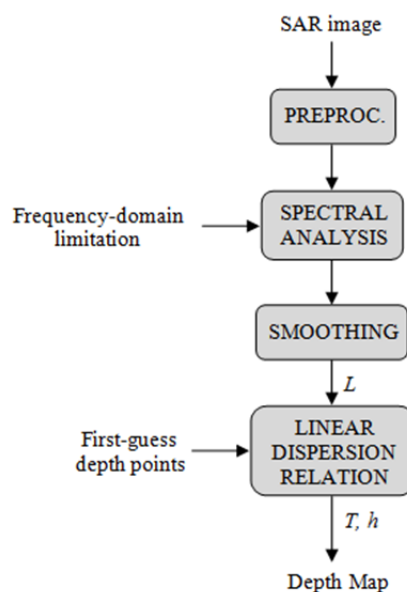


Fig. 5.3 The proposed algorithm for swell-based bathymetry.

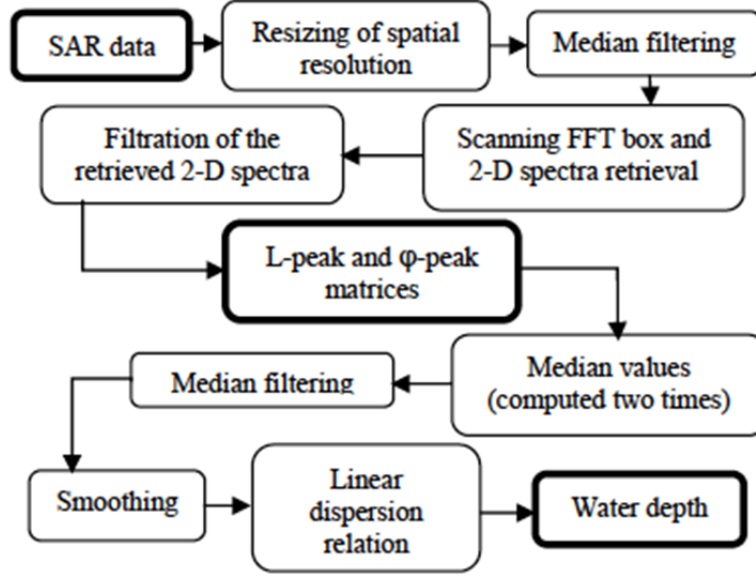


Fig. 5.4 The detailed flowchart of the proposed data processing algorithm for swell-based bathymetry [89].

At this point, spectral analysis can be performed using the raster scanning approach (see Fig. 5.2) and the FFT method to obtain the values of peak wavelength and peak wave direction along each track. However, when the spectrum is computed in a relatively small box, at a given location over the image, not a single, dominant, peak is found, but several peaks appear (see Fig. 5.5). In order to select the right peak, i.e. the peak corresponding to swell waves to track, frequency-domain limitations are required. For this reason, the algorithm introduces a region of interest in the domain of the spectrum. The region of interest is a portion of a circular corona. Upper and lower boundaries of the corona guarantee that the retrieved peak wavelength is within the assigned range of typical swell wavelength, that is

$$L_{\min} \leq \frac{1}{\sqrt{f_x^2 + f_y^2}} \leq L_{\max} \quad (5.3)$$

where L_{\min} and L_{\max} are the minimum and maximum expected wavelength and f_x, f_y are the spatial frequencies associated to the spectrum. The angular extent of the region can be instead defined introducing a range of admissible angles of propagation

$$\varphi_{\min} \leq \varphi \leq \varphi_{\max} \quad \varphi = \tan^{-1} \frac{f_y}{f_x} \quad (5.4)$$

The range of admissible angles, as well as the range of expected wavelengths, can be easily set looking at the SAR image. The last limitation to the spectrum analysis is the introduction of a maximum admissible deviation, $\Delta\varphi$, of the propagation angle between two consecutive

locations of the FFT box. This is useful to maintain the tracking of the main swell field and to avoid switching to wrong wave systems.

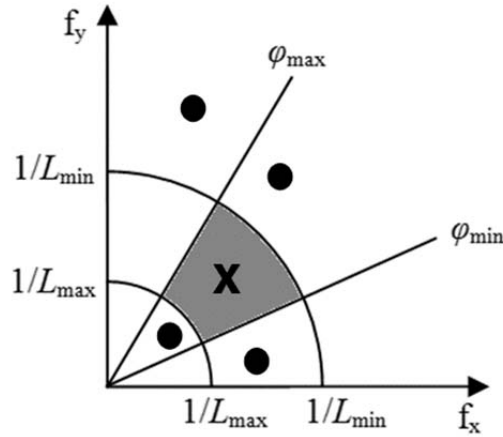


Fig. 5.5 As result of the spectral analysis performed on a given small box, several peaks are obtained (marked with dots and cross on the image). Frequency-domain limitations on the (f_x, f_y) plane are set by the identified ranges of admissible swell wavelength $([L_{min}; L_{max}])$ and angle of propagation $([\varphi_{min}; \varphi_{max}])$. Only the peak included in the so defined region of interest (i.e. gray area on the image) is considered (marked with a cross on the image) by the algorithm to perform wavelength and period estimation.

After completion of spectral analysis, two matrices containing the values of the dominant swell wavelength and dominant direction of propagation throughout the SAR image are obtained. A smoothing step is in charge of increasing the stability of the obtained results. This is achieved through a two-dimensional median filter processing the matrixes of wavelength and angle of propagation resulting from the spectral analysis. In addition, a moving average filter is applied along each row of the two obtained matrixes.

At this point, the first guess approach for wave period estimation can be applied and sea water depth can be derived by applying eq. 4.3 for each location of the scanning window.

Overall, eleven parameters must be set to run the proposed algorithm: two parameters refer to the preprocessing steps (scaling factor and kernel size for median filter on the SAR image); two parameters define the raster scanning (i.e. FFT window size and sampling step); five parameters are required to introduce limitations to the output of the spectral analysis (i.e. maximum and minimum wavelengths and propagation angles, and maximum admissible deviation between consecutive boxes); and two parameters are used by the final smoothing step (kernel size of the median filter and span of the moving average filter). Most of these tuning parameters can be set from visual image inspection.

Chapter 6

Experimental Results

The present chapter shows the main experimental results that have been obtained with the Wave-Based Approach and the proposed WBA algorithm. The data set provided by the Italian Space Agency in the framework of the SAR4BAT project is presented and the selection process of SAR images is described, both for L-band ALOS PALSAR images and X-band COSMO-SkyMed SAR images. Tracking of swell wave shoaling and refraction phenomena is shown. Finally, Digital Elevation Models of seabed in the Gulf of Naples, Italy, are retrieved and correlation analysis with the official nautical charts provided by the Italian Navy Hydrographic Institute is performed.

6.1 Italian Space Agency's SAR4BAT project

The SAR4BAT project (Synthetic Aperture Radar data fusion for bathymetric retrieval of seabed in coastal areas and archaeological areas) is founded by the Italian Space Agency (ASI) in the framework of a call reserved to Small/Medium Enterprises (SMEs) and dealing with Earth observation [93]. The project goal is the development of a system that, starting from Earth Observation data, produces bathymetric maps of seabed and of maps of possible underwater archaeological sites in the Gulf of Naples, Italy. SAR data from ALOS and COSMO-SkyMed satellites have been provided by ASI to test the system. Data fusion with optical data has also to be investigated. Data distribution shall be based on a WebGIS, making use of public background maps to easily locate the generated maps.

Figure 6.1 shows the companies and teams involved in the SAR4BAT project. Kell srl, an Italian software development SME located in Rome and Arezzo, Italy. Since 1997 it has operated in software and TLC integration employing ground and satellite networks, in particular for Telemedicine, satellite and airborne remote sensing. The main partner of the project is LitCom, a company founded a few years ago and based in Lacco Ameno (Ischia Island). Its mission is customer support for technical documentation management, ensuring both on-site and remote support. The Aerospace Systems group of the Department of Industrial Engineering (DII) of the University of Naples "Federico II" is also part of the SAR4BAT team. The contribution of DII to SAR4BAT deals with SAR-based algorithm selection, implementation and demonstration.

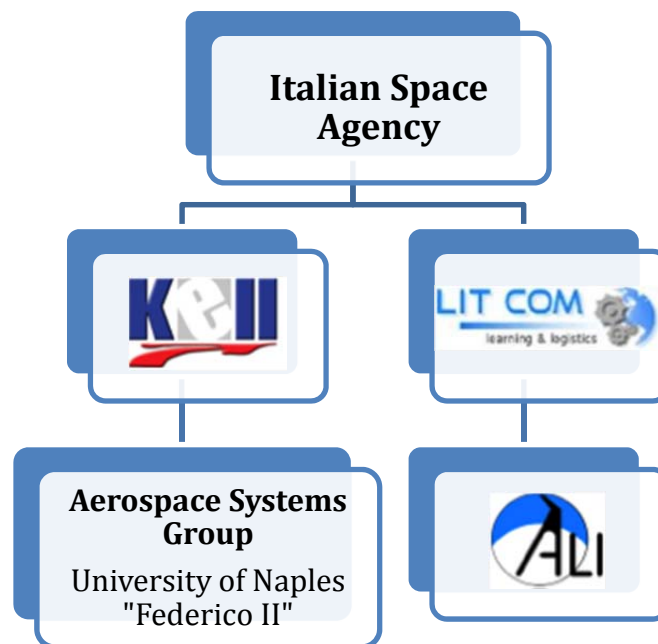


Fig. 6.1 Companies and teams involved in the Italian Space Agency's SAR4BAT project.

6.2 Data set

The data set, made available by ASI in the framework of SAR4BAT project, for algorithm definition and validation, is represented by:

- 5 ALOS PALSAR images, L-band, HH polarization, Stripmap mode, Level 1.5 product (i.e. a multi-look image in ground range and azimuth coordinates [88]), acquired during the ascending pass of the satellite at about 9:30 pm and with right looking side, 6.25 m x 6.25 m pixel spacing, 38.7° incidence angle at the centre of the scene;
- 6 COSMO-SkyMed SAR images, X-band, HH polarization acquired with right looking side, both in Stripmap mode, 2.5 m x 2.5 m pixel spacing, and in Spotlight mode, 0.5 m x 0.5 m pixel spacing [83].

All the images cover the area of the Gulf of Naples, Italy, since it is the area of main interest for the SAR4BAT project.

The data set includes both archive data and some new acquisitions. In both cases, the images were selected in order to maximize the probability of observing swell waves. This was done by checking the meteorological data for the former days with respect to the acquisition time in an area that is larger than the Gulf of Naples and includes most of the Tyrrhenian Sea. This is because swell waves are not generated in loco but travel far from their regions of origin.

6.2.1 ALOS PALSAR images

The 5 ALOS PALSAR images reported in Tab. 6.1 has been provided by ASI in the framework of the SAR4BAT project. A numeration has been adopted to refer to each image.

N°	Scene ID	Sensor/Mode	Acquired	Wind Speed (WS) (m/s)*	WS day before (m/s)*	WS day after (m/s)*
1	ALPSRP056280800	PALSAR FSB	13/02/2007	6.7 / 9.8 / 20.5	2.5 / 8.2 / 14.4	1.7 / 3.6 / NA
2	ALPSRP109960800	PALSAR FSB	16/02/2008	4.2 / 6.7 / 15	0.2 / 1.0 / NA	3.0 / 5.1 / 10.3
3	ALPSRP210610800	PALSAR FSB	06/01/2010	2.5 / 4.7 / 8.9	1.4 / 3.3 / 5	1.9 / 4.2 / 7.8
4	ALPSRP264290800	PALSAR FSB	09/01/2011	0.6 / 1.1 / NA	0.6 / 0.6 / NA	0.6 / 1.7 / NA
5	ALPSRP103250800	PALSAR FSB	01/01/2008	1.2 / 2.6 / NA	1.0 / 1.5 / NA	1.2 / 2.6 / NA

*(average value / maximum value / gust)

Tab. 6.1 Available ALOS PALSAR SAR images provided by ASI.

6.2.2 COSMO-SkyMed SAR images

The 6 COSMO-SkyMed SAR images reported in Tab. 6.2 has been provided by ASI in the framework of the SAR4BAT project. Additional details about the images are listed in Tab. 6.3. A numeration has been adopted to refer to each image.

N°	Scene ID	Sensor/Mode	Pass
1	EL20130109_510815_2513585.6.2	HIMAGE	Ascending
2	EL20130111_511370_2518037.6.2	HIMAGE	Descending
3	EL20121222_507597_2477243.6.2	EN-SPOTLIGHT	Descending
4	EL20130120_512956_2545081.6.2	EN-SPOTLIGHT	Ascending
5	EL20130210_514951_2630659.6.2	EN-SPOTLIGHT	Ascending
6	EL20130210_514951_2632986.6.2	EN-SPOTLIGHT	Descending

Tab. 6.2 Available COSMO-SkyMed SAR images provided by ASI.

N°	Acquired	Hour	Incidence angle	Wind Speed (m/s)*	WS day before (m/s)*	WS day after (m/s)*
1	27/02/2012	5:01	44.7-50.6	8.3/11.9/ 19.2	3.3/11.4/15.0	3.1/6.1/NA
2	25/12/2011	17:13	24.9-28.3	3.9/5.3/NA	2.2/3.1/ NA	NA
3	07/03/2009	17:18	35.2-35.9	2.2/5.0/NA	1.7/4.7/ NA	1.4/3.9/NA
4	20/01/2013	4:10	35.2-35.9	3.9/5.6/9.7	1.4/2.5/ NA	3.1/6.9/9.2
5	10/02/2013	4:52	NA	NA	NA	NA
6	10/02/2013	17:09	NA	NA	NA	NA

*(average value / maximum value / gust)

Tab. 6.3 Additional details about the COSMO-SkyMed SAR images.

6.3 Selection of SAR images

The SAR images provided by ASI and listed in Tabs. 6.1 - 6.3 have been preliminary inspected in the NEST (Next ESA SAR Toolbox) environment [94]. Visual inspection of the images in order to identify swell waves propagating along the ground range direction has been performed (see section 4.1.4). Moreover, the following nautical and bathymetric charts provided by the Italian Navy Hydrographic Institute have been used to locate potential suitable areas for SAR-based bathymetric data retrieval (see section 4.1.4):

- "Golfo di Napoli" Nautical Chart [95], Navy Hydrographic Institute, number 127, edition 1/2004, Scale 1:60.000, Fig. 6.2;
- "Canali d'Ischia e Procida" Nautical Chart [96], Navy Hydrographic Institute, number 129, edition 2/2010, Scale 1:30.000;
- "Golfo di Pozzuoli" Bathymetric Chart [97], Navy Hydrographic Institute, number 1256, Scale 1:20000.

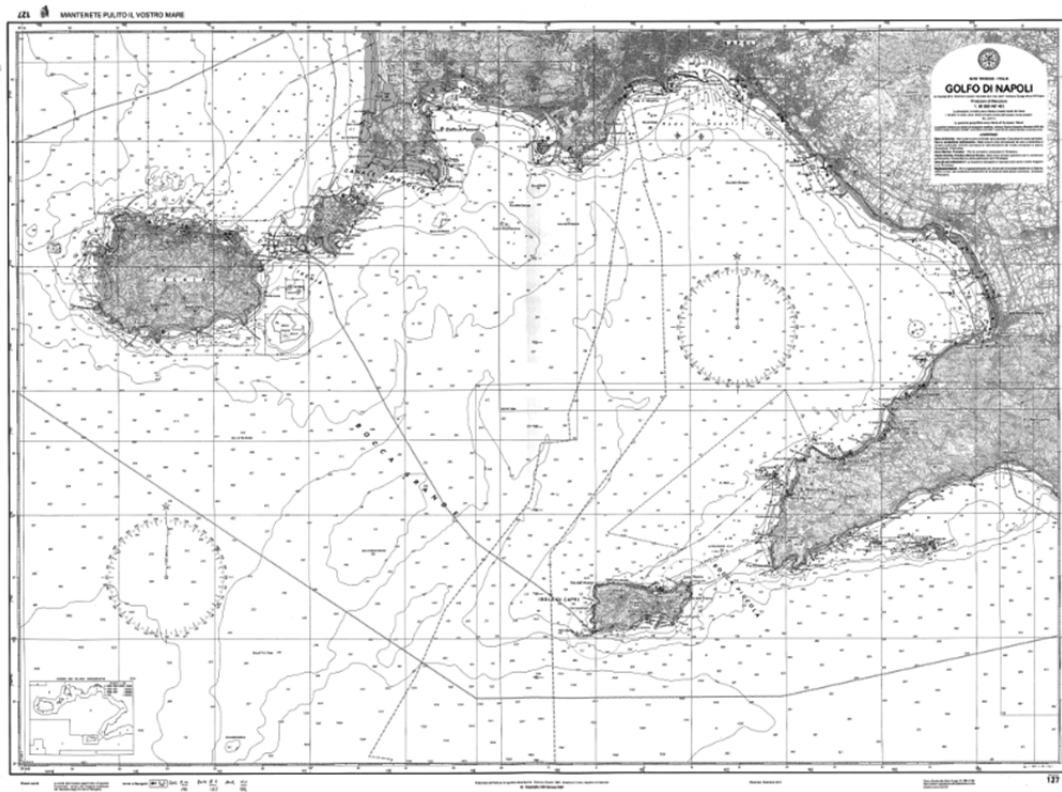


Fig. 6.2 "Golfo di Napoli" Nautical Chart [95], Navy Hydrographic Institute, number 127, edition 1/2004, Scale 1:60.000.

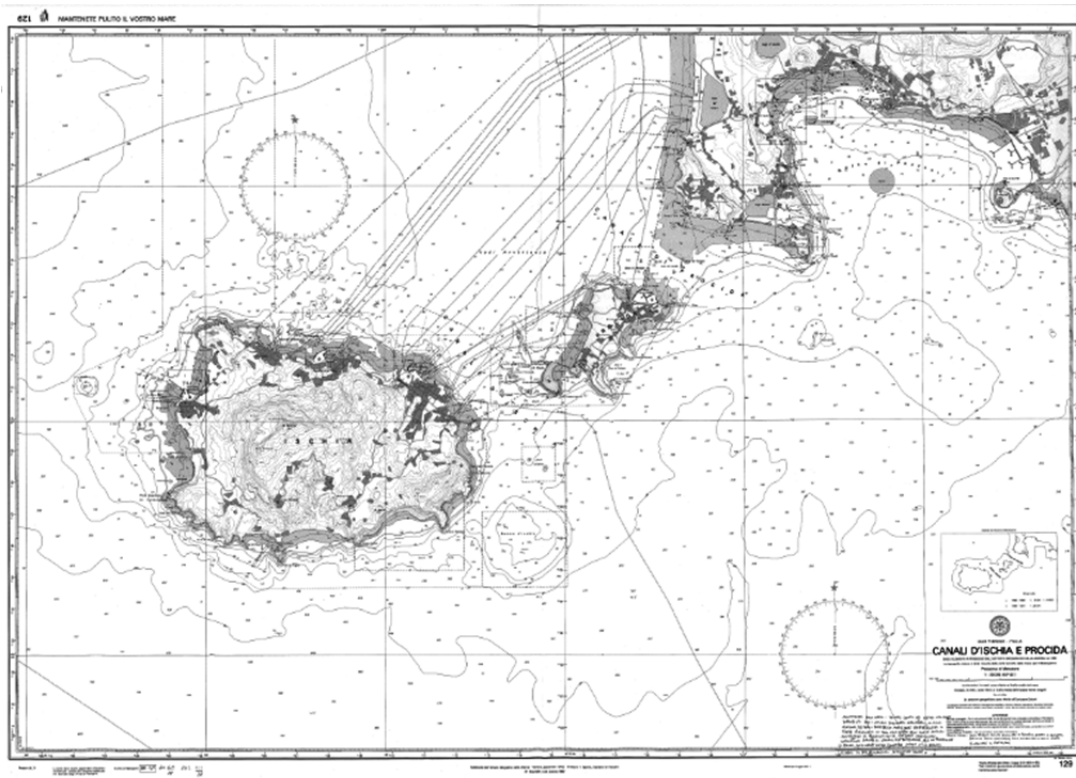


Fig. 6.3 "Canali d'Ischia e Procida" Nautical Chart [96], Navy Hydrographic Institute, number 129, edition 2/2010, Scale 1:30.000.

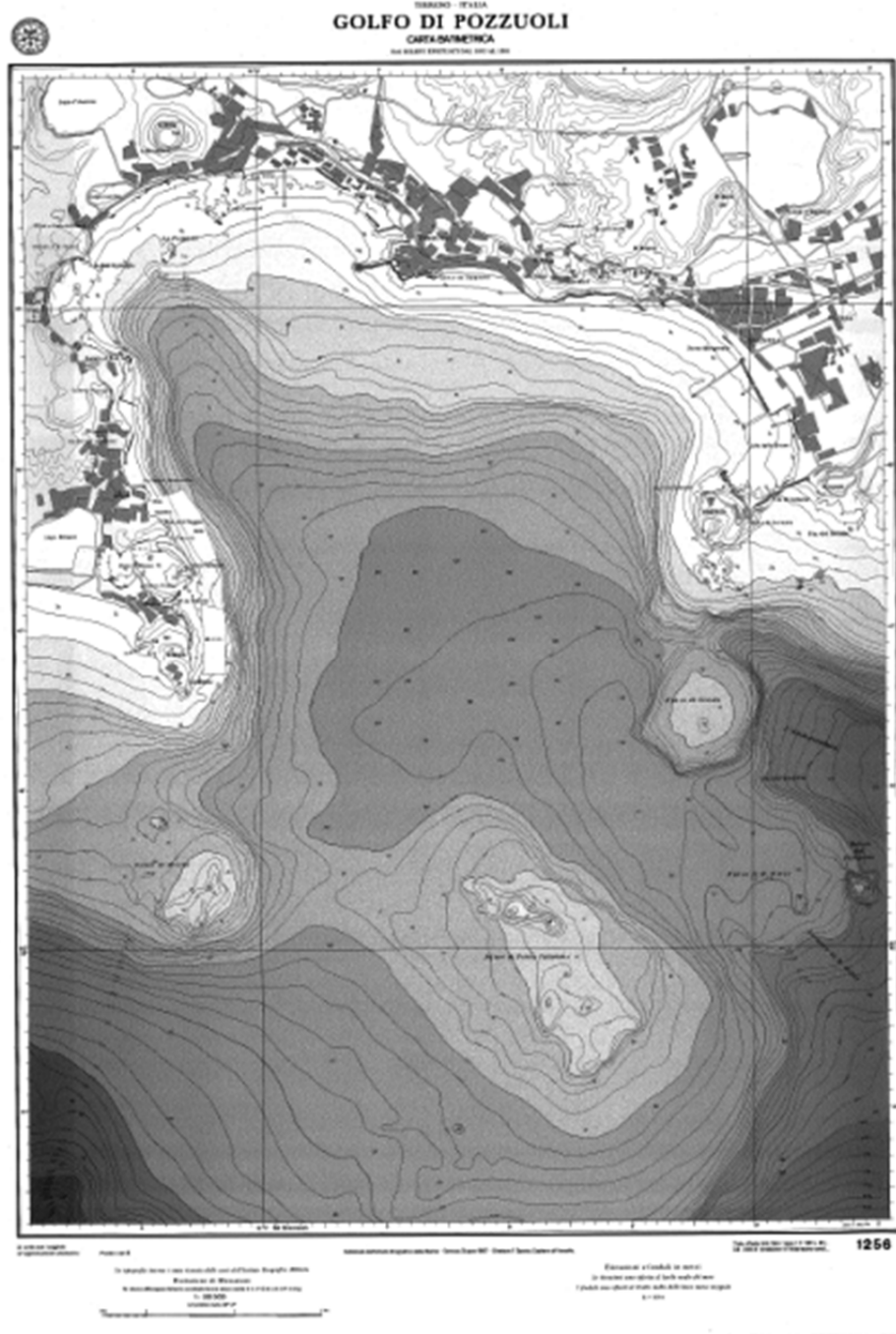


Fig. 6.4 "Golfo di Pozzuoli" Bathymetric Chart [97], Navy Hydrographic Institute, number 1256, Scale 1:20000.

6.3.1 Visual inspection of the ALOS PALSAR images

6.3.1.1 ALOS PALSAR image N° 1 (Scene ID: ALPSRP056280800)

The ALOS PALSAR image N° 1 (see Fig. 6.5) has been preliminary inspected and a wide swell field propagating on sea surface has been identified. As shown in Tab. 6.1, this can be attributed to the large value of wind speed the day before the SAR image acquisition (see section 2.1).

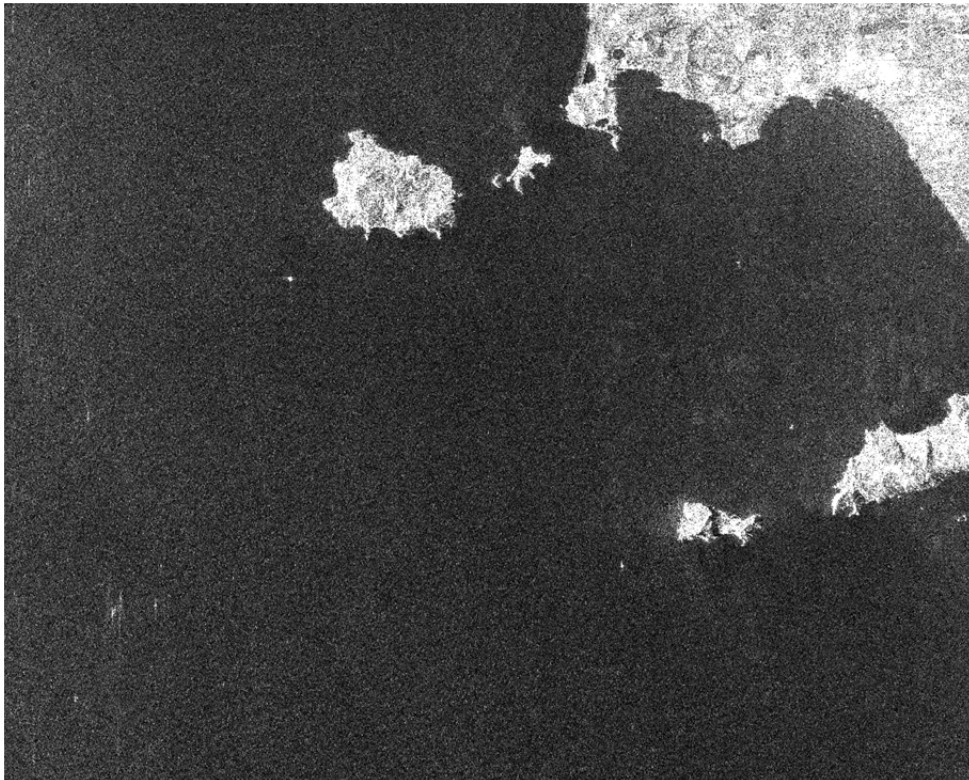


Fig. 6.5 ALOS PALSAR image N° 1 (Scene ID: ALPSRP056280800).

Phenomena of swell shoaling and refraction are clearly visible on several portions of sea surface throughout the SAR image. Figs. 6.6 - 6.7 show some examples along the south coast of the Ischia island and the northern part of the Gulf of Naples, respectively. In particular, the nautical charts [95], [96] reveal that the subset of the SAR image shown in Fig. 6.7 is particularly suitable for WBA application due to the gradually varying seafloor (see detail in Fig. 6.8). Indeed, values of sea water depth equal to 100 m are reported at 10 km from the coast, 50 m at 5 km from the coast and they gradually vary up to the shoreline. Not significant weather phenomena were present at the time of image acquisition, and the wind speed was about 3 m/s [98]. Moreover, Fig. 6.7 shows that swell waves propagate close to the ground range direction and swell crests tend to align themselves to the iso-depth lines of seabed.

As result of the performed preliminary visual inspection, the portion of the ALOS PALSAR image N° 1 related to the northern side of the Gulf of Naples has been selected for further analysis and for testing of the proposed wave-based algorithm for bathymetric data retrieval.

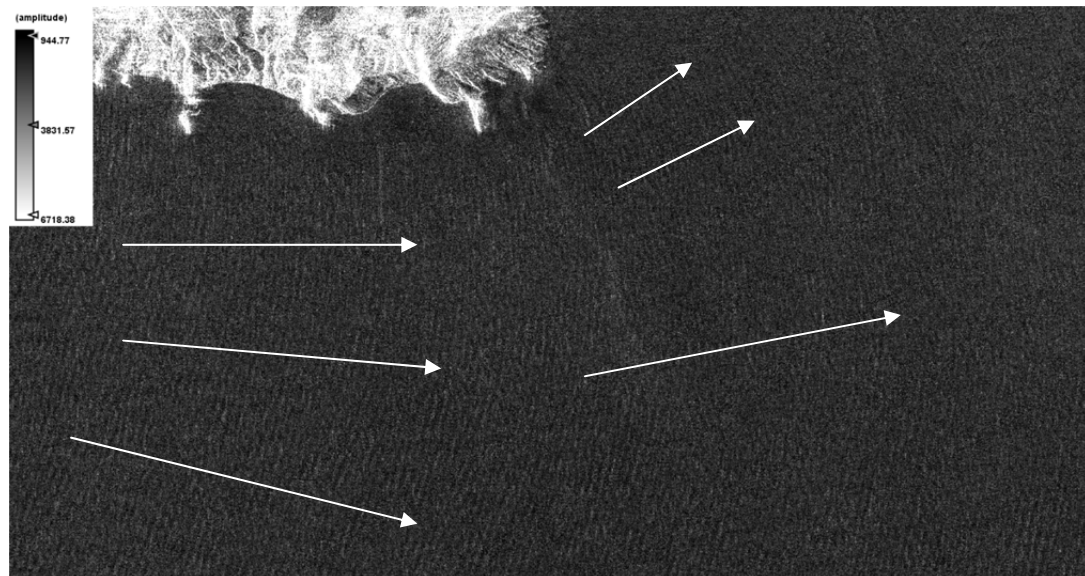


Fig. 6.6 Subset of the ALOS PALSAR image N° 1 (range of latitudes: [40.646°N, 40.706°N], range of longitudes: [13.851°E, 14.095°E]). Swell shoaling and refraction phenomena are clearly visible close to the south coast of the Ischia Island in the Gulf of Naples, Italy. The arrows show the direction of propagation of swell waves.

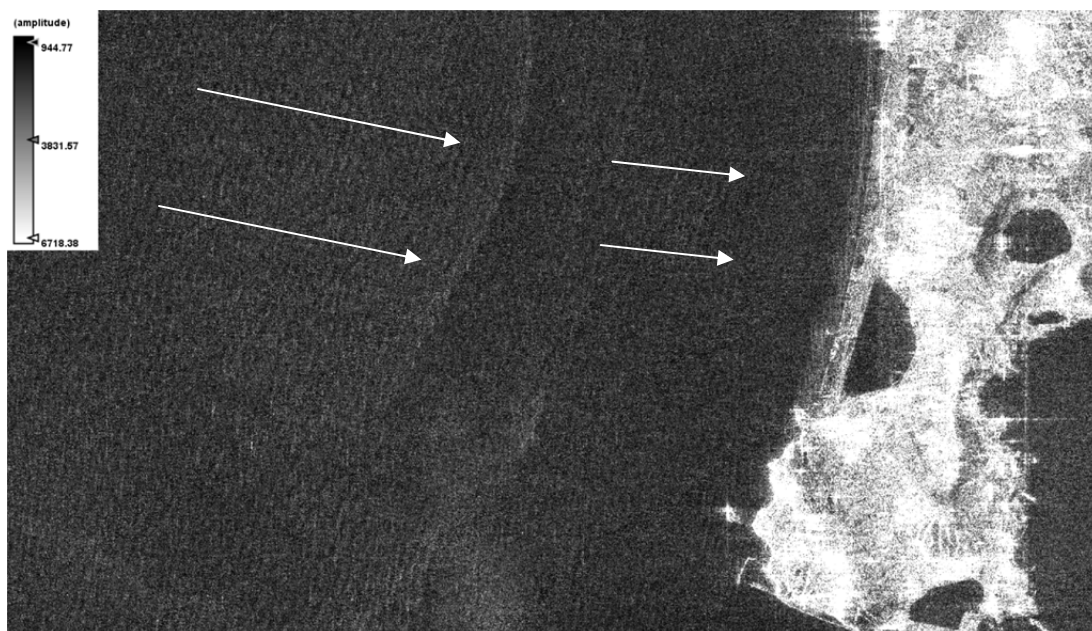


Fig. 6.7 Subset of the ALOS PALSAR image N° 1 (range of latitudes: [40.792°N, 40.843°N], range of longitudes: [13.908°E, 14.096°E]). Swell shoaling and refraction phenomena are clearly visible approaching the coast in the northern side of the Gulf of Naples, Italy. The arrows show the direction of propagation of swell waves.

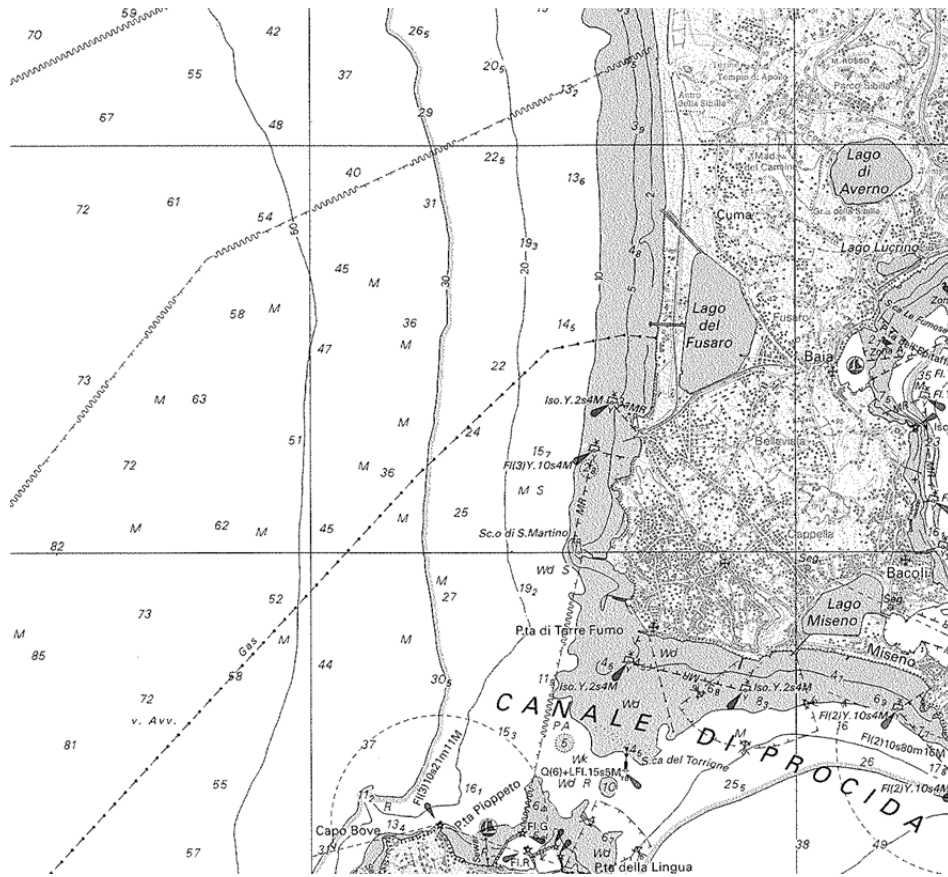


Fig. 6.8 Detail of the "Golfo di Napoli" Nautical Chart [95] related to the northern side of the Gulf of Naples, Italy.

6.3.1.2 ALOS PALSAR image N° 2 (Scene ID: ALPSRP109960800)

The ALOS PALSAR image N° 2 (see Fig. 6.9) has been preliminary inspected and no swell waves have been identified. The lack of swell waves can be due to the small values of wind speed during the day before the acquisition date, as reported in Tab. 6.1. On the contrary, sea surface is characterized by a wave field whose wavelength is higher than that typical of swell waves and it could be attributed to internal waves which are generally associated with high values of currents. The direction of propagation of this waves field is compatible with the typical direction of the current in the Gulf of Naples (the current usually enters into the so-called "Bocca Piccola", between Capri and the Coast of Sorrento, and exits from the so-called "Bocca Grande", between Capri and Ischia). Therefore, the ALOS PALSAR image N° 5 has been not selected for WBA application.



Fig. 6.9 ALOS PALSAR image N° 2 (Scene ID: ALPSRP109960800).

6.3.1.3 ALOS PALSAR image N° 3 (Scene ID: ALPSRP210610800)

The ALOS PALSAR image N° 3 (see Fig. 6.10) has been preliminary inspected and a very weak swell field has been identified. However, it is too weak and not enough visible for WBA application. Again, this can be attributed to the small values of wind speed during the day before the acquisition date, as reported in Tab. 6.1. Therefore, the ALOS PALSAR image N° 3 has been not selected for WBA application.

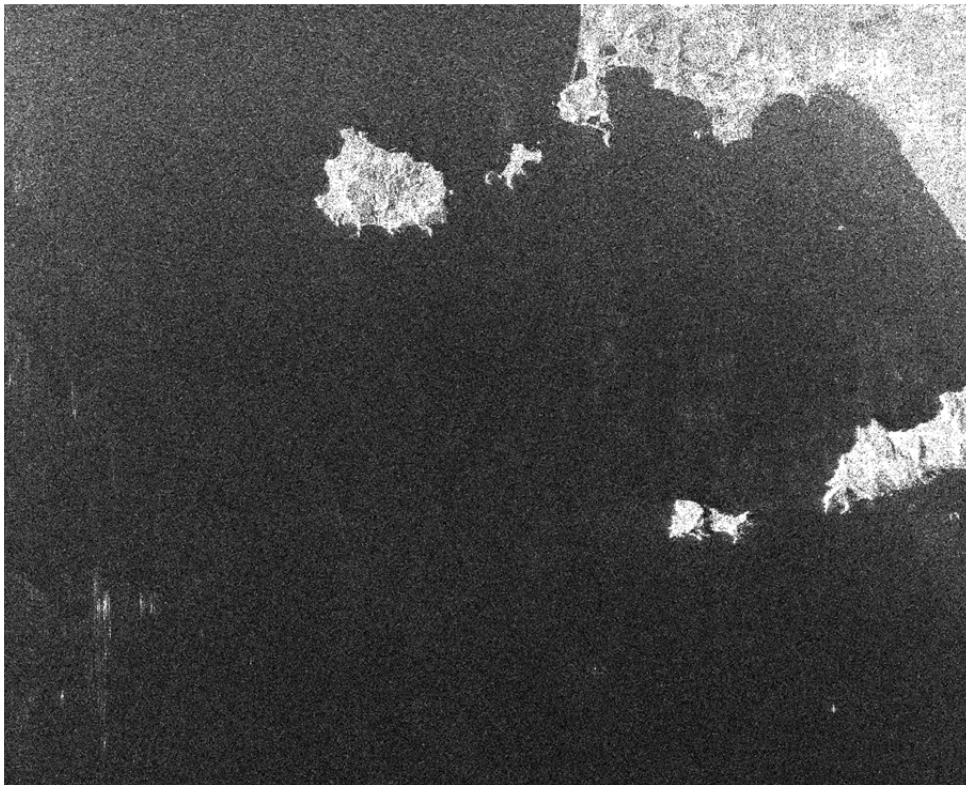


Fig. 6.10 ALOS PALSAR image N° 3 (Scene ID: ALPSRP210610800).

6.3.1.4 ALOS PALSAR image N° 4 (Scene ID: ALPSRP264290800)

The ALOS PALSAR image N° 4 (see Fig. 6.11) has been preliminary inspected and no swell waves have been identified. The lack of swell waves can be due to the small values of wind speed during the day before the acquisition date, as reported in Tab. 6.1. Instead, sea surface is characterized by some dark areas in proximity of the upper part of the islands. This can be due to a current travelling from south to north (which is compatible with the typical direction of the current in the Gulf of Naples) and to the mask effect of the islands. Therefore, the ALOS PALSAR image N° 4 has been not selected for WBA application.

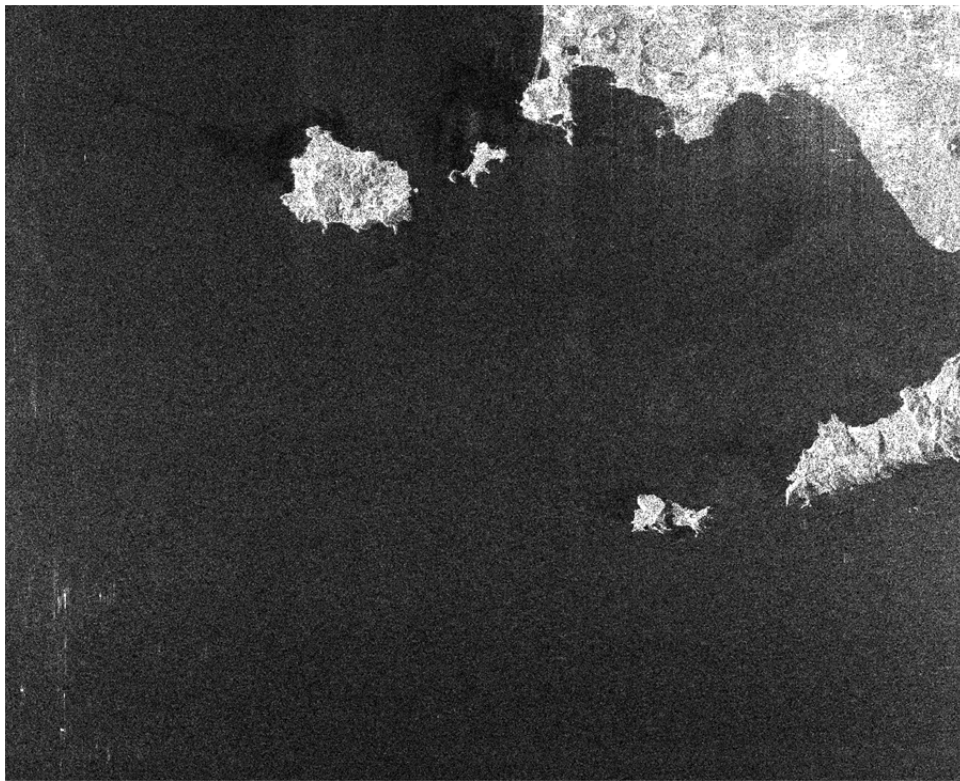


Fig. 6.11 ALOS PALSAR image N° 4 (Scene ID: ALPSRP264290800).

6.3.1.5 ALOS PALSAR image N° 5 (Scene ID: ALPSRP103250800)

The ALOS PALSAR image N° 5 (see Fig. 6.12) has been preliminary inspected and no swell waves have been identified. The lack of swell waves can be due to the small values of wind speed during the day before the acquisition date, as reported in Tab. 6.1. Therefore, the ALOS PALSAR image N° 5 has been not selected for WBA application.

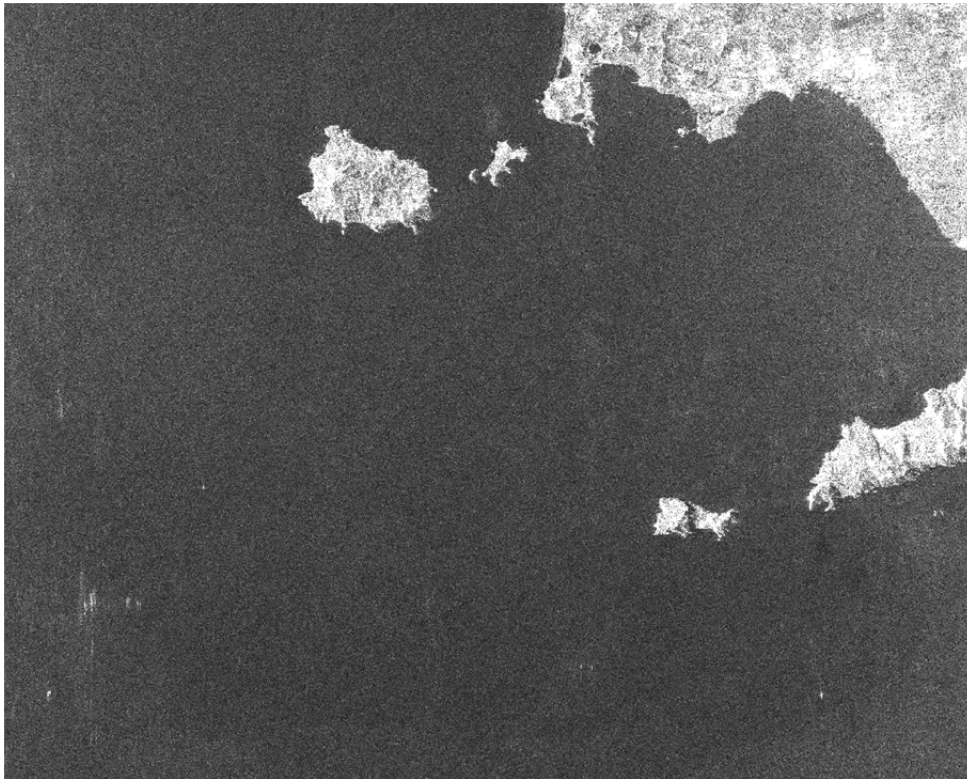


Fig. 6.12 ALOS PALSAR image N° 5 (Scene ID: ALPSRP103250800).

6.3.2 Visual inspection of the COSMO-SkyMed SAR images

6.3.2.1 COSMO-SkyMed SAR image N° 1 (Scene ID: EL20130109_510815_2513585.6.2)

The COSMO-SkyMed SAR image N° 1 (see Fig. 6.13) has been preliminary inspected. Due to the large values of wind speed during the day before the acquisition date (see Tab. 6.3), swell waves propagating on the sea surface were expected. However, visual inspection of the SAR image has shown that no swell waves field is present. Three subsets of the image are reported in Figs. 6.14-6.16. They correspond to the areas marked with boxes in Fig. 6.13. Sea surface is really noisy and bright areas are present. No swell field is present and, therefore, the COSMO-SkyMed SAR image N° 1 has been not selected for WBA application.

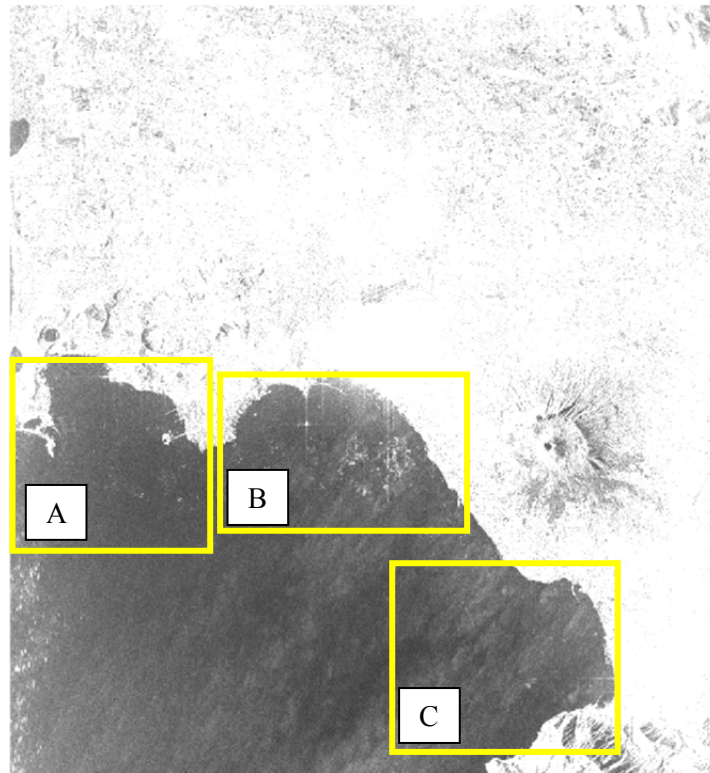


Fig. 6.13 COSMO-SkyMed SAR image N° 1 (Scene ID: EL20130109_510815_2513585.6.2). The boxes mark the subsets shown in Figs. 6.14-6.16.



Fig. 6.14 Subset A of the COSMO-SkyMed SAR image N° 1 (see Fig. 6.13).

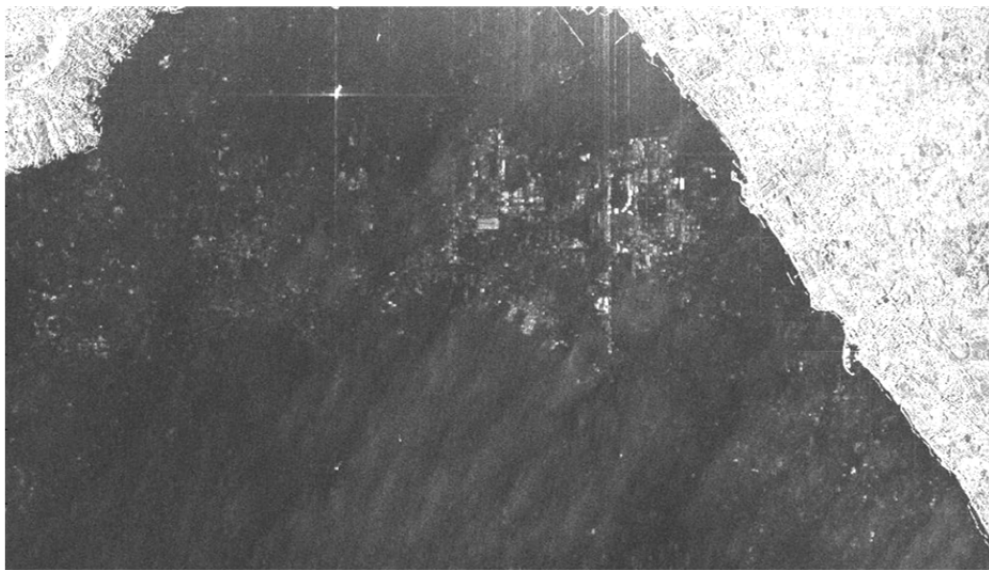


Fig. 6.15 Subset B of the COSMO-SkyMed SAR image N° 1 (see Fig. 6.13).

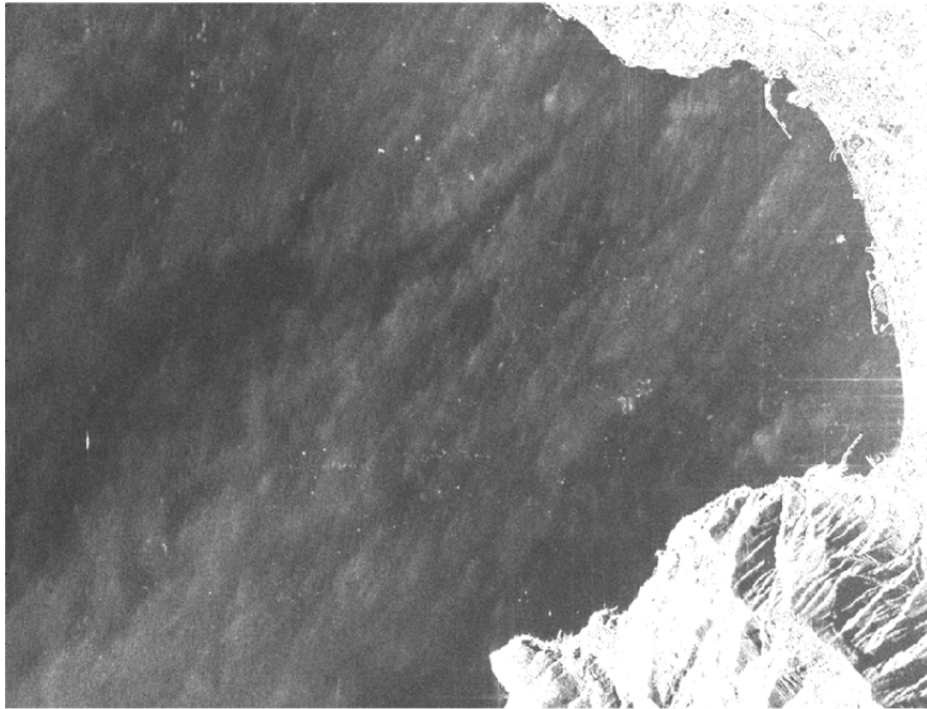


Fig. 6.16 Subset C of the COSMO-SkyMed SAR image N° 1 (see Fig. 6.13).

6.3.2.2 COSMO-SkyMed SAR image N° 2 (Scene ID: EL20130111_511370_2518037.6.2)

The COSMO-SkyMed SAR image N° 2 (see Fig. 6.17) has been preliminary inspected and a swell waves field has been identified. The three subsets marked with boxes in Fig. 6.17 are reported in Figs. 6.18-6.20. All of them show phenomena of swell shoaling and refraction despite the swell waves are less visible than in the ALOS PALSAR image N°1. Subset A (Fig. 6.18) is related to the northern side of the Gulf of Naples which, as shown in the detail of the "Golfo di Napoli" Nautical Chart [95] in Fig. 6.8, is particularly suitable for WBA application due to the gradually varying seafloor. Moreover, Fig. 6.18 shows that the swell field propagates along the ground range direction and that swell crests tend to align to iso-depth lines of seabed. Subset B (Fig. 6.19) is related to the Procida Channel (the channel between the mainland and the Procida island). Swell shoaling and refraction phenomena are present, as shown by the arrows in Fig. 6.19. Specifically, a swell waves field enters in the channel from the west entrance and, then, tends to align to the swell waves field which propagates on the area at east of the channel. The direction of propagation of the last swell waves field is due to the influence of the Ischia and Procida islands (i.e., swell waves refraction phenomenon along their coasts). However, this channel is characterized by high values of sea surface current [99] and the, therefore, the WBA cannot be applied (see section 4.1.4). Subset C (Fig. 6.20) is related to the Gulf of Pozzuoli, a portion of the Gulf of Naples. Fig. 6.21 shows a detail of the "Golfo di

Pozzuoli" Bathymetric Chart [97] and it reveals that the seabed gradually varies up to the shoreline. However, swell waves propagate almost along the SAR flight direction and, therefore, the WBA cannot be applied (see section 4.1.4).

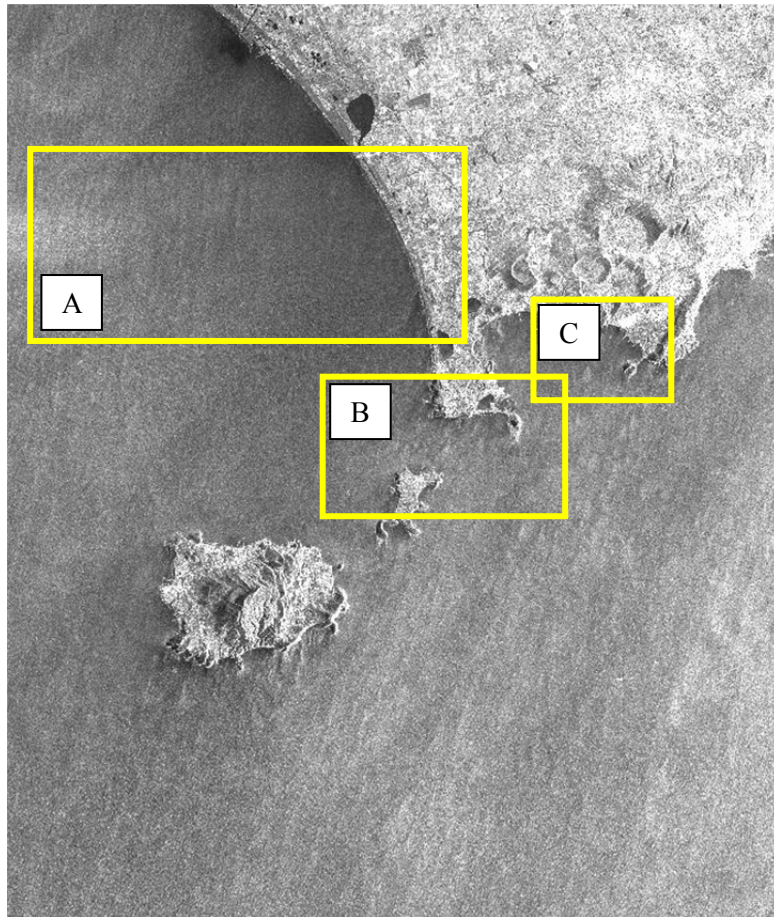


Fig. 6.17 COSMO-SkyMed SAR image N° 2 (Scene ID: EL20130111_511370_2518037.6.2). The boxes mark the subsets shown in Figs. 6.18-6.20.

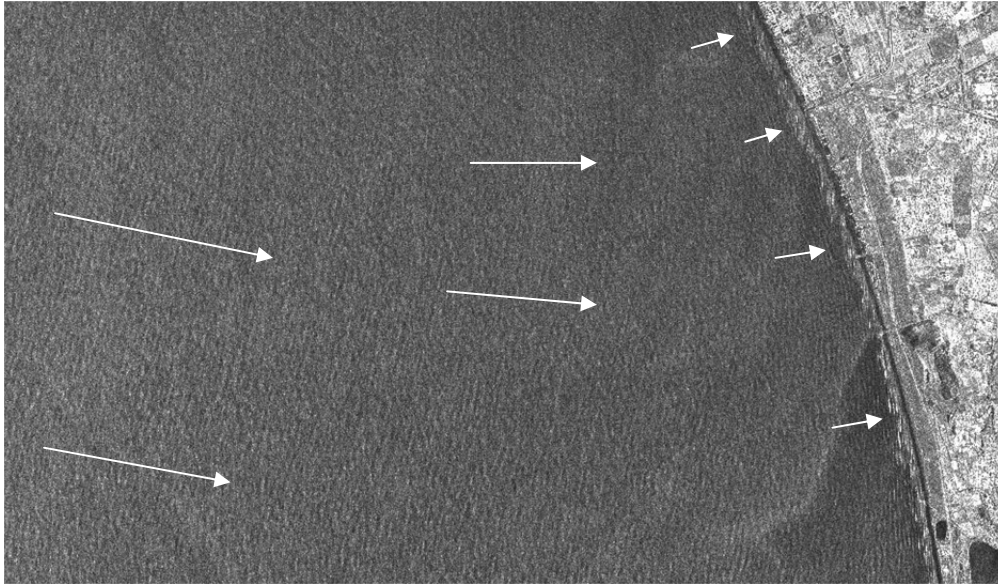


Fig. 6.18 Subset A of the COSMO-SkyMed SAR image N° 2 (see Fig. 6.17). The arrows show the direction of propagation of swell waves.



Fig. 6.19 Subset B of the COSMO-SkyMed SAR image N° 2 (see Fig. 6.17). The arrows show the direction of propagation of swell waves.

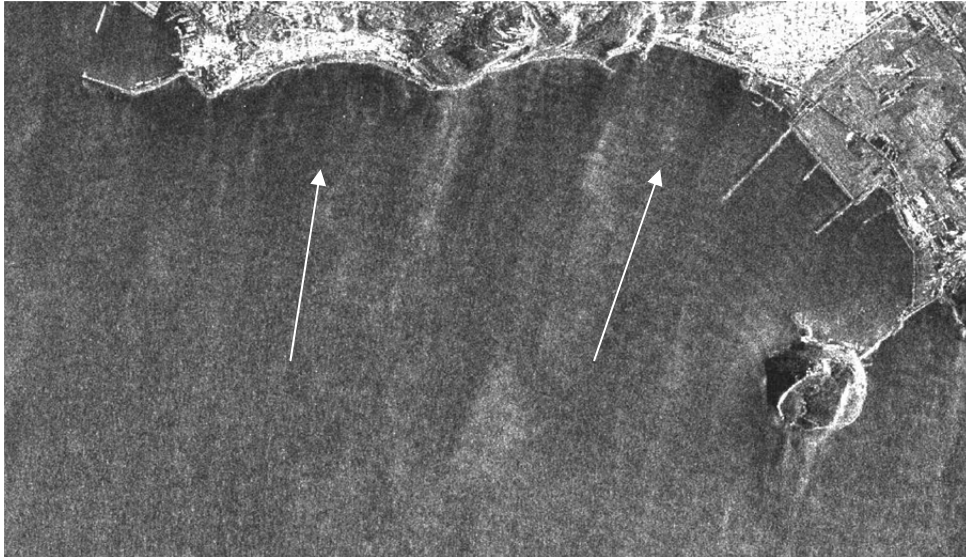


Fig. 6.20 Subset C of the COSMO-SkyMed SAR image N° 2 (see Fig. 6.17). The arrows show the direction of propagation of swell waves.

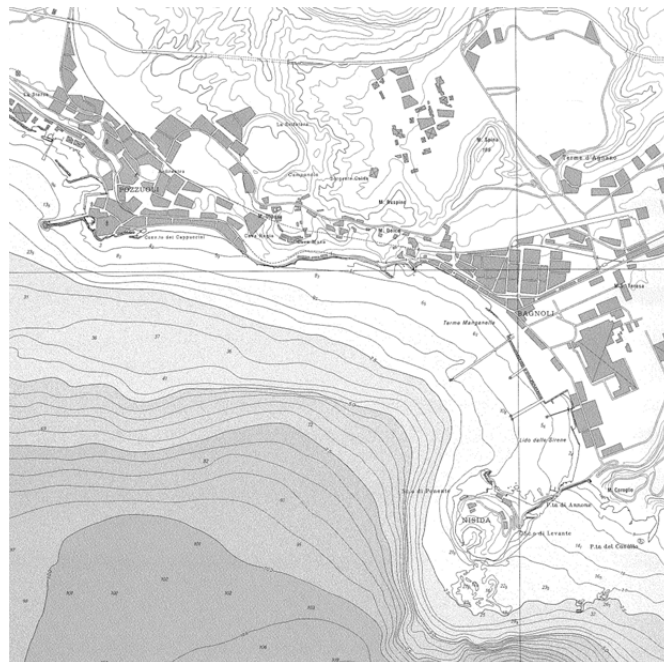


Fig. 6.21 Detail of the "Golfo di Pozzuoli" Bathymetric Chart [97].

6.3.2.3 COSMO-SkyMed SAR image N° 3 (Scene ID: EL20121222_507597_2477243.6.2)

The COSMO-SkyMed SAR image N° 3 (see Fig. 6.22) has been preliminary inspected and a swell wave field has been identified. However, subset A reported in Fig. 6.23 shows that swell waves propagate almost along the SAR flight direction and, therefore, the WBA cannot be applied (see section 4.1.4). The COSMO-SkyMed SAR image N° 6 has been not considered for application of WBA.

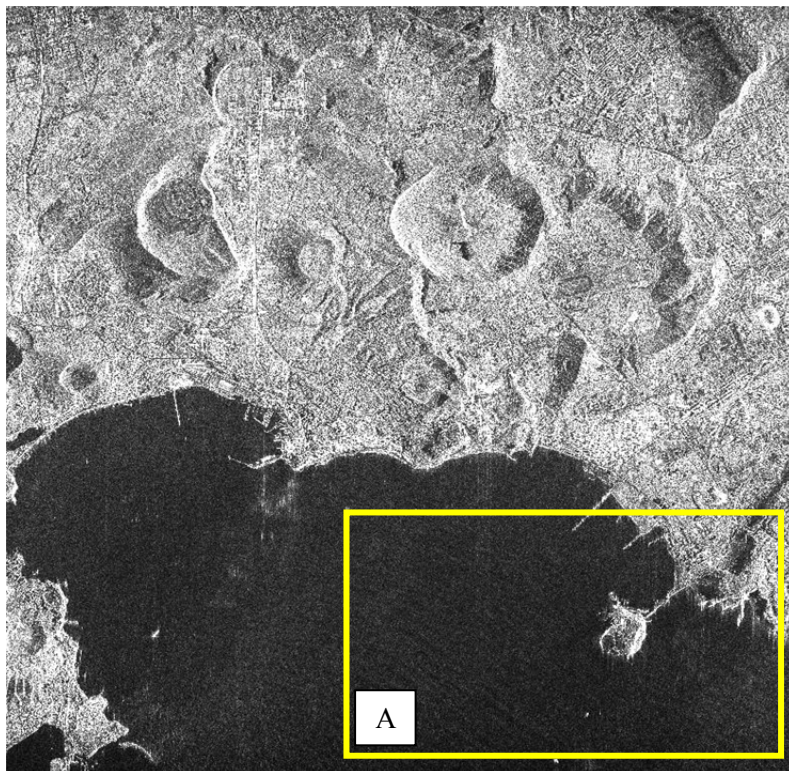


Fig. 6.22 COSMO-SkyMed SAR image N° 3 (Scene ID: EL20121222_507597_2477243.6.2). The box marks the subset shown in Fig. 6.23.

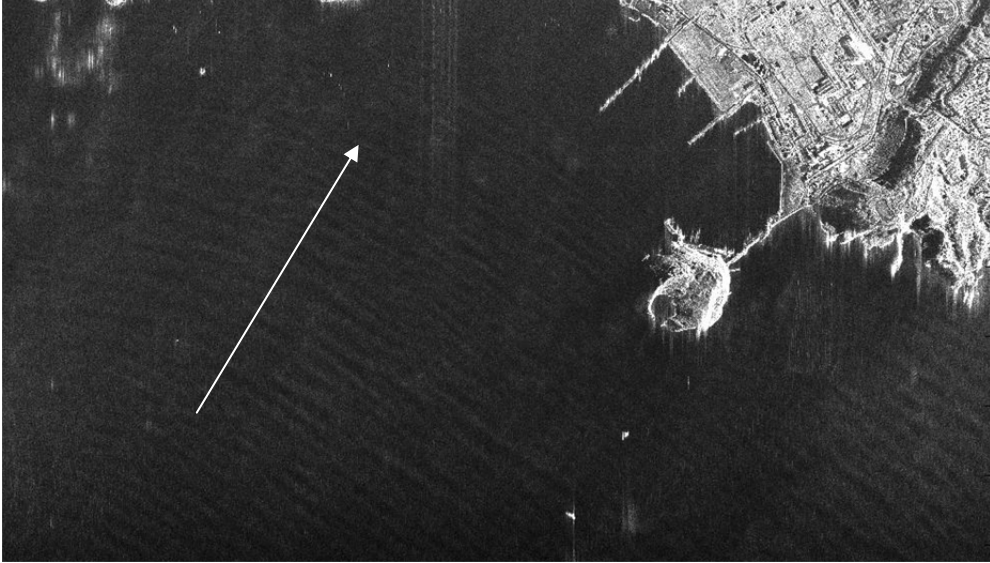


Fig. 6.23 Subset A of the COSMO-SkyMed SAR image N° 3 (see Fig. 6.22). The arrows show the direction of propagation of swell waves.

6.3.2.4 COSMO-SkyMed SAR image N° 4 (Scene ID: EL20130120_512956_2545081.6.2)

The COSMO-SkyMed SAR image N° 4 (see Fig. 6.24) has been preliminary inspected and a swell waves field has been identified in the northern part of the Gulf of Naples. However, subset A (Fig. 6.25) shows that this swell field is weak and not enough well visible for WBA application. Moreover, the SAR image presents some bright areas on the sea surface. Therefore, the COSMO-SkyMed SAR image N° 4 has been not considered for application of WBA.

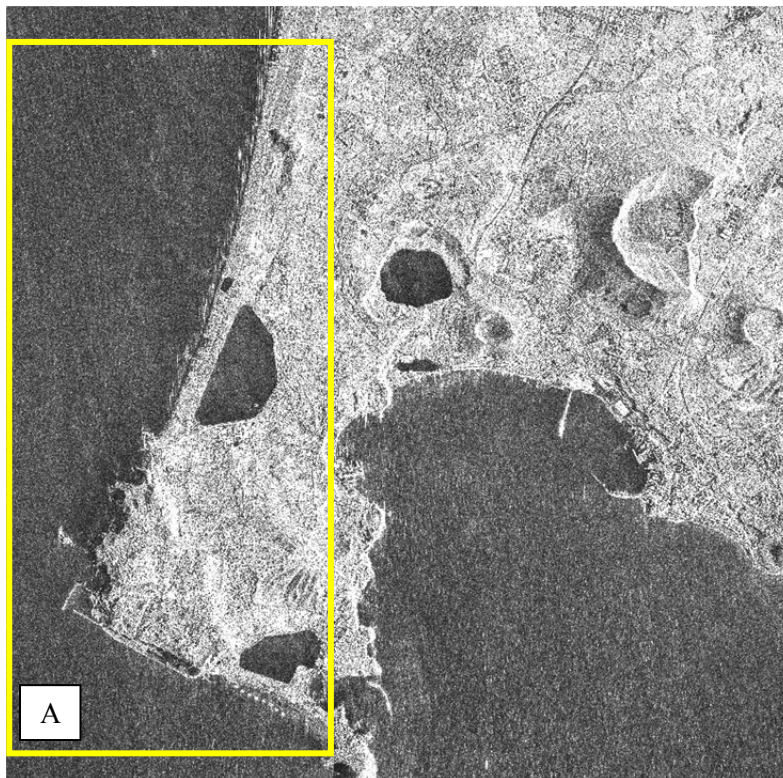


Fig. 6.24 COSMO-SkyMed SAR image N° 4 (Scene ID: EL20130120_512956_2545081.6.2). The box marks the subset shown in Fig. 6.25.

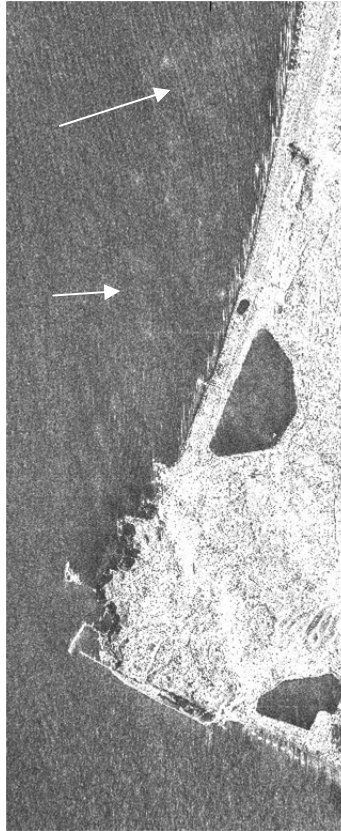


Fig. 6.25 Subset A of the COSMO-SkyMed SAR image N° 4 (see Fig. 6.24). The arrows show the direction of propagation of swell waves.

6.3.2.5 COSMO-SkyMed SAR image N° 5 (Scene ID: EL20130210_514951_2630659.6.2)

The COSMO-SkyMed SAR image N° 5 (see Fig. 6.26) has been preliminary inspected and swell waves propagating on the sea surface have been identified. However, subset A (Fig. 6.27) and subset B (Fig. 6.28) show that the swell field is weak and not enough well visible for WBA application. The SAR image presents some bright areas on the sea surface and, therefore, presence of further phenomena is supposed, i.e. swell waves do not fully characterize sea surface state. Therefore, the COSMO-SkyMed SAR image N° 5 has been not considered for application of WBA.

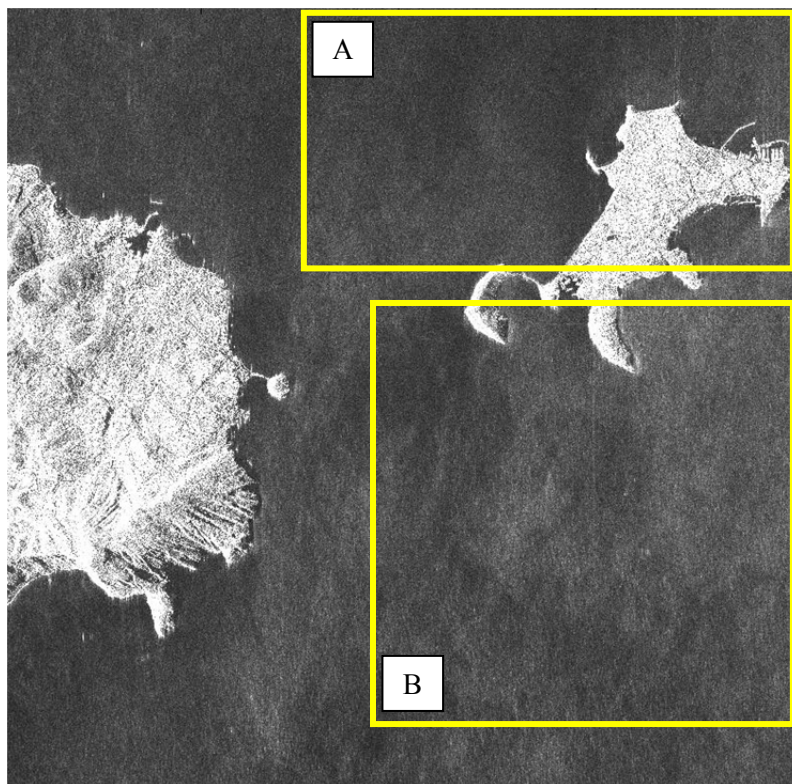


Fig. 6.26 COSMO-SkyMed SAR image N° 5 (Scene ID: EL20130210_514951_2630659.6.2). The boxes mark the subsets shown in Figs. 6.26 - 6.27.

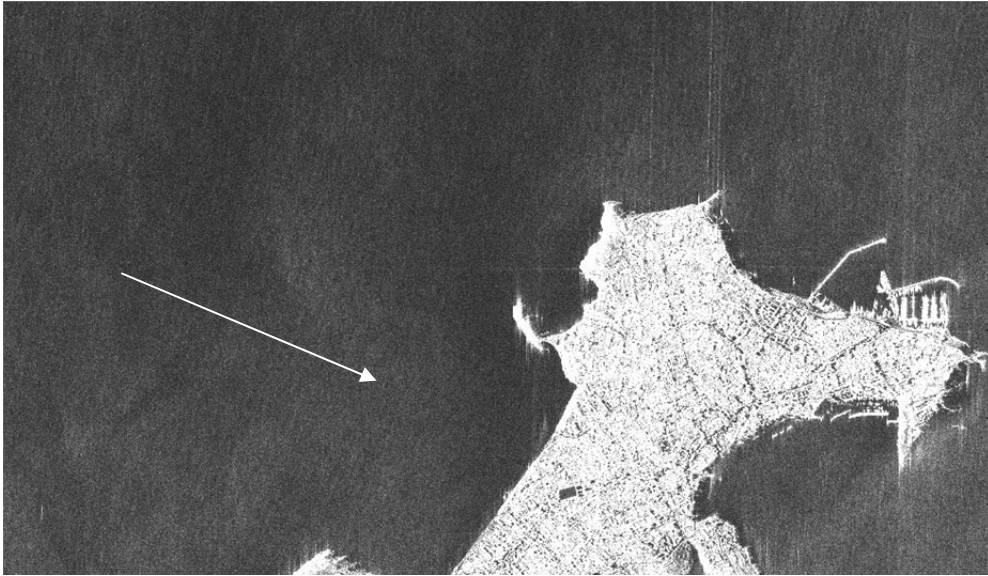


Fig. 6.27 Subset A of the COSMO-SkyMed SAR image N° 5 (see Fig. 6.26). The arrow shows the direction of propagation of swell waves.

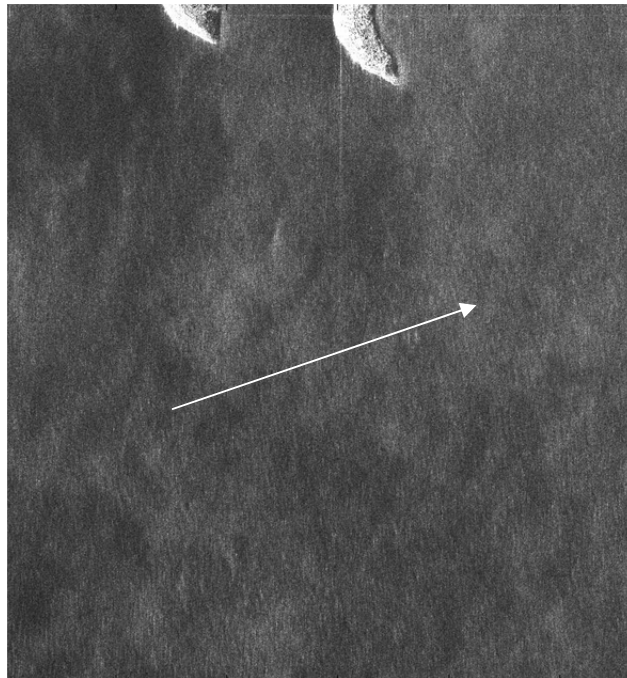


Fig. 6.28 Subset B of the COSMO-SkyMed SAR image N° 5 (see Fig. 6.26). The arrow shows the direction of propagation of swell waves.

6.3.2.6 COSMO-SkyMed SAR image N° 6 (Scene ID: EL20130210_514951_2632986.6.2)

The COSMO-SkyMed SAR image N° 6 (see Fig. 6.29) has been preliminary inspected and swell waves propagating on the sea surface have been identified. The three subsets marked with boxes in Fig. 6.29 are reported in Figs. 6.30-6.32. All of them show phenomena of swell shoaling and refraction. However, sea surface in both subset A and subset B is characterized by swell waves propagating almost along the SAR flight direction and, therefore, these subsets are not suitable for WBA application (see section 4.1.4). Subset C shows that the swell field is weak and not enough well visible for WBA application. Moreover, the SAR image presents some bright areas on sea surface and, therefore, presence of further phenomena is supposed, i.e. swell waves do not fully characterize sea surface state. Therefore, the COSMO-SkyMed SAR image N° 6 has been not considered for application of WBA.

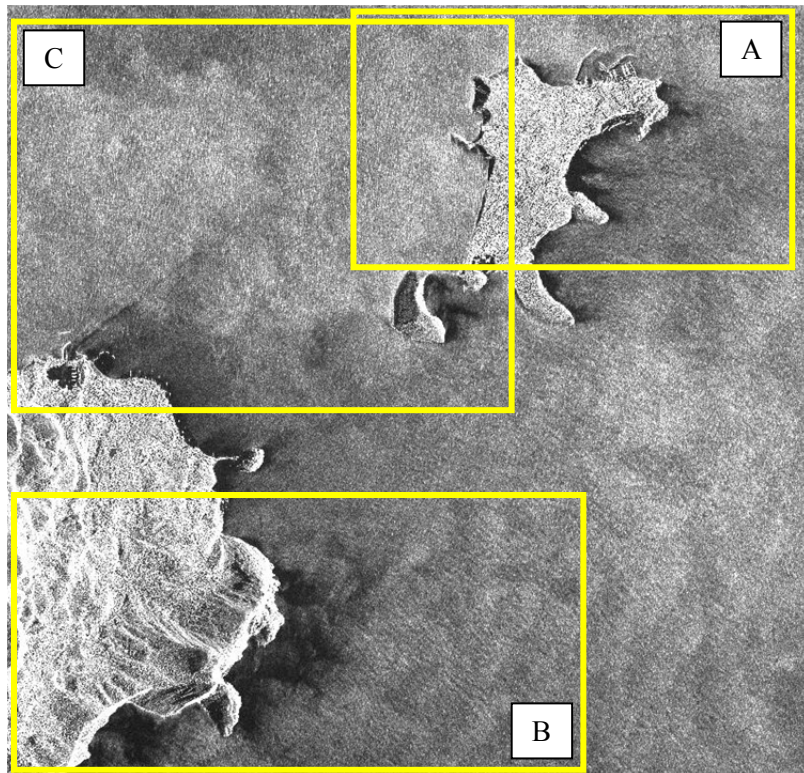


Fig. 6.29 COSMO-SkyMed SAR image N° 6 (Scene ID: EL20130210_514951_2632986.6.2).

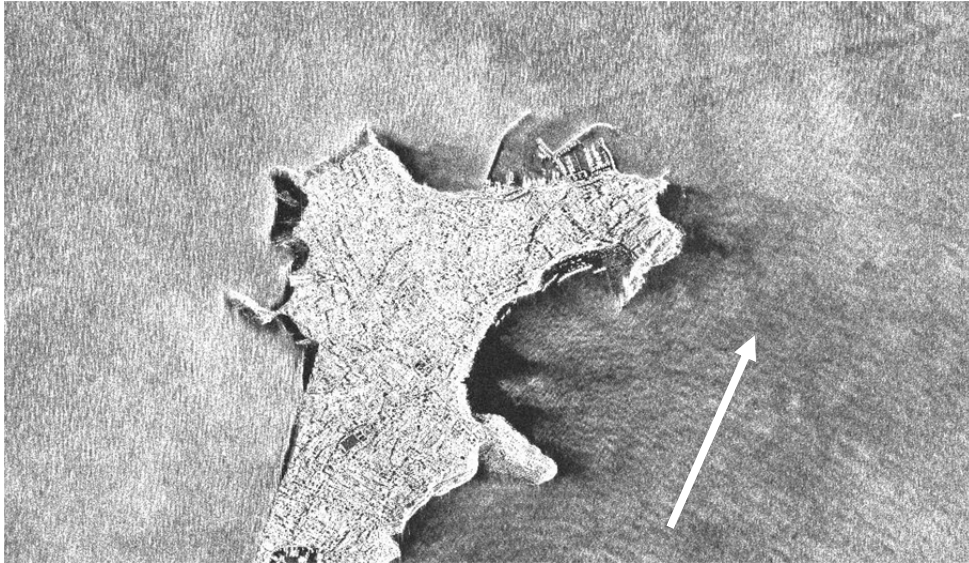


Fig. 6.30 Subset A of the COSMO-SkyMed SAR image N° 6 (see Fig. 6.29). The arrow shows the direction of propagation of swell waves.

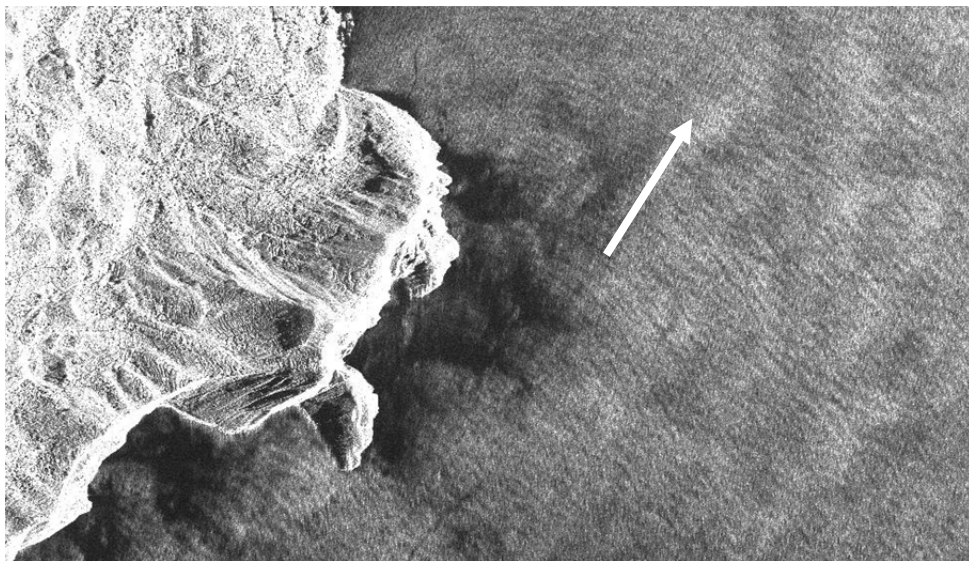


Fig. 6.31 Subset B of the COSMO-SkyMed SAR image N° 6 (see Fig. 6.29). The arrow shows the direction of propagation of swell waves.

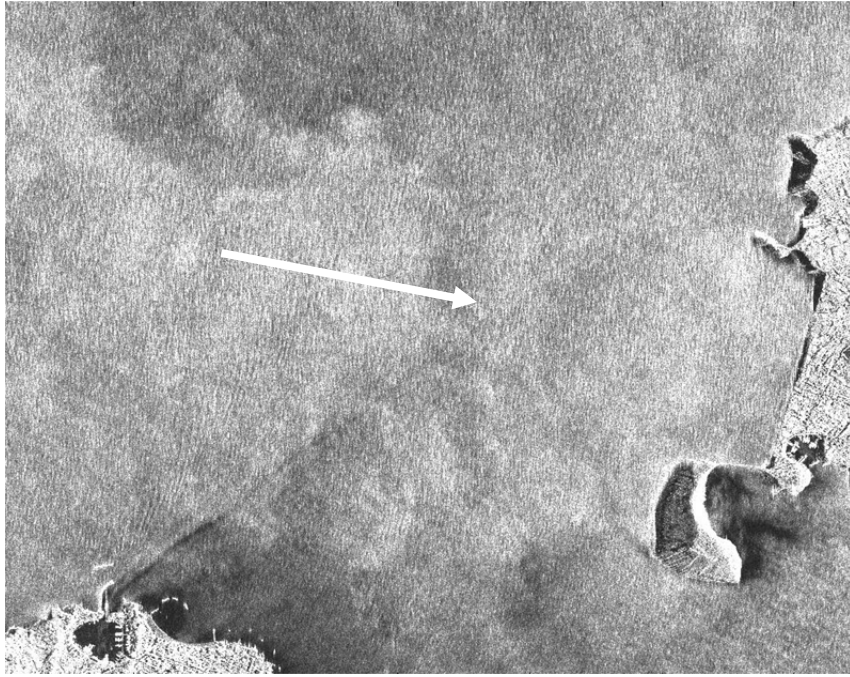


Fig. 6.32 Subset C of the COSMO-SkyMed SAR image N° 6 (see Fig. 6.29). The arrow shows the direction of propagation of swell waves.

6.4 Experimental results obtained on the selected ALOS PALSAR image

As a result of the preliminary visual inspection of the available SAR images performed in Section 6.3.1, the ALOS PALSAR image N°1 has been selected for further study and testing of the proposed Wave-Based Algorithm (see Section 5.2) for bathymetric data retrieval [100]. Specifically, the portion of the SAR image related to the northern side of the Gulf of Naples (see Fig. 6.33) has been identified as the most promising area for WBA application since all the requirements listed in Section 4.1.4 are satisfied [92].

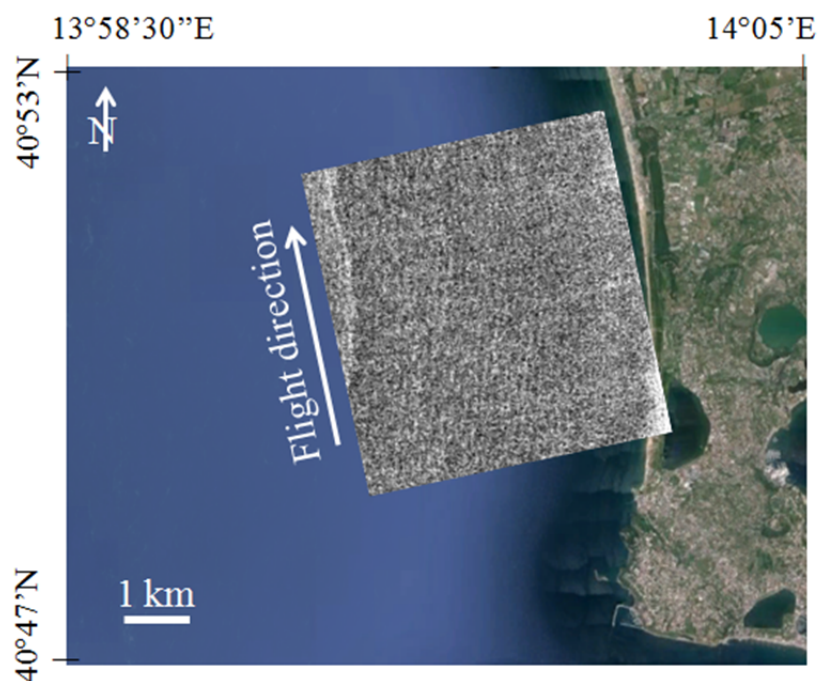


Fig. 6.33 Subset of the ALOS stripmap image covering the northern side of the Gulf of Naples, Italy (background image © Google Earth), selected for testing the proposed Wave-Based Algorithm.

6.4.1 Tracking of swell shoaling and refraction phenomena on the selected ALOS PALSAR image

The proposed Wave-Based Algorithm described in Chapter 5 has been implemented on the selected subset of the ALOS PALSAR image N°1. Specifically, the performed preliminary

visual analysis has allowed to estimate the wavelength and direction of propagation of swell waves on the selected subset (Fig. 6.34). Therefore, the range of admissible wavelength and propagation angle have been set to [50 m; 200 m] and [0°; 30°], respectively.

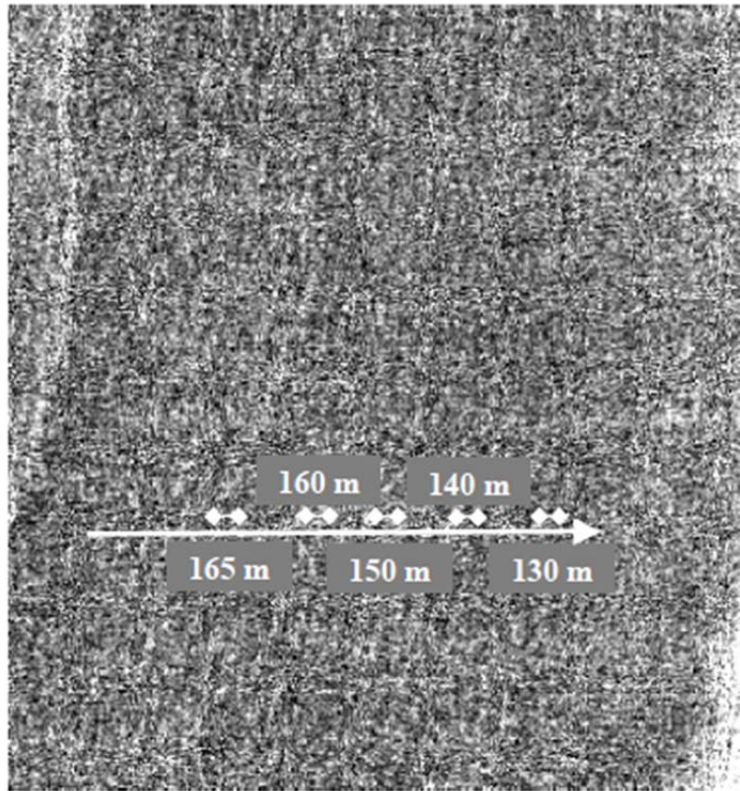


Fig. 6.34 Values of swell wavelength on the selected subset of the ALOS PALSAR image N°1 retrieved from preliminary visual inspection.

In order to retrieve the values of swell wavelength and angle of propagation throughout the subset, the following steps have been performed (see Fig. 5.4) [89]:

- 1) The image has been resized by setting the scaling factor to lead to a degraded spatial resolution of about 15 m, which is still able to correctly sample the shortest admissible swell wavelength (see Tab. 6.4).
- 2) A median filter of 5 x 5 pixels kernel size has been applied on the resized image to further reduce the noise.
- 3) The dimension of the scanning window has been selected to be 128 x 128 resized pixels, i.e. 2 km x 2 km, and the raster approach has been selected to scan the image. The scanning window has been moved by a constant distance of 5 resized pixels along the track, starting from open sea and up to the shoreline. The upper edge of the scanning

window along each track is set at a distance of 5 resized pixels from the upper edge of the previous one. As a consequence, the area under study has been covered by 40 tracks and a numeration has been assigned so that the first track is the one laying alongside of the upper edge of the investigated area.

For each position of the scanning window a 2-D image spectrum has been retrieved. Since the conditions for linear imaging model [59] are satisfied, the peak in the 2-D retrieved spectrum shows the dominant wavelength and the dominant wave direction of propagation of all the waves present in the subset. However, sea surface is characterized by several wave components apart from swell waves and, therefore, the retrieved sea surface spectrum does not show a single prominent peak when the theory-driven algorithm is applied (Fig. 6.35).

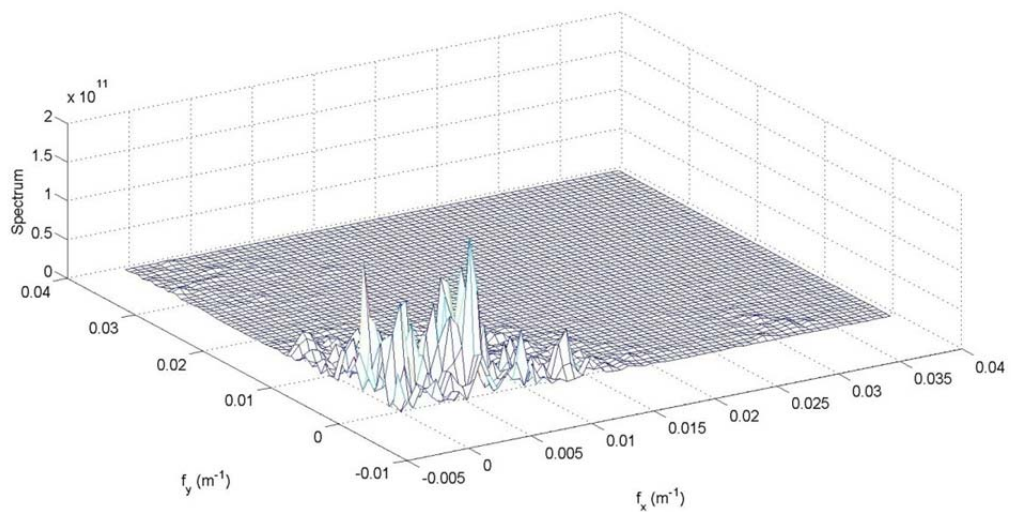


Fig. 6.35 Example of retrieved sea surface spectrum when the theory-driven algorithm is applied to the area covered by the scanning window in the selected subset.

Therefore, some frequency-limitations have been introduced in order to identify the peak in the sea surface spectrum related to swell waves. Specifically, the following conditions have been set:

- a) wavelength peak $L \in [50; 200]$ m;
- b) wave angle of propagation $\varphi \in [0^\circ; 30^\circ]$;
- c) maximum deviation of the wave propagation direction between two consecutive positions of the scanning window along the same track $\Delta\varphi|_{\text{MAX}} = 15^\circ$ [39], [91].

Values of L and φ have been retrieved throughout the image and they have been stored in two matrices, respectively.

- 4) For each value in the obtained L and φ matrices, the median value has been evaluated by considering the previous and the further values along the same row. This step has been performed twice.
- 5) A median filter of kernel 5×5 has been applied to the resulting L and φ matrices.
- 6) Smoothing of the elements along the rows of the obtained L and φ matrices has been performed by using a moving average with a 20-element span.

A complete list of the setting parameters is provided in Tab. 6.4.

Setting Parameters	Value
Scaling factor	2.5
scanning window size	128 x 128 resized pixels
scanning window sampling step	5 resized pixels
$\Delta\varphi _{\text{MAX}}$	15°
Kernel size for median filter on the SAR image	5 x 5 resized pixels
Kernel size for median filter on the L and φ matrixes	5 x 5 elements
Moving average span	20 elements
L_{min}	50 m
L_{max}	200 m
φ_{min}	0°
φ_{max}	30°

Tab. 6.4 Setting parameters for implementation of the proposed WBA algorithm on the selected ALOS PALSAR image.

To highlight the achieved improvement in swell detection and investigation capabilities, Fig. 6.36 reports the retrieved L -peak values along a track of the study area, for both the case of application of the theory-driven and proposed algorithm. The estimated wavelength by the theory-driven algorithm is unstable, and extremely large, unrealistic, values (up to 2000 m long wavelength) are derived. This means that the spectral analysis is not correctly tracking the desired wave field. The application of preprocessing, smoothing and limitations in the frequency domain keeps the wavelength more stable. Results show that the proposed algorithm provides L -peak values in the expected range for swell waves [32], [39], [91], and in agreement with the ones obtained from preliminary visual inspection (see Fig. 6.34). Moreover, as expected, L -peak values decrease as approaching the coast. Hence it is possible to state that swell waves are properly tracked. Similarly, Fig. 6.37 reports the trend for the swell angle of

propagation related to the L -peak values reported in Fig. 6.36, for both the case of application of the theory-driven and the proposed algorithm. Again, implementation of the proposed algorithm provides values of swell angle of propagation consistent with the expected trend in the investigated area. Similar trends in swell wavelength and angle of propagation can be found for the other tracks covering the investigated subset.

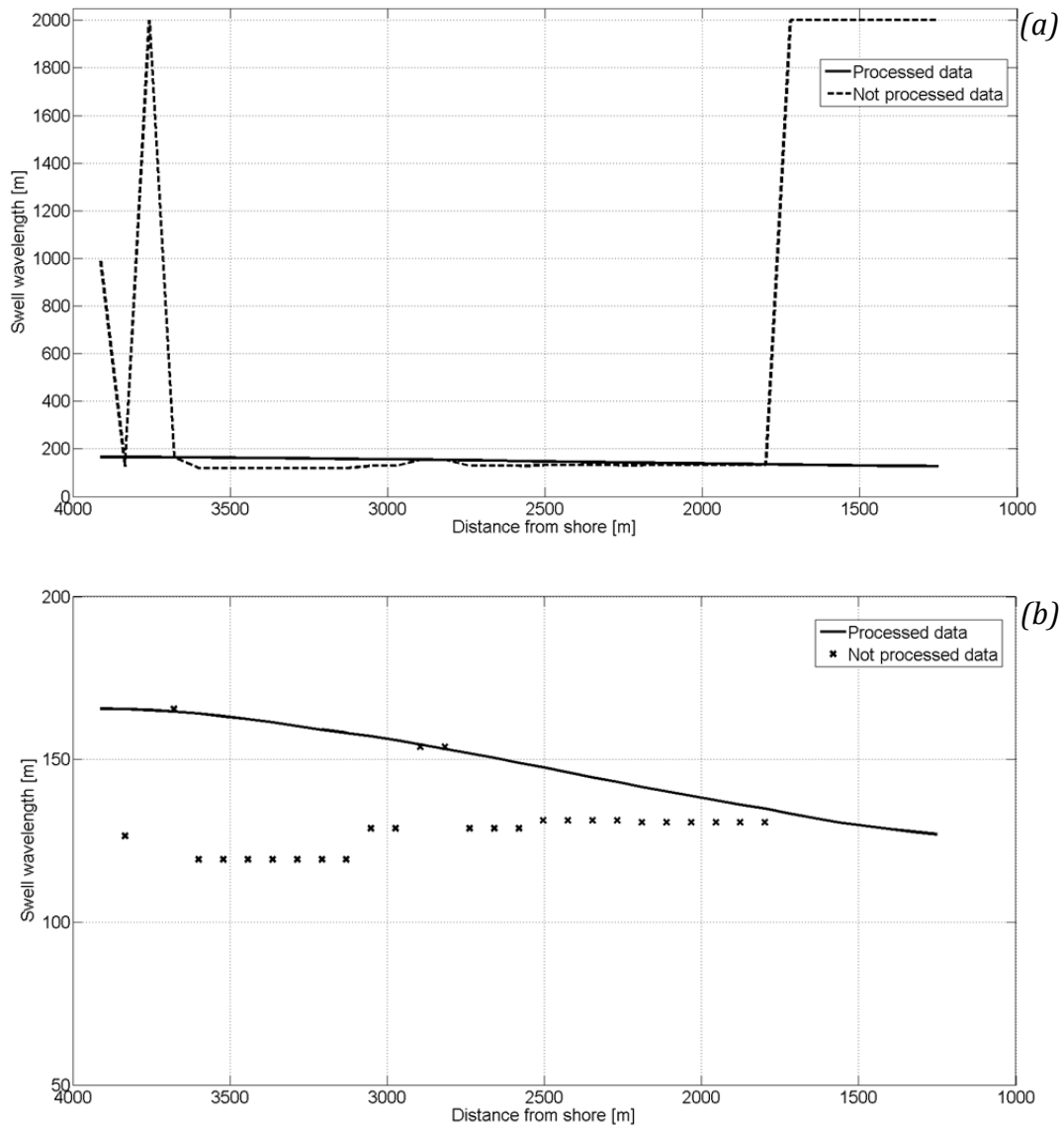


Fig. 6.36 (a) Retrieved L -peak values along the 35th track of the investigated area; (b) Zoom on the range [50 m; 200 m] [89].

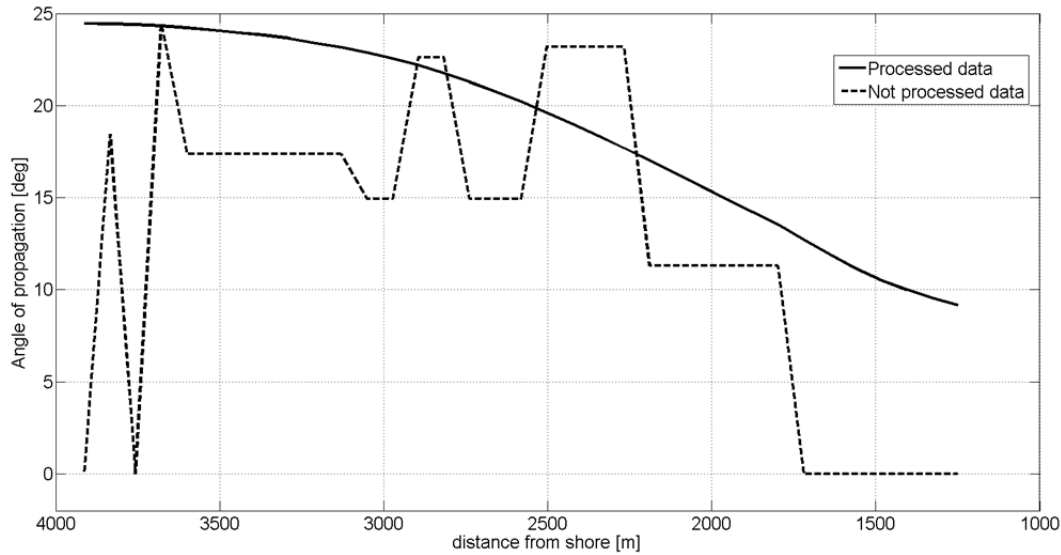


Fig. 6.37 Retrieved values of angle of propagation related to the L -peak values reported in Fig. 6.36 [89].

6.4.2 Digital Elevation Model retrieved from the selected ALOS PALSAR image

A first-guess approach has been implemented to estimate values of swell period throughout the selected subset. The available nautical charts [95], [96] have been adopted in order to have some reference values of water depth and the L values retrieved according to Section 6.4.1 have been used. Therefore, values of swell period have been estimated by computing depth with eq. (4.3) by using different trial values of T and by comparing the obtained value with the actual depth at a known point. Only values larger than the minimum threshold $t_{\min} = (2\pi L_{\max}/g)^{1/2}$ are considered, where L_{\max} is the maximum wavelength observed along the considered track. The retrieved T value has been kept along the whole track since, under certain conditions, the sensitivity of the depth to the wave period is very low and therefore high uncertainties on the wave period can be tolerated (see Section 5.1). Table 6.5 reports the estimated values of swell period for each track. The closer the track is to the bottom edge of the investigated area, the larger is the value of T . This trend can be explained considering the presence of two channels, i.e. the Procida Channel and the Ischia Channel, beneath the investigated area. Channels generate significant hydrodynamic effects, hence swell period may increase as approaching these areas.

Track Number	T [sec]
1-5	9.90
6-17	10.0
18-27	10.5
28-40	10.8

Tab. 6.5 Values of swell period for each track throughout the selected ALOS PALSAR image estimated with the first-guess approach.

Preliminary visual inspection of the selected subset has shown that two areas are characterized by the presence of misleading features on the SAR image (see Fig. 6.38). Those areas do not show prominent refraction and shoaling phenomena. Specifically, the offshore area (left circle in Fig. 6.38) lacked of well-defined swell waves propagating on the sea surface while the area closer to the coastline (right circle in Fig. 6.38) was affected by a wave breaking process that destroyed the swell waves propagation. Those areas have not been considered for Digital Elevation Model reconstruction.

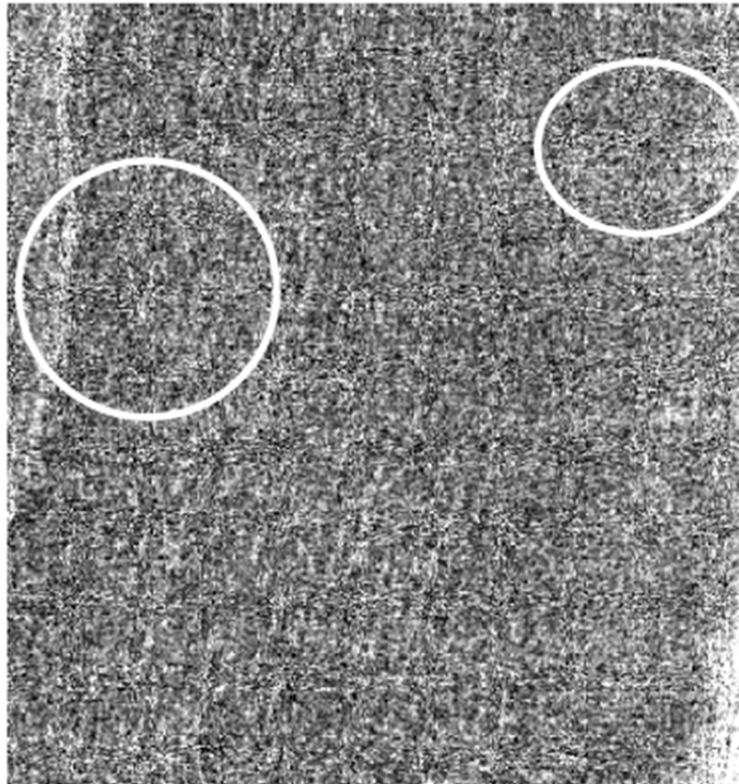


Fig. 6.38 The two circles mark areas characterized by the presence of misleading features on the SAR image.

The linear dispersion relation (eq. 4.3) has been applied to each scanning window by using the related estimated values of swell wavelength and period. Therefore, values of sea water depth have been estimated throughout the image and they have been recorded in a dedicated matrix. Fig. 6.39 shows the resulting DEM. Each track on the SAR image corresponds to a row in the retrieved sea water depth matrix and each location of the scanning window along the same track corresponds to a column along the same row.

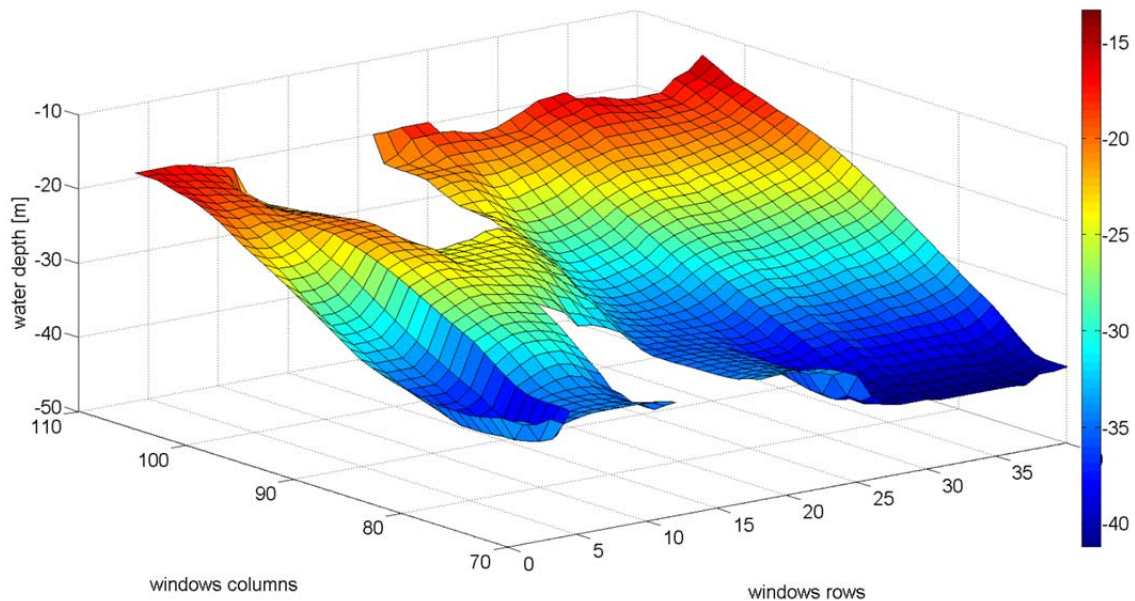


Fig. 6.39 Bathymetric map of the investigated area in the Gulf of Naples resulting from the application of the proposed algorithm for swell-based bathymetry to the selected ALOS PALSAR image [89].

The obtained results are in good agreement with the values of sea water depth reported in the "Golfo di Napoli" nautical chart [95]. Fig. 6.40 shows a correlation analysis performed considering 108 control points available from the chart and the corresponding values estimated with the proposed algorithm. The correlation between the data is very high, the correlation coefficient being 0.99. The mean difference results to be about 0.2 m and the maximum difference is 0.9 m. Finally, the standard deviation of the difference is about 0.4 m.

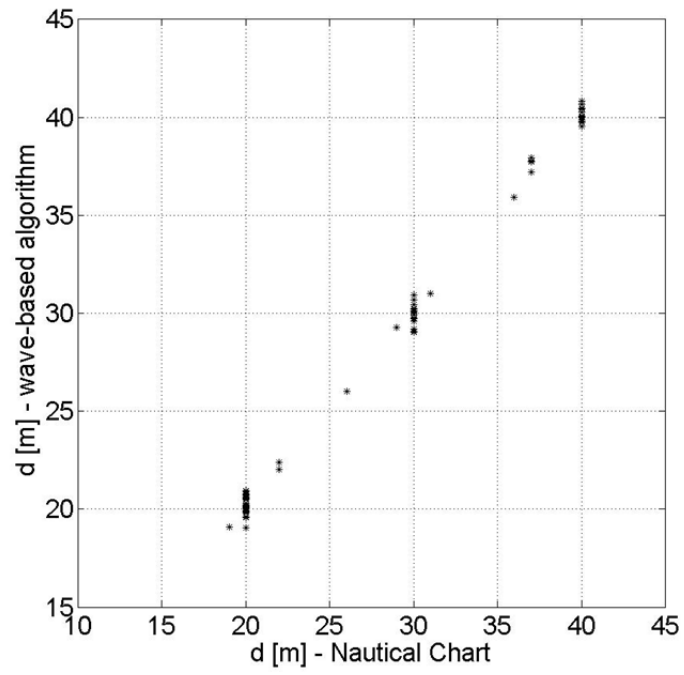


Fig. 6.40 Correlation analysis over the considered area of the ALOS PALSAR image performed with the available control points of the "Golfo di Napoli" nautical chart [95] and the corresponding values retrieved with the proposed WBA algorithm.

6.5 Experimental results obtained on the selected COSMO-SkyMed SAR image

As a result of the preliminary visual inspection of the available SAR images performed in Section 6.3.2, the COSMO-SkyMed image N°2 has been selected for further study and testing of the proposed Wave-Based Algorithm (see Section 5.2) for bathymetric data retrieval. Specifically, as for the ALOS image (see previous section), the portion of the SAR image related to the northern side of the Gulf of Naples (see Fig. 6.40) has been identified as the most promising area for WBA application since all the requirements listed in Section 4.1.4 are satisfied.

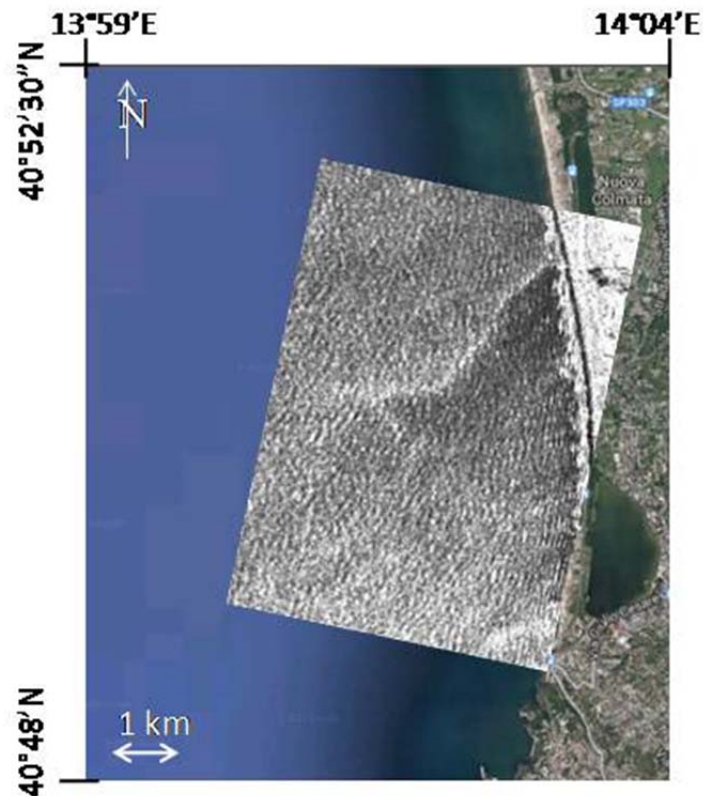


Fig. 6.40 Subset of the COSMO-SkyMed SAR stripmap image covering the northern side of the Gulf of Naples, Italy (background image © Google Earth), selected for testing the proposed Wave-Based Algorithm.

6.5.1 Tracking of swell shoaling and refraction phenomena on the selected COSMO-SkyMed SAR image

The proposed Wave-Based Algorithm described in Chapter 5 has been implemented on the selected subset of the COSMO-SkyMed SAR image N°2. Specifically, the performed preliminary visual analysis has allowed to estimate the wavelength and direction of propagation of swell waves on the selected subset (Fig. 6.41). Therefore, the range of admissible wavelength and propagation angle have been set to [40 m; 120 m] and [0°; 30°], respectively.

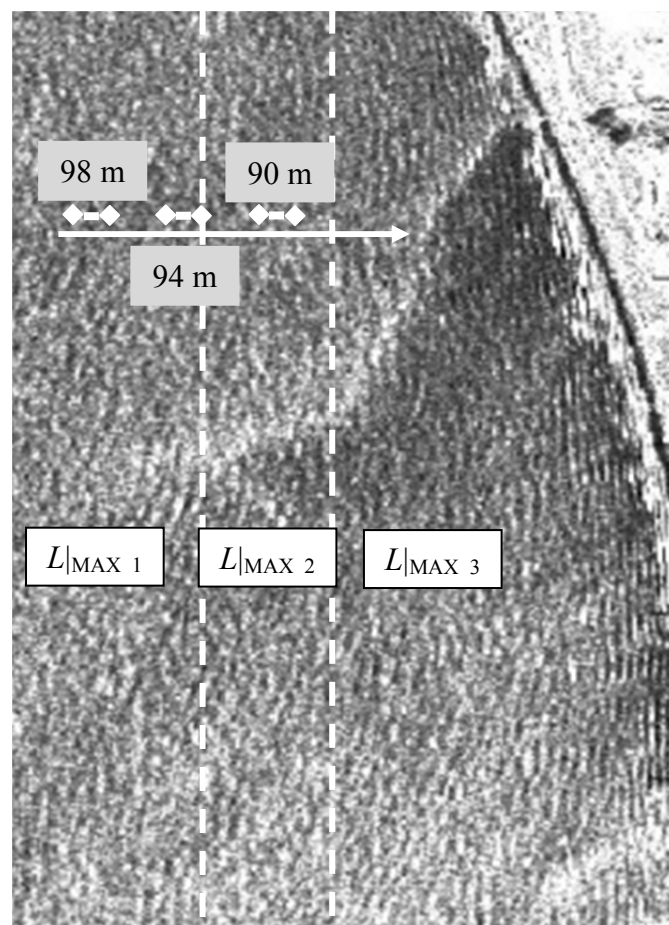


Fig. 6.41 Values of swell wavelength on the selected subset of the COSMO-SkyMed SAR image N°2 retrieved from preliminary visual inspection and the portions related to the different values of $L|_{MAX}$.

In order to retrieve the values of swell wavelength and angle of propagation throughout the subset, the land has been removed and the steps from 1) to 5) listed in Section 6.4.1 have been performed by using the setting parameters reported in Tab. 6.6. Specifically, the image has been resized by setting the scaling factor to lead to a degraded spatial resolution of 12 m, which is

still able to correctly sample the shortest admissible swell wavelength. The subset has been covered by 55 tracks. Moreover, three different $L|_{MAX}$ values have been used, i.e. $L|_{MAX_1}$, $L|_{MAX_2}$, and $L|_{MAX_3}$ (see Tab. 6.6). Each of them is related to a different portion of the SAR image as shown in Fig. 6.41. Indeed, the performed analysis has revealed that more strict frequency-limitations are needed in the case of the COSMO-SkyMed SAR image with respect to the ALOS PALSAR one in order to properly identify the peak in the sea surface spectrum related to swell waves. On the contrary, smoothing of the elements along the rows of the retrieved L and φ matrices (step 6 in Section 6.4.1) has not been required.

Setting Parameter	Value
Scaling factor	4.8
scanning window size	128 x 128 resized pixels
scanning window sampling step	5 resized pixels
$\Delta\varphi _{MAX}$	15°
Kernel size for median filter on the SAR image	5 x 5 resized pixels
Kernel size for median filter on the L and φ matrixes	5 x 5 elements
Moving average span	20 elements
L_{min}	40 m
$L _{MAX_1}$	120 m
$L _{MAX_2}$	100 m
$L _{MAX_3}$	80 m
φ_{min}	0°
φ_{max}	30°

Tab. 6.6 Setting parameters for implementation of the proposed WBA algorithm on the selected COSMO-SkyMed SAR image.

To highlight the achieved improvement in swell detection and investigation capabilities, Fig. 6.42 reports the retrieved L -peak values along a track of the study area, for both the case of application of the theory-driven and proposed algorithm. The estimated wavelength by the theory-driven algorithm is unstable, and extremely large, unrealistic, values (up to almost 1600 m long wavelength) are derived. This means that the spectral analysis is not correctly tracking the desired wave field. The application of preprocessing and limitations in the frequency domain keeps the wavelength more stable. Results show that the proposed algorithm provides L -peak values in the expected range for swell waves [32], [39], [91], and in agreement with the ones obtained from preliminary visual inspection (see Fig. 6.41). Moreover, as expected, L -peak values decrease as approaching the coast. Hence it is possible to state that swell waves are properly tracked. Similarly, Fig. 6.43 reports the trend for the swell angle of propagation related

to the L-peak values reported in Fig. 6.42, for both the case of application of the theory-driven and the proposed algorithm. Again, implementation of the proposed algorithm provides values of swell angle of propagation consistent with the expected trend in the investigated area. Similar trends in swell wavelength and angle of propagation can be found for the other tracks covering the investigated subset.

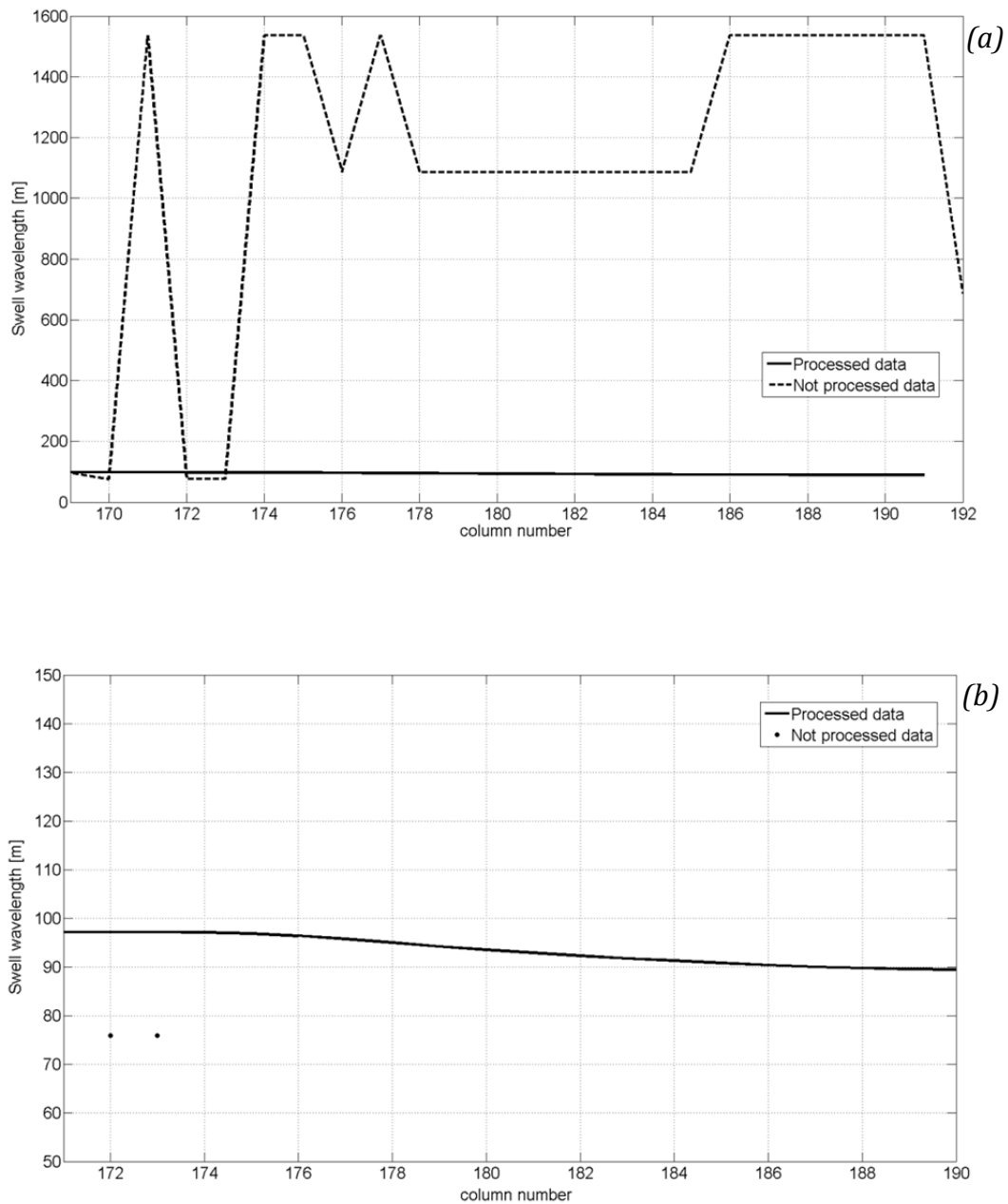


Fig. 6.42 (a) Retrieved L-peak values along the 13th track of the investigated area; (b) Zoom on the range [50 m; 150 m].

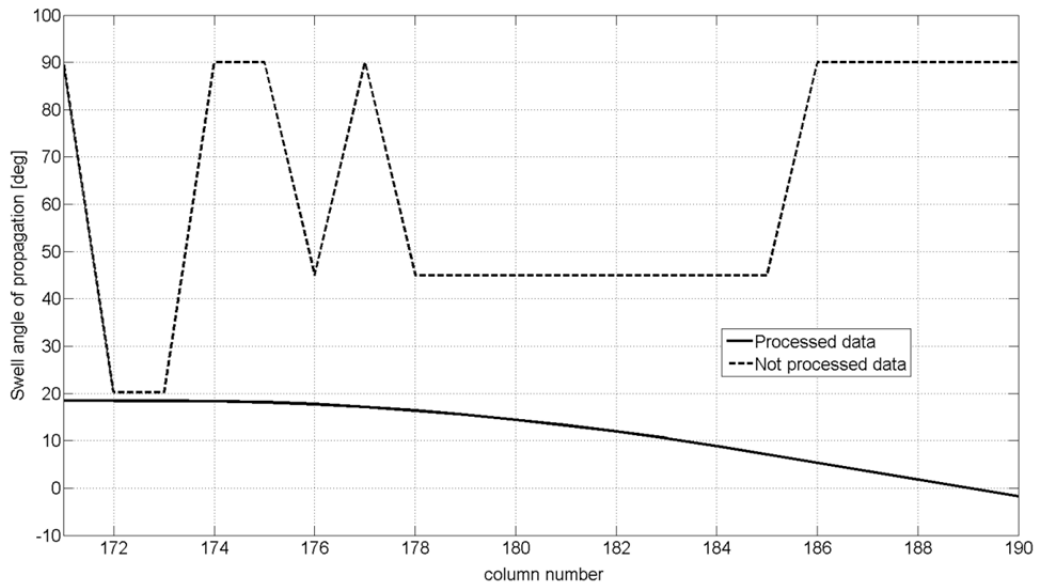


Fig. 6.43 Retrieved values of angle of propagation related to the L -peak values reported in Fig. 6.42.

6.5.2 Digital Elevation Model retrieved from the selected COSMO-SkyMed SAR image

As for the ALOS PALSAR image, also for the selected COSMO-SkyMed SAR image a first-guess approach has been implemented to estimate values of swell period throughout the selected subset. The available nautical charts [95], [96] have been adopted in order to have some reference values of water depth and the L values retrieved according to Section 6.5.1 have been used. Table 6.7 reports the estimated values of swell period for each track.

Preliminary visual inspection of the selected subset has shown that two areas must not be considered (see Fig. 6.44). The area marked with a rectangle in Fig. 6.44 presents some misleading features due to the presence of the coast. The other area marked in Fig. 6.44 does not show prominent refraction and shoaling phenomena since it lacks of well-defined swell waves propagating on the sea surface. Therefore, those areas have not been considered for Digital Elevation Model reconstruction.

Track Number	T [sec]
1-7	8.4
8-11	8.2
12-17	8.1
18-21	8.0
22-25	7.9
26-28	7.8
29-31	7.7
32	7.6
33-35	7.4
36-37	7.3
38-44	7.2
45-50	7.1
51-55	7.2

Tab. 6.7 Values of swell period for each track throughout the selected COSMO-SkyMed SAR image estimated with the first-guess approach.

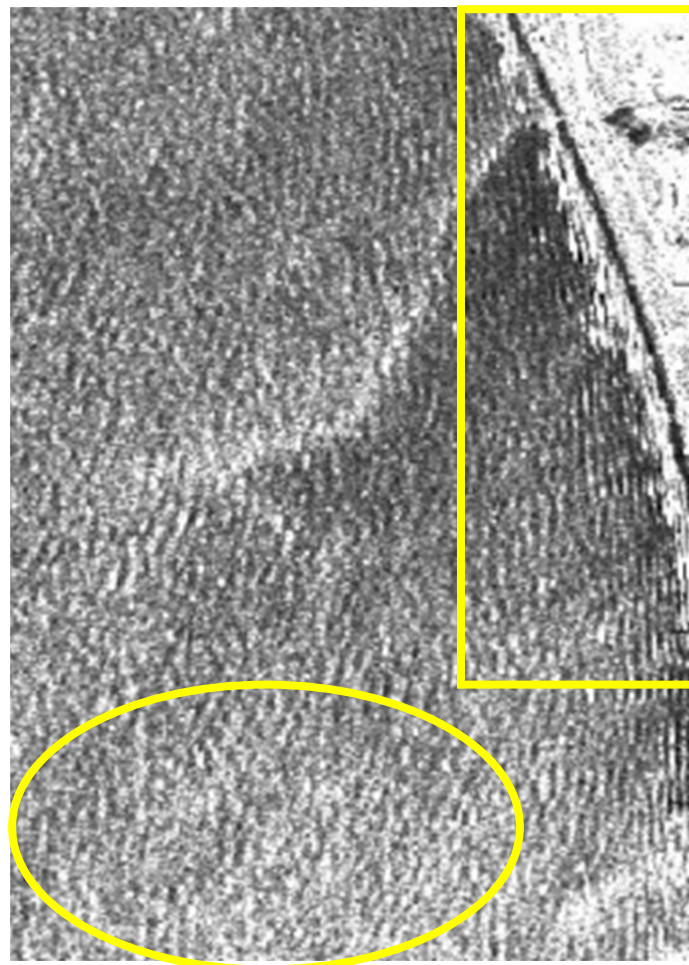


Fig. 6.44 Areas of sea surface characterized by misleading features due to the effect of the coast (rectangle) and to the lack of well-defined swell waves propagating on the sea surface (ellipse).

The linear dispersion relation (eq. 4.3) has been applied to each scanning window by using the related estimated values of swell wavelength and period. Therefore, values of sea water depth have been estimated throughout the image and they have been recorded in a dedicated matrix. Fig. 6.45 shows the resulting DEM. Each track on the SAR image corresponds to a row in the retrieved sea water depth matrix and each location of the scanning window along the same track corresponds to a column along the same row.

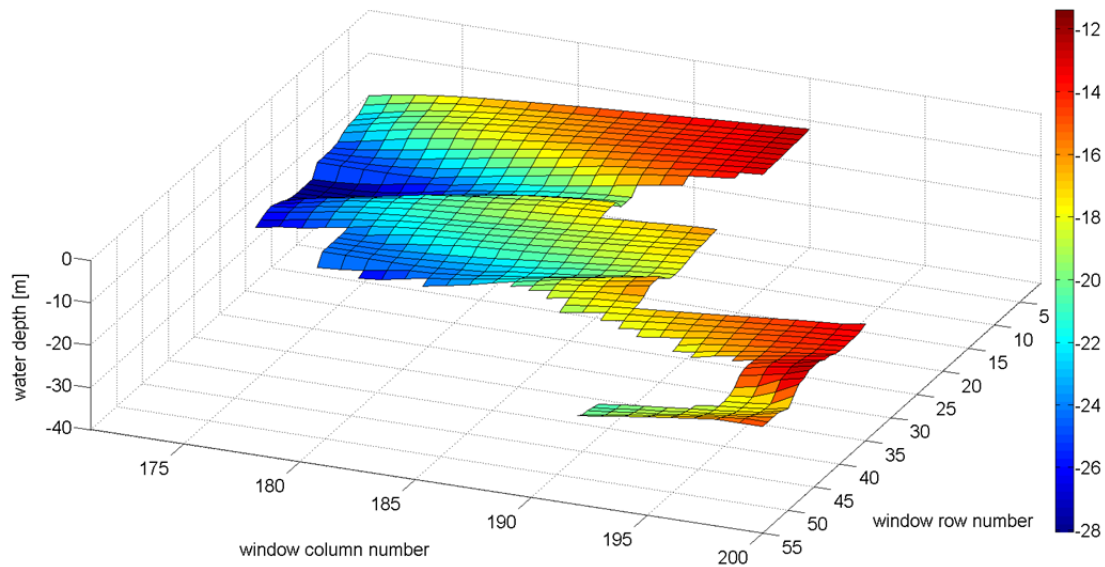


Fig. 6.45 Bathymetric map of the investigated area in the Gulf of Naples resulting from the application of the proposed algorithm for swell-based bathymetry to the selected COSMO-SkyMed SAR image.

The obtained results are in good agreement with the values of sea water depth reported in the "Golfo di Napoli" nautical chart [95]. Figure 6.46 shows a correlation analysis performed considering 97 control points available from the chart and the corresponding values estimated with the proposed algorithm. The correlation between the data is very high, the correlation coefficient being 0.99. The mean difference results to be about 0.0125 m and the maximum difference is 0.5 m. Finally, the standard deviation of the difference is about 0.2 m.

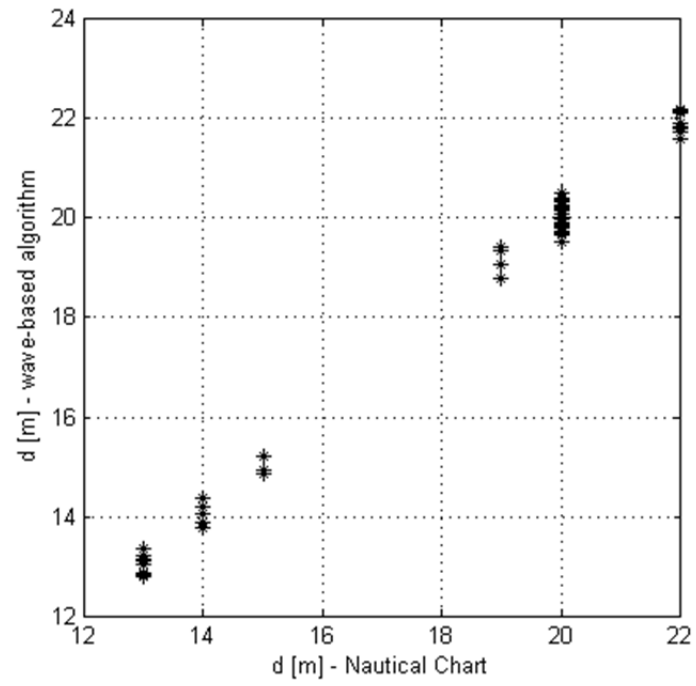


Fig. 6.46 Correlation analysis over the considered area of the COSMO-SkyMed SAR image performed with the available control points of the "Golfo di Napoli" nautical chart [95] and the corresponding values retrieved with the proposed WBA algorithm.

Chapter 7

Discussion and Conclusions

The performed study has shown that bathymetric features can be estimated by SAR data utilizing two families of processing techniques provided that a number of conditions are respected and with some limitations. In particular, bathymetric feature extraction is based either on exploitation of sea currents or on sea waves. The Current-Based Approach (CBA) needs proper modelling of three physical mechanisms: (a) the interaction of the currents with bottom topography; (b) interactions of surface current with the wind-driven spectrum of water waves; (c) response of radar backscatter to modulation of sea surface roughness, i.e. Bragg-waves. The physical processes involved in such technique need that significant sea currents are established and interact with sea floor (therefore superficial, wind-driven currents are not useful) and that wind speed is moderate to establish adequate Bragg-waves. Conducted experiments showed that strong currents with velocity larger than 0.5 m/s are needed to retrieve bathymetry for depths lower than 30 m and wind speed should be limited within the 3-12 m/s range.

Since modelling of the three involved physical mechanisms is not trivial in the general case, simplified approaches are reported in literature which all tend to show that best bathymetric reconstruction performance can be achieved when ridges are parallel to the flight direction and current is orthogonal to the ridges.

The extraction of bathymetric features by means of the proposed forward approaches (from bathymetry to simulated SAR image and back to adjust bathymetry through comparison between simulated and real images) relies on a number of a-priori information, including sea state, meteorological information and also sparse bathymetric information. In addition, the proposed methodologies still need significant intervention from human image interpreters. Some of these issues can be tackled considering an inverse approach (bathymetry is derived from surface currents, in turn estimated from SAR images), which needs a model to relate SAR image to sea currents and a technique to invert it. Such methodology was proposed making use of the Volterra Series Expansion and it was proved that bathymetric data can be retrieved without using in input any a-priori bathymetric measurements other than a single reference depth value.

A bathymetric algorithm to derive underwater bottom topography from SAR images has been presented. The algorithm is aimed at reducing the need for a-priori bathymetric and ancillary information and the role of human interpreters in the processing chain. For this reason, it is based on a simplified imaging model in which only the ground range kernel is used to calculate sea current variations generated by the local bathymetry. A theoretical error budget analysis has shown that the method is potentially able to generate depth profiles characterized by metric scale depth accuracy provided that the current velocity is sufficiently high and the wind speed is adequate to activate Bragg scattering. This accuracy is not expected to depend significantly on the radar wavelength and it can be achieved by medium resolution Stripmap products. However,

the required particularly favourable circumstances (e.g. strong current, uniform wind fields, and absence of long waves) are actually very rare in close areas, such as gulfs or inlets, and relative close seas, such as the Mediterranean Sea, because current velocity is too slow or tends to be irregular both in time and in intensity. For these reasons, the CBA has not been further considered in the present work.

More recent researches have led to the identification of a Wave-Based Approach (WBA) and methods to retrieve bathymetry from swell waves shoaling and refraction phenomena in coastal areas have been proposed. Such techniques rely on swell waves propagating on sea surface that must be present in the imaged scene, no matter their direction. Extraction of bathymetric features by means of wave-based techniques needs that wave parameters depend on local depth, which in turn claims for intermediate local depths (less than half the local swell wavelength). In this case, water depth can be related to swell wavelength by means of the small amplitude or linear wave theory (wave height smaller than wavelength). Utilizing a SAR image, it is possible to track a wave from open sea to shoreline and estimate the change of its wavelength and direction of propagation. For very shallow water (few meters depth) instead, the ratio of the depth over the wavelength becomes relatively small and wave crests become higher. In such a situation, non linear theories should be utilized, even if their performance in terms of bathymetric accuracy depends on the availability of high quality a-priori information on wave height and crest behaviour.

Therefore, the performed research has reviewed the main phenomena related to swell waves propagation that allow underwater bathymetric features to be detected in coastal areas from SAR images. The properties and features of the generally adopted expression of the dispersion relation for SAR-based bathymetric data retrieval, i.e. the finite depth linear version of the dispersion relation for swell waves, have been discussed. Its viability and potential performance when applied to SAR-based bathymetry have been analyzed. An error budget model has been developed to assess capabilities and limits of this approach. Typical ranges of swell wavelength ([20; 300] m) and swell period ([4; 33] s) in coastal areas have been considered. The performed analysis has shown that values of water depth up to 40 m can be retrieved in these conditions by using the linear dispersion relation. Two typical values of high and low spatial resolution of SAR, respectively, have been adopted for the uncertainty in swell wavelength. Moreover, two values have been used for the uncertainty in swell period. The performed study has shown that the values of uncertainty in the estimated water depth are lower than 0.6 m (4.6 m) for almost all the acceptable values of wavelength and period, in the case of the minimum (maximum) values of uncertainties on swell parameters that were considered.

An algorithm has been proposed and tested for swell-based bathymetric data by SAR data. The algorithm relies on a linear imaging model and assumes that swell patterns imaged by SAR corresponds to the true swell wave patterns. However, it differs from the merely theory-driven approach because it includes additional steps to be performed in order to properly retrieve swell waves characteristics and sea water depth. The proposed algorithm has been tested on L-band ALOS PALSAR data and X-band COSMO-SkyMed SAR data of the Gulf of Naples, Italy, provided by the Italian Space Agency in the framework of the SAR4BAT project (Synthetic Aperture Radar data fusion for bathymetric retrieval of seabed in coastal areas and archaeological areas) and Digital Elevation Models of seafloor have been obtained. The obtained results have been compared with the actual values of water depth reported in the official nautical chart provided by the Italian Navy Hydrographic Institute. Comparison has shown that the method is able to successfully follow the behaviour of bottom topography. Based on the indirect process through which bathymetry is sensed by SAR, only seabed features having scale length at least of the same order of magnitude as the peak wavelength of the local swell field can be identified. The presented bathymetric algorithm is thus suggested for gradually varying seabed without sharp depth variations. The adopted dispersion relation is valid in the range of intermediate waters. This range cannot be determined *a-priori*, as it depends on the specific case, i.e. on the actual values of swell wavelength. Different swell fields can be thus sensitive to different bathymetric ranges and features.

References

- [1] National Oceanic and Atmospheric Administration, NOAA's website [Online]. Available at: <http://oceanservice.noaa.gov/facts/bathymetry.html>.
- [2] C. Traversi, *Tecnica Cartografica*. Firenze, Italy: Istituto Geografico Militare, 1968.
- [3] R. Wiebel, M. Heller, "Digital Terrain Modeling," in *Geographical Information System: Principles and Applications*, D.J. Maguire, M.F. Goodchild, D.W. Rhind (eds), Ed. London, UK: Longman, 1991, pp. 269-297.
- [4] Horizon 2020, *The EU Framework Programme for Research and Innovation* [Online]. Available: <http://ec.europa.eu/research/horizon2020/>
- [5] S. Flampouris., "On the wave field propagating over an uneven sea bottom observed by ground based radar," Ph.D Thesis, University of Hamburg, Germany, pp. 207, Jul. 2010.
- [6] B. W. Eakins and L. A. Taylor, "Seamlessly integrating bathymetric and topographic data to support tsunami modeling and forecasting efforts," in *Ocean Globe*, J. Breman, Ed. Redlands, CA, USA: ESRI Press, 2010, pp. 37–56.
- [7] A. Renga, G. Rufino, M. D'Errico, A. Moccia, V. Boccia, M. D. Graziano, C. Aragno, S. Zoffoli, "SAR Bathymetry in the Tyrrhenian Sea by COSMO-SkyMed Data: A Novel Approach," *IEEE Journal of Selected Topics in Applied Earth Observation and Remote Sensing*, vol. 7, no. 7, pp. 2834-2847, Jul. 2014. DOI: 10.1109/JSTARS.2014.2327150, 2014, ISSN 1939-1404.
- [8] International Hydrographic Bureau, "Depth Determination," in *Manual on Hydrography*, Publication M-13, first edition, May 2005.
- [9] A. Guadagni, "Rilevamenti Marini e Batimetria," in *Prontuario dell'ingegnere*, Hoepli, 2010.
- [10] J. Gao, "Bathymetric mapping by means of remote sensing: methods, accuracy and limitations," *Progress in Physical Geography*, Vol. 33, No. 1, pp. 103–116, 2009.
- [11] D. K. Burton, *Modern Radar System Analysis*. Boston, MA: Artech House, 1991.
- [12] X. Lurton, *An Introduction to Underwater Acoustics – Principles and Applications*, Springer-Praxis Books in Geophysical Sciences, Springer-Verlag, Chichester, UK, 2002.
- [13] National Oceanic and Atmospheric Administration (NOAA) National Ocean Service, "What is LIDAR?" [Online]. Available: <http://oceanservice.noaa.gov/facts/lidar.html>.
- [14] National Oceanic and Atmospheric Administration (NOAA) Coastal Services Center. 2012. "Lidar 101: An Introduction to Lidar Technology, Data, and Applications."

- Revised. Charleston, SC: NOAA Coastal Services Center, [Online]. Available: http://coast.noaa.gov/digitalcoast/_pdf/lidar101.pdf.
- [15] R. Reuter, "Ocean Remote Sensing Using Lasers", Tutorial from the 24th European Association of Remote Sensing Laboratories (EARSeL), Symposium, 2004, [Online]. Available: <http://www.earsel.org/?target=educ>.
- [16] National Oceanic and Atmospheric Administration (NOAA) Office of Coast Survey, "Lidar" [Online]. Available: <http://www.nauticalcharts.noaa.gov/hsd/lidar.html>.
- [17] H. Abdallah, J.-S. Bailly, N. N. Baghdadi, N. Saint-Geours, F. Fabre, "Potential of space-borne LiDAR sensors for global bathymetry in coastal and inland waters," *IEEE J. Sel. Topics Appl. Earth Observ. Remote Sens.*, vol. 6, no. 1, pp. 202–216, Feb. 2013.
- [18] V. I. Feigels, Yu. I. Kopilevich, "Lasers for lidar bathymetry and oceanographic research: choice criteria," in *Proceedings of the IEEE International Geoscience and Remote Sensing Symposium 1994, IGARSS '94*, August, vol. 1, pp. 475-478.
- [19] H. Parker, M. Sinclair, "The successful application of Airborne LiDAR Bathymetry surveys using latest technology," in *Proceedings of OCEANS 2012*, Virginia, USA, Oct 14-19, pp. 1-4.
- [20] J. M. Wozencraft, "Complete coastal mapping with airborne lidar," in *Proceedings of OCEANS '02 MTS/IEEE*, Oct. 29-32, 2002, vol. 2, pp. 1194-1198.
- [21] G. C. Guenther, A. G. Cunningham, P. E. La Rocque, D. J. Reid, "Meeting the accuracy challenge in airborne lidar bathymetry", in *Proc. Of EARSeL-SIG-Workshop LIDAR*, Dresden, Germany, June 16-17, 2000.
- [22] W. J. Lillycrop, J. L. Irish, L. E. Parson, "SHOALS system," *Sea Technology*, vol. 38, no. 6, pp. 17–25, 1997.
- [23] G. . Shaw, H. K. Burke, "Spectral Imaging for Remote Sensing", *Lincon Laboratory Journal*, Vol. 14, no. 1, 2003, pp. 3-28, [Online]. Available: https://www.ll.mit.edu/publications/journal/pdf/vol14_no1/14_1remotesensing.pdf.
- [24] H. M. Dierssen, "Perspectives on empirical approaches for ocean color remote sensing of chlorophyll in a changing climate," in *Proceedings of the National Academy of Science of the United States of America*, USA, Oct 5, 2010; 107(40), pp. 17073-17078. DOI: 10.1073/pnas.0913800107.
- [25] D. R. Lyzenga, N. P. Malinas, F. J. Tanis, "Multispectral bathymetry using a simple physically based algorithm," *IEEE Transactions on Geoscience and Remote Sensing*, vol. 44, no. 8, August 2006.
- [26] D. R. Lyzenga, "Remote sensing of bottom reflectance and water attenuation parameter in shallow water using aircraft and Landsat data," *International Journal of Remote Sensing*, vol. 2, issue 1, 1981. DOI: 10.1080/01431168108948342.
- [27] W. D. Philpot, "Bathymetric mapping with passive multispectral imagery," *Applied*

- Optics*, vol. 28, issue 8, pp. 1569-1578, 1990.
- [28] S. Maritorena, A. Morel, B. Gentili, "Diffuse reflectance of oceanic shallow waters: Influence of water depth and bottom albedo," *Limnol. Oceanogr.*, vol. 39, pp. 1689-1703, 1994.
- [29] D. Jupp, "Background and extensions to depth of penetration (DOP) mapping in shallow coastal waters," in *Proceedings of the Symposium on Remote Sensing of the Coastal Zone*, Gold Coast, Queensland, 1988, pp. IV.2.1-IV.2.19.
- [30] H. M. Dierssen, A. E. Theberge Jr., "Bathymetry: Assessing Methods", *Encyclopedia of Natural Resources* [Online]. Available: http://colors.uconn.edu/pubs/DIERSEN-Bathymetry_Methods_LO.pdf.
- [31] S. Jay, M. Guillaume, J. Blanc-Talon, "Underwater target detection with hyperspectral data: Solutions for both known and unknown water quality," *IEEE Journal of Selected Topics in Applied Earth Observation and Remote Sensing*, vol. 5, no. 4, pp. 1213–1221, Aug. 2012.
- [32] A. Pleskachevsky, S. Lehner, T. Heege, C. Mott, "Synergy and fusion of optical and synthetic aperture radar satellite data for underwater topography estimation in coastal areas," in *Ocean Dynamics*, vol. 61, pp. 2099-2120, 2011.
- [33] C.R. McClain, "A decade of satellite ocean colour observations*," *Annual Review of Marine Science*, vol. 1, January 2009, pp.19–42. DOI: 10.1146/annurev.marine.010908.163650.
- [34] J. Vogelzang, G. J. Wensink, C. J. Calkoen, M. W. A. van der Kooij, "Mapping submarine sand waves with multi-band imaging radar, 2. Experimental results and model comparison," *J. Geophys. Res.*, vol. 102, pp. 1183–1192, 1997.
- [35] W. Alpers, G. Campbell, H. Wensik, and Q. Zhang, "Underwater topography," in *Synthetic Aperture Radar Marine User's Manual*, Washington, DC, USA: U.S. Department of Commerce, 1st ed., 2004, ch. 10, pp. 245–262.
- [36] A. Renga et al., "Analysis of SAR monitoring capabilities in coastal areas," in *Proceedings of the IET International Conference on Radar Systems*, IET RADAR 2012, Glasgow, Scotland, Oct. 2012, pp. 1–6.
- [37] W. Alpers, I. Hennings, "A theory of the imaging mechanism of underwater bottom topography by real and synthetic aperture radar," *J. Geophys. Res.*, vol. 89, no. 10, pp. 529-546, 1984.
- [38] C. Wackerman, D. Lyzenga, E. Ericson, and D. Walker, "Estimating Near-Shore Bathymetry Using SAR," in *Proceedings of the IEEE International Geoscience and Remote Sensing Symposium 1998, IGARSS'98*, vol. 3, pp. 1668-1670.
- [39] S. Brusch, P. Held, S. Lehner, W. Rosenthal, A. Pleskachevsky, "Underwater Bottom Topography in coastal areas from TerraSAR-X data," *International Journal of Remote*

- Sensing*, vol. 32, Issue 16, 2011.
- [40] F. T. Ulaby, R. K. Moore, A. K. Fung, *Microwave Remote Sensing Active and Passive*, Volume III, From Theory to Application, Artech House, 1986, pp.1418-1420.
- [41] I. S. Robinson, *Measuring the Oceans from Space*, Chichester, UK: Springer, Praxis Publishing Ltd, 2004.
- [42] I.S. Robinson, *Satellite Oceanography*, Ellis Horwood limited, 1985.
- [43] I. G. Main, *Vibrations and Waves in Physics*, Cambridge University Press, Second Edition, 1988, chapters 12-13.
- [44] CDIP, The Coastal Data Information Program, Integrative Oceanography Division, "Wave Measurement", [Online]. Available: <http://cdip.ucsd.edu/?sub=index&nav=documents&xitem=waves>.
- [45] "Waves" [Online]. Available: <http://educationally.narod.ru/wavesphotoalbum.html>.
- [46] Hasselmann et al., "Measurement of wind-wave growth and swell decay during the joint North Sea wave project (JONSWAP)," *Deutschen Hydrographischen Zeitschrift*, vol. 8, no. 12, 1973 [Online]. Available: <file:///C:/Users/user/Downloads/Jonswap-Hasselmann1973.pdf>.
- [47] K. Hasselman et al., "Theory of Synthetic Aperture Radar Ocean Imaging: a MARSEN View," *J. Geophys. Res.*, vol. 90, no. C3, pp. 4659-4686, May 1985.
- [48] U.S. Army Corps of Engineers, *Coastal Engineering Manual*, Vicksburg, Mississippi, 2nd ed., 2008, pp. II-1-1 - II-1-106.
- [49] G. J. Komen, L. Cavaleri, M. Donelan, K. Hasselmann, S. Hasselmann, P. A. E. M. Janssen, *Dynamics and Modelling of Ocean Waves*, Cambridge, UK: Cambridge University Press, 1994, pp. 5-16, 343-349, 391-402.
- [50] C. J. Calkoen, G. H. F. Hesselmanns, G. J. Wesink, J. Vogelzang, "The Bathymetry Assessment System. Efficient depth mapping in shallow seas using radar images," *International Journal of Remote Sensing*, vol. 22, no. 15, pp. 2973-2998, 2001.
- [51] Canada Centre for Remote Sensing, "Fundamentals of Remote Sensing", Remote Sensing Tutorial [Online]. Available: file:///G:/LIBRI/Fundamentals_of_Remote_Sensing_TUTORIAL_CANADA.pdf.
- [52] C. A. Wiley, "Synthetic Aperture Radar, A paradigm for technology evolution," *IEEE Transactions on Aerospace and Electronic Systems*, vol. 21, pp. 440-443, 1985. DOI:10.1109/TAES.1985.310578.
- [53] A. Moccia, "Synthetic Aperture Radar," in *Encyclopedia of aerospace engineering*, Editor: John Wiley & Sons, Ltd. Chichester. R. Blockley, W. Shyy (eds), 2010. ISBN: 9780470754405.
- [54] A. Moccia, A. Renga, "Bistatic Synthetic Aperture Radar," in *Distributed Space Missions for Earth System Monitoring*, Space Technology Library 31, New York,

- USA: Springer Science+Business Media, 2013, Chapter 1. DOI: 10.1007/978-1-4614-4541-8_1.
- [55] B. C. Barber, "Theory of Digital Imaging from Orbital Synthetic Aperture Radar," *International Journal of Remote Sensing*, vol. 6, Issue 7, pp. 1009-1057, 1985.
- [56] F. T. Ulaby, R. K. Moore, A. K. Fung, *Microwave Remote Sensing Active and Passive*, Volume II, Radar Remote Sensing and Surface Scattering and Emission Theory, Reading, MA: Addison-Wesley Publishing Company, 1982.
- [57] J. C. Curlander, R. N. McDonough, *Synthetic Aperture Radar Systems & Signal Processing*, Wiley Series in Remote Sensing, New York, USA: Wiley Interscience, 1991.
- [58] F. Collard, F. Ardhuin, B. Chapron, "Monitoring and analysis of ocean swell fields from space: new methods for routine observations," *Journal of Geophysical Research*, vol. 114, pp. 1–15, 2009.
- [59] B. Chapron, H. Johnsen, and R. Garello, "Wave and wind retrieval from SAR images of the ocean," *Annals of Telecommunications*, vol. 56, no. 11-12, pp. 682–699, 2001.
- [60] S. Flampouris, J. Seeman, F. Ziemer, "Sharing our Experience Using Wave Theories Inversion for the Determination of the Local Depth," in *Proceedings of OceanSAR 2009*, Herrsching, Germany, Sept. 7-11.
- [61] R. A. Dalrymple, F. Asce, A. B. Kennedy, J. T. Kirby, M. Asce, Qin Chen, "Determining depth from remotely-sensed images," *Coastal Engineering Proceedings*, no. 26, pp. 2395-2408, 1998.
- [62] Y. K. Holland, "Application of the linear dispersion relation with respect to depth inversion and remotely sensed imagery," *IEEE Trans. Geosc. Remote Sens.*, vol. 39, pp. 2060-2072, 2001.
- [63] I. A. Svendsen, J. Buhr Hansen, "Deformation up to breaking of periodic waves on a beach", in *Proceedings of the 15th International Coastal Engineering Conference*, ICCE, Hamburg, Germany, 1976, pp. 477-496.
- [64] J. T. Kirby, R. A. Dalrymple, "An approximate model for nonlinear dispersion in monochromatic wave propagation models," in *Coastal Engineering*, vol. 9, 1986, pp. 545-561.
- [65] G. P. De Loor, H. W. Brunsveld van Hulst, *Microwave measurements over the North Sea*, *Boundary Layer Meteorology*, vol. 13, pp. 113-131, 1978.
- [66] G. P. De Loor, "The observation of tidal patterns, currents and bathymetry with SLAR imagery of the sea," *IEEE Transactions on Oceanic Engineering*, vol. 6, pp. 124-129, 1981.
- [67] E. S. Kasischke, R. A. Shuchman, D. R. Lyzenga, G. A. Meadows, "Detection of bottom features on SEASAT synthetic aperture radar imagery," *Photogrammetric*

- Engineering and Remote Sensing*, vol. 49, pp. 1341-1353, 1983.
- [68] D. W. S. Lodge, "Surface expression of bathymetry on SEASAT synthetic aperture radar images," *International Journal of Remote Sensing*, vol. 4, pp. 639-653, 1983.
- [69] A. Renga, V. Boccia, M. D'Errico, G. Rufino, A. Moccia, C. Aragno, S. Zoffoli, "Analysis of SAR monitoring capabilities in coastal areas," *Proceedings of the IET International Conference on Radar Systems, IET RADAR 2012*, Glasgow, Scotland, 22-25 Oct, 2012, 6 pp. ISBN 978-1-84919-676-5, ISSN 0537-9989, Reference PEP0603Z, DOI: 10.1049/cp.2012.1609.
- [70] C. B. Vreugdenhil, *Numerical Methods for Shallow-Water Flow*, Water Science and Technology Library, Vol. 13, Dordrecht, The Netherlands: Kluwer Academic Pub., 1994, pp. 15-46.
- [71] M. S. Longuet-Higgins, R. W. Stewart, "Radiation stresses in water waves, a physical discussion with applications," *Deep-Sea Research*, vol. 11, pp. 529-562, 1964.
- [72] J. Vogelzang, "The mapping of bottom topography with imaging radar. A comparison of the hydrodynamic modulation in some existing models," *International Journal of Remote Sensing*, vol. 10, no. 9, pp. 1503–1518, 1989.
- [73] J. Inglada, R. Garello, "On rewriting the Imaging Mechanism of Underwater Bottom Topography by Synthetic Aperture Radar as Volterra Series Expansion," *IEEE Journal of Oceanic Engineering*, vol. 27, no. 3, pp. 665-670, Jul., 2002.
- [74] R. Romeiser, W. Alpers, "An improved composite surface model for the radar backscattering cross section of the ocean surface 2. Model response to surface roughness variations and the radar imaging of underwater bottom topography," *Journal of Geophysical Research*, vol. 102(C11), no. 25, pp. 251-267, 1997.
- [75] R. A. Shuchman, D. R. Lyzenga, G. A. Meadows, "Synthetic Aperture Radar imaging of ocean-bottom topography via tidal-current interactions: theory and observations," *International Journal of Remote Sensing*, vol. 6, pp. 1179-1200, 1985.
- [76] C. F. De Valk, G. J. Wensink, "Measuring the bathymetry of shallow seas using radar imagery from satellite and aircraft," in *Proceedings of the Offshore Technology Conference*, Houston, 2002, paper 14276.
- [77] H. Greidanus, C. Calkoen, I. Hennings, R. Romeiser, J. Vogelzang, G. J. Wensink, "Intercomparison and validation of bathymetry radar imaging models," in *Proceedings of the IEEE International Geoscience Remote Sensing Symposium 1997, IGARSS'97*, vol. 3, pp. 1320–1322.
- [78] J. Inglada and R. Garello, "Volterra model for the imaging mechanism of ocean surface currents by synthetic aperture radar," in *Proceedings of the IEEE International Geoscience Remote Sensing Symposium 1999, IGARSS'99*, Hamburg, Germany, June 28-July 2, pp. 2551-2553.

- [79] J. Inglada, R. Garello, "Depth estimation and 3D topography reconstruction from SAR images showing underwater bottom topography signatures," in *Proceedings of the IEEE International Geoscience Remote Sensing Symposium 1999, IGARSS'99*, Hamburg, Germany, June 28-July 2, pp. 956–98.
- [80] A. Renga, G. Rufino, M. D'Errico, A. Moccia, V. Boccia, M. D. Graziano, C. Aragno, S. Zoffoli, "Analysis of spaceborne SAR monitoring capabilities for coastal areas bathymetry with COSMO-SkyMed and ALOS data," in *Proceedings of SPIE Remote Sensing 2013 Conference, Remote Sensing of the Ocean, Sea Ice, Coastal Waters, and Large Water Regions 2013*, vol. 8888, Dresden, Germany, 23-26 Sept., 2013, no. 888808, 15 pp. DOI: 10.1117/12.2028974.
- [81] I. Hennings, B. Lurin, N. Didden, "Radar Imaging Mechanism of the Seabed: Results of the C-STAR Experiment in 1996 with Special Emphasis on the Relaxation Rate of Short Waves due to Current Variations," *Journal of Physical Oceanography*, vol. 31, pp. 1807-1827, 2001.
- [82] Italian Space Agency, *COSMO-SkyMed System Description & User Guide*, 2007.
- [83] Italian Space Agency, *COSMO-SkyMed SAR Products Handbook*.
- [84] J. Vogelzang, G. J. Wensink, G. P. de Loor, H. C. Peters, H. Pouwels, "Sea bottom topography with X-band SLAR: The relation between radar imagery and bathymetry," *International Journal of Remote Sensing*, vol. 13, no. 10, pp. 1943–1958, 1992.
- [85] M. Marghany, M. Hashim, A. P. Cracknell, "3D Bathymetry Reconstruction from Airborne Topsar Polarized Data," in *Proceedings of the International Conference on Computational Science and Its Applications, ICCSA 2007*, Kuala Lumpur, Malaysia, August 26-29, pp. 410 – 420.
- [86] P. Perona, J. Malik, "Scale-Space and Edge Detection Using Anisotropic Diffusion," *IEEE Transactions on Pattern Analysis and Machine Intelligence*, Vol. 12, No. 7, pp. 629-639, July 1990.
- [87] V. Boccia, A. Renga, G. Rufino, M. D'Errico, A. Moccia, C. Aragno, S. Zoffoli, "Linear dispersion relation and depth sensitivity to swell parameters: Application to Synthetic Aperture Radar Imaging and Bathymetry," *The Scientific World Journal*, vol. 2015, Article ID 374579, pp. 10, 2015. DOI:10.1155/2015/374579, ISSN 2356-6140.
- [88] Japanese Aerospace Exploration Agency, *ALOS Data Users Handbook*, Revision C, 2008.
- [89] V. Boccia, A. Renga, G. Rufino, A. Moccia, M. D'Errico, C. Aragno, S. Zoffoli, "L-band SAR image processing for the determination of coastal bathymetry based on swell analysis," in *Proceedings of the Geoscience and Remote Sensing Symposium IGARSS 2014*, Québec, Canada, 13-18 July, pp. 5144-5147. DOI:

- 10.1109/IGARSS.2014.6947656.
- [90] B. Holt, "SAR imaging of the ocean surface," *Synthetic Aperture Radar Marine User's Manual*, C. R. Jackson and J. R. Apel, Eds., pp. 25–79, NOAA, Washington, DC, USA, 2004.
- [91] M. K. Mishra, D. Ganguly, P. Chauhan, Ajai, "Estimation of Coastal Bathymetry Using RISAT-1 C-Band Microwave SAR Data," *IEEE Geoscience and Remote Sensing Letters*, vol. 11, no. 3, pp. 671-675, Mar. 2014.
- [92] V. Boccia, A. Renga, M. D'Errico, G. Rufino, A. Moccia, M.D. Graziano, C. Aragno, S. Zoffoli, "Application of SAR data from Cosmo-SkyMed and ALOS for coastal area bathymetry in the Gulf of Naples," in *Proceedings of the Italian Association of Aeronautics and Astronautics AIDAA XXII Conference*, Naples, Italy, Sept. 9-12, 2013.
- [93] Italian Space Agency, SAR4BAT project, July 13th, 2011, [Online]. Available: <http://www.asi.it/files/SAR4BAT.pdf>.
- [94] European Space Agency, "NEST - Next ESA SAR Toolbox", [Online]. Available: <https://earth.esa.int/web/nest/home>.
- [95] "Golfo di Napoli" Nautical Chart, Navy Hydrographic Institute, number 127, edition 1/2004, Scale 1:60.000.
- [96] "Canali d'Ischia e Procida" Nautical Chart, Navy Hydrographic Institute, number 129, edition 2/2010, Scale 1:30.000.
- [97] "Golfo di Pozzuoli" Bathymetric Chart, Navy Hydrographic Institute, number 1256, Scale 1:20000.
- [98] Weather data and wind speed measurements at the Napoli Station of the National Tidegauge Network [Online]. Available: mareografico.it.
- [99] M. Menna, "Misure di correnti superficiali nel Golfo di Napoli eseguite con radar costiero", Ph.D. thesis, Università degli Studi di Napoli "Federico II", 2007, [Online]. Available: http://www.fedoa.unina.it/2660/1/Menna_Scienze_e_Ingegneria_del_Mare.pdf.
- [100] V. Boccia, A. Renga, G. Rufino, A. Moccia, M. D'Errico, S. Zoffoli, C. Aragno, "Seabed morphology retrieval in coastal areas from ALOS and COSMO-SkyMed SAR data," *Proceedings of the 65th International Astronautical Congress, IAC 2014*, Toronto, Canada, 29 Sept - 3 Oct, 2014.